



**CENTRO DE INVESTIGACIÓN Y DE ESTUDIOS AVANZADOS
DEL INSTITUTO POLITÉCNICO NACIONAL**

UNIDAD QUERETARO

**Caracterización estructural y electrónica de Fe_3C bajo presión.
Un estudio de primeros principios**

Tesis que presenta

Alejandra Vargas Calderón

para obtener el Grado de

Maestro(a) en Ciencias

en la Especialidad de

Materiales



**Director de la Tesis / Codirector de la Tesis:
Dr. Aldo Humberto Romero Castro / Dr. Razvan Caracas**

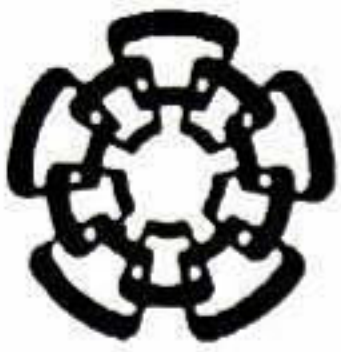
Santiago de Querétaro, Qro.

Junio 2010

**CINVESTAV
IPN
ADQUISICION
DE LIBROS**

CLAS: TA404.2 V37 2010
ADQUIS: - 51-150
FE: 13-Enero-2011
F: Tesis-2010

ID: 167568-1001



CENTRO DE INVESTIGACIÓN Y DE ESTUDIOS AVANZADOS
DEL INSTITUTO POLITÉCNICO NACIONAL

UNIDAD QUERETARO

Structural and electronic characterization of Fe_3C under pressure.
An ab initio study

Thesis submitted by

Alejandra Vargas Calderón

to obtain the Degree of

Master in Science

Materials specialty

Thesis advisor/ Thesis supervisor:
Dr. Aldo Humberto Romero Castro / Dr. Razvan Caracas

Santiago de Querétaro, Qro.

June 2010

To my mother and my family Italia, Luis y Ruben for their unconditional support.

Acknowledgements

I would to thank the following for their contributions to my Master studies.

First to Dr. Aldo Humberto Romero Castro and Dr. Razvan Caracas, for his stalwart supervision during the execution of this research work.

Also to all the members of the theoretical research group in computational Materials Science at *CINVESTAV* Querétaro (Jazmin, Alejandra, Pilar, Hugo, Sinhue & Carolina), but specially to Rosa Elena Dávila Martínez and Luis Enrique Díaz. And finally to all of my friends at *CINVESTAV* for their friendship and support.

To *CINVESTAV's* department of Materials Science.

To the Consejo Nacional de Ciencia y tecnología (*CONACYT*) for providing the financial support that allowed me to carry to completion the Master in Material sciences (numero de becario 210697) as well as the research stay at the Laboratoire de Sciences de la Terre de la Ecole Normale Supérieure de Lyon (*ENS*) in France (numero de proyecto J-59853-F).

To the bilateral scientific agreement between the Belgian Fund for Scientific Research (*F.R.S – FNRS*) for the financial support provided to visit the European Theoretical Spectroscopy Facility at the University of Louvain (*U.C.L*) in Belgium.

Finally to acknowledge the following institutions for providing computational resources needed to realize this work:

To the Instituto Potosino de Investigación Científica y Tecnológica (*IPYCIT*).

To the Centre Informatique National de l'Enseignement Supérieure at France (*CINES*).

And also to Dr. Alfonso Muñoz from the Physics department of the University of La Laguna, at Spain.

Contents

Introduction	1
1 State of the art	3
1.1 The earth's interior	3
1.2 The Fe_3C compound	5
1.3 Iron carbide in the earth's inner core	6
2 Theoretical Background	9
2.1 Introduction	9
2.2 Ab initio methods	9
2.3 Born Oppenheimer approach	10
2.4 Density Functional Theory	11
2.4.1 The Hohenberg-Kohn theorem	11
2.4.2 The Kohn-Sham method	12
2.4.3 Exchange correlation	13
2.4.4 Handling electron-ion interactions	13
2.4.5 Projector Augmented Wave Method	15
2.5 ABINIT	18
2.5.1 What does the code do?	18
2.5.2 ABINIT reliability	20
2.5.3 ABINIT parallelization	21
3 Ground State Properties	23
3.1 Introduction .	23
3.1.1 Thermodynamics	23
3.2 Methodology	24
3.2.1 Computational details	24
3.2.2 Types of calculations	25
3.3 Results .	26
3.3.1 Structural relaxation	26
3.3.2 Magnetic properties	31
4 Effect of pressure	35
4.1 Introduction	35
4.1.1 Thermodynamics	35
4.1.2 The invar effect	36
4.1.3 Equation of state	36
4.2 Methodology	37

4.3	Results	37
4.3.1	Pressure-induced magnetic phase transition	37
4.3.2	Magnetic transition parameters	38
4.3.3	Effect on Compressibility	42
4.3.4	Equation of state	47
5	Elastic Properties	55
5.1	Introduction	55
5.1.1	Stress-strain relations	55
5.1.2	The Voigt-Reuss scheme	56
5.1.3	Seismic waves and density	57
5.2	Methodology	58
5.3	Results .	59
5.3.1	Ground state elastic properties	59
5.3.2	High pressure elastic properties	60
5.3.3	Sound Velocities and Density	65
	Conclusions	69
	Bibliography	77

List of Figures

1.1	Structure of earth's interior.	4
1.2	The <i>PREM</i> model.	4
1.3	Natural iron carbide (cohenite)	6
1.4	Phase diagram of the <i>F - C</i> system	6
2.1	Solution of the Khon-Sham equations diagram	14
2.2	Comparisson of <i>LDA</i> versus <i>GGA</i> accuracy	21
3.1	Unit cell of antiferromagnetic spin configuration (AFM-S).	26
3.2	Fe_3C unit cell showing <i>Fe</i> atoms in special and general positions	27
3.3	Crystal structure of cementite	27
3.4	Bond lengths between iron atoms	29
3.5	Bond lengths between iron atoms	29
3.6	Unit cell of Fe_3C showing atom labels	30
3.7	Bond lengths between iron and carbon atoms	30
3.8	Polar charge density map FM configuration	33
3.9	Polar charge density map AFM-S configuration	33
4.1	Relative enthalpy from zero to 300 <i>GPa</i>	39
4.2	Relative enthalpy from zero to 30 <i>GPa</i>	39
4.3	Magnetic moment as a function of pressure.	41
4.4	Magnetic moment as a function of volume	41
4.5	Relative compressibility for FM calculation	44
4.6	Relative compressibility for FMM calculation	44
4.7	Compressibility for fixed magnetic moment (FMM) calculation.	46
4.8	Compressibility for ferromagnetic (FM) calculation.	46
4.9	Angle compressibility vs. pressure, FM calculation	48
4.10	Bond lenght compressibility vs. pressure, FM calculation	48
4.11	Angle compressibility vs. pressure, FMM calculation	49
4.12	Bond length compressibility vs. pressure, FMM calcaultion	49
4.13	Fe_3C unit cell showing angles considered in figures 4.9 and 4.11	50
5.1	Elastic constants vs. pressure, NS calculation	62
5.2	Bulk <i>K</i> and shear <i>G</i> modulus.	64
5.3	Poisson's ratio as a function of pressure	65
5.4	Compressional V_P and shear V_S wave velocities	66
5.5	Density for NS calculation and comparisson with <i>hcp</i> iron and <i>PREM</i> .	67

List of Tables

2.1	Comparisson of PAW accuracy	22
3.1	Unit cell parameters and volume V_0 at 0GPa	28
3.2	Unit cell parameters at 0GPa for FMM calculation	28
3.3	Magnetic moment and inter-atomic distances in Fe_3C at 0GPa.	31
4.1	Magnetic transition parameters for Fe_3C	43
4.2	Effect of magnetization on the <i>EOS</i>	51
4.3	Effect of pressure on the <i>EOS</i>	52
4.4	Equation of state parameters for Fe_3C	53
5.1	Elastic constants at 0GPa.	61

Abstract

This is a study of iron carbide Fe_3C , under pressure employing state-of-the-art first-principles calculations under the Projected Augmented Wave Method (*PAW*) approach to density-functional theory (*DFT*) in the *ABINIT* implementation. In order to get a deeper understanding of the nature of the pressure induced magnetic transition from a low-pressure magnetically ordered state to a high-pressure magnetically disordered state observed in Fe_3C , structural and electronic properties for different spin configurations and residual values were computed over a large pressure range. Then, the enthalpy was employed as the parameter that determines the stability of each configuration. This calculations included an antiferromagnetic system for which three kinds of calculations were carried out, a non-spin polarized calculation, a zero fixed magnetic moment calculation (which mimics an antiferromagnetic configuration) and finally an antiferromagnetic structure which belongs to the magnetic space group *Shubnikov* type *III Fedorov* space group $P 2_1 2_1 2_1$ #19. The study was complemented by calculating the electronic structure and the minimal energy configuration of several ferromagnetic structure by fixing the magnetic moment to 4, 8, 10, 12, 16, 20, 24, 36, and 48 bohr's magneton. The results showed that the magnetic transition occurs around 30GPa, and it is accompanied by a discontinuous change of the axial compressibility. This alloy have been considered as a strong candidate to be major forming constituent phase of the Earth's inner core. Therefore, the elastic constant tensor of the high-pressure non-magnetized phase was computed as well. From this last, the elastic properties up to core conditions were determined. Results were interpreted in conjunction with available seismological data. As expected, it was concluded that carbon considerably reduce the seismic wave velocities and density of the iron-based alloys of the Earth's core.

Resumen

El presente trabajo es un estudio de primeros principios del carburo de hierro Fe_3C bajo presión, empleando la aproximación de ondas planas proyectadas y aumentadas (*PAW* por sus siglas en inglés) en el marco de la Teoría del Funcional de la Densidad (*TFD*) implementado en el código *ABINIT*. El objetivo principal, es entender la naturaleza de la transición magnética inducida por el efecto de la presión que se ha observado para este compuesto. Esta transición tiene lugar de un estado ordenado y magnético a bajas presiones, a un estado desordenado no magnético a altas presiones. Por este motivo, se llevaron a cabo cálculos estructurales y electrónicos para diferentes configuraciones de spin y valores residuales de la magnetización, sobre un espectro amplio de presiones. La entalpía fue empleada como el parámetro que determina la estabilidad de cada configuración. Se consideraron sistemas antiferromagnéticos para los cuales tres tipos de cálculos fueron realizados; de spin no polarizado, de momento magnético fijado a cero y además una estructura antiferromagnética que pertenece al grupo magnético espacial *Shubnikov* tipo *III* grupo espacial *Fedorov* $P 2_1 2_1 2_1$ #19. Adicionalmente se consideraron varias configuraciones ferromagnéticas, fijando el momento magnético total a 4, 8, 10, 12, 16, 20, 24, 36 y 48 magnetones de Bohr. Los resultados mostraron, que la transición magnética ocurre alrededor de 30GPa y esta acompañada por un cambio discontinuo de la compresibilidad axial. Este compuesto ha sido considerado como un fuerte candidato a ser una fase presente en el núcleo de la tierra. Por esta razón, también se ha calculado el tensor de constantes elásticas para la fase no magnética estable a altas presiones. A partir de ello, se determinaron, las propiedades elásticas para un rango de presiones correspondientes al núcleo de la tierra. Los resultados encontrados fueron interpretados en conjunción con datos sismológicos. Como era de esperarse, a altas presiones la densidad y las velocidades sísmicas medidas para Fe_3C se ven reducidas considerablemente en comparación a las del hierro hcp, y por lo tanto las propiedades elásticas de Fe_3C se aproximan mejor a las condiciones del núcleo de la tierra.

Introduction

Materials science is one of the disciplines that has taken more advantage by the improvement of computational techniques. There are many physical properties that can be computed with the adequate theoretical knowledge and computational tools. Besides, this is done in a more practical way than its experimental counterpart. A lot of time, control management and economical cost can be save with these methods. For instance, in the last years the dramatic effect that high pressure conditions has on matter has been reveled with the asistance of computer simulations. In fact, materials present a different behavior from that at normal conditions because pressure produces changes in the atomic and electronic structure of matter. When the distance between atoms decrease due to high pressures, the chemical bonds are affected by the overlapping of atomic orbitals [1].

Similarly, for long time the study of the earth's interior composition remained inaccessible to scientific research. The extreme conditions of high pressure and temperature in this region makes very difficult to perform experiments, thus only seismological data were available. Nowadays there are many studies on the subject realized by computer simulations where high pressure and temperature conditions are easily achieve.

According to one of the most accepted seismological models *PREM* (Preliminary Reference Earth Model Dzitewonski & Anderson, 1981), the earth's core density is about %10 less than that of iron measured under the same temperature and pressure conditions. In spite of, it has been suggested that the core must be mainly composed of iron alloyed with some lower atomic weight elements (lower than iron). Due to its high cosmological abundance the strongest candidates are *H*, *O*, *C*, *Si* and *S* [2]. Among these elements, carbon is quite relevant because meets further constrains.

Based on these assumptions *Wood* proposed that Fe_3C (cementite) might be the major phase forming the earth's inner core [3]. He performed thermodynamic calculations and derived a equation of state (*EOS*) which gave a density, incompressibility K_0 and its first derivative K' at an a average inner core pressure of 338GPa, in excellent agreement with the inner's core density values of *PREM*. Similar results were obtained by high pressure X-ray powder diffraction measurements at room temperature [4], [5]. However, later was demonstrated that cementite's magnetic character can be affect either by temperature (from

ferromagnetic to paramagnetic behavior [6]) or by pressure (from a low-pressure magnetically ordered to a high-pressure non-magnetically ordered state [7]). Accordingly, *Wood's EOS* is not necessarily accurate to model the earth's inner core, since the high pressure and temperature conditions will ensure that cementite will be in a non magnetically ordered state.

At the moment exist a great variety of studies concerning the pressure induced magnetic phase transition in Fe_3C and the possibility of this material been a forming major phase inside the earth's inner core. However, there is great disagreement between them (both theoretical and experimental studies). Moreover, in order to compare the elastic properties of Fe_3C with seismic measurements, its high pressure elastic constant tensor is needed. Nevertheless, these properties have not been measured neither theoretically or experimentally.

For all the aforementioned, it has been decided to focus the present work in a systematic study of the magnetic character of Fe_3C under pressure and to obtain its high pressure elastic properties. This allows to discern the accuracy between previous results and it helps as well to answer whether cementite can be a major phase inside the earth's inner core or not.

To achieve this goal *ab initio* calculations based on density-functional theory were performed since this method provide an excellent tool to obtain physical properties of materials, when experimental studies are difficult to perform.

In summary, this study is focus on three points:

- To perform a ground state structural characterization and to study the cementite's magnetic character.
- To reproduce the reported pressure induced magnetic phase transition in Fe_3C and to study its effects on the equation of state.
- To determine the high pressure elastic properties of Fe_3C in order to investigate the possibility of Fe_3C being a major phase inside the earth's inner core.

This thesis is composed of five chapters. Chapters 1 and 2 contain introductory information. The first presents the state of the art on the study of the physical properties of Fe_3C . The second comprehend a brief description of Density Functional Theory (*DFT*), electronic structure calculations and the basic concepts under the Projected Augmented Wave method (*PAW*). Chapters 3, 4 and 5 are devoted to present the obtained results. Additionally, each of these are provided with a specific theoretical introduction, computational details and methodology. Chapter 3, deals with the ground state structural and electronic characterization. In chapter 4, the effect of pressure on the magnetic state of Fe_3C is studied and finally the high pressure elastic properties of Fe_3C are presented in chapter 5.

Part I

Chapter 1

State of the art

1.1 The earth's interior

The study of the earth's deep interior is constrained by its great temperature and pressure conditions. Hence, its constitution has to be inferred using indirect methods. As a first approximation, the overall composition of the earth's interior must be somehow similar to the bulk chemical composition of the sun (deduced from its light spectrum). In particular, it is close to the devolatilized chondrite meteorites. These have a similar composition to the sun and are believed to be similar to the material from which the earth accreted. The overall density and mass of the earth is determined based on measurements of how the earth perturbs the orbits of other planets and the moon [8].

Seismograms recorded at stations all over the globe, measure the time of travel of refracted and reflected seismic waves created by earthquakes. Velocities depend on the elastic moduli and density of the medium in which the waves propagate. In turn, the elastic moduli and the density, depend on the crystal structure and chemical composition of the constitutive minerals, on pressure and temperature [9]. This allows to use observations recorded on seismograms to infer the composition or range of compositions of the planet.

According to one of the most accepted seismological models, *PREM* (Preliminary Reference Earth Model Dziewonski & Anderson, 1981) the earth's structure consists of three major first-order seismic boundaries; the core, the mantle and the crust (figure 1.1). Figure 1.2 shows, the variation with depth and pressure, of density, compressional (P) and shear wave velocities (S) through the earth's mantle and core. Note that distinct regions are characterized by the same level of velocity heterogeneity, i.e. regions with a constant speed increase, have uniform composition.

As we go downward in depth, density increases because pressure increases. In general waves speed diminish with density. However the extreme pressure conditions of the earth's interior makes the elastic modulus to grow faster. As a result (with the exception of some transition domains) the overall trend is an increment of seismic wave velocity with pressure (see section 5.1.3). Tempera-

ture also increase the speed of waves, but the effect of pressure is higher.

The mantle and the crust are mostly made of silicates. In particular within the mantle ($P = 24 - 136$ GPa, $T = 773 - 4200$ °K) there is a convective material circulation driven by the loss of heat from the earth's deep interior. It is divided in two regions, the upper mantle is made of silicates of iron and magnesium. The outermost part is tough to be liquid rock while with increasing depth it becomes solid. After this, there is a transition zone where a sudden seismic-velocity discontinuity occurs. In this region, as a consequence of increasing pressure there is rearrangement of atoms in the material to form a denser crystal structure. Thus the lower mantle is in a denser solid state, composed mainly of sulphides and oxides of silicon and magnesium.

To be more specific, it is commonly accepted that the mantle must be dominated by $MgSiO_3$. In the lower mantle this material has the perovskite crystal structure [10]. Nevertheless, it has been discovered that the average atomic number in the mantle (21.3) is higher than that of $MgSiO_3$ (20.1). This difference it is believed to be due to 10% substitution of Mg by Fe . Additionally, in the lower mantle there is also a low content of magnesiowüstite (MgO with 30% of Mg substituted by Fe) [10].

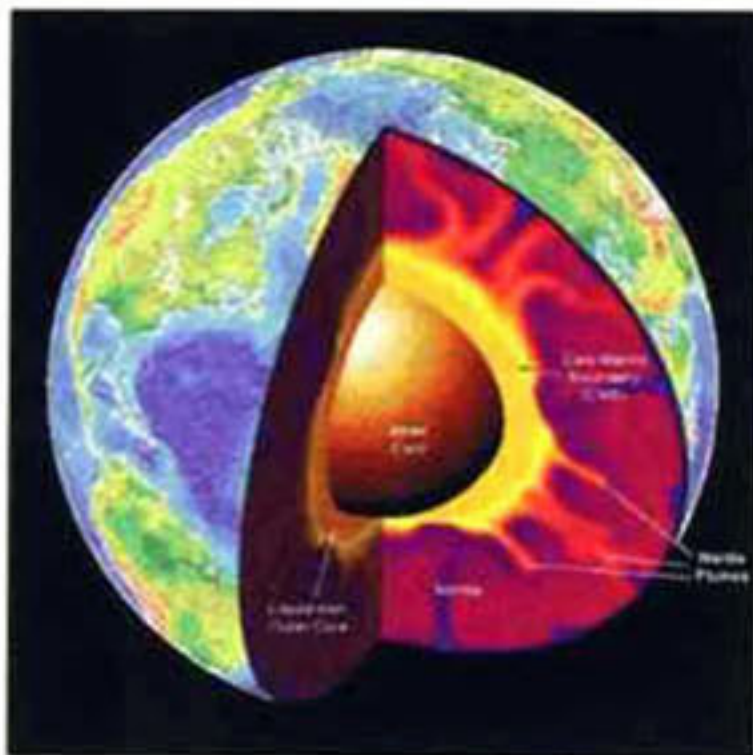


Figure 1.1: Structure of earth's interior, showing the major first-order seismic boundaries¹

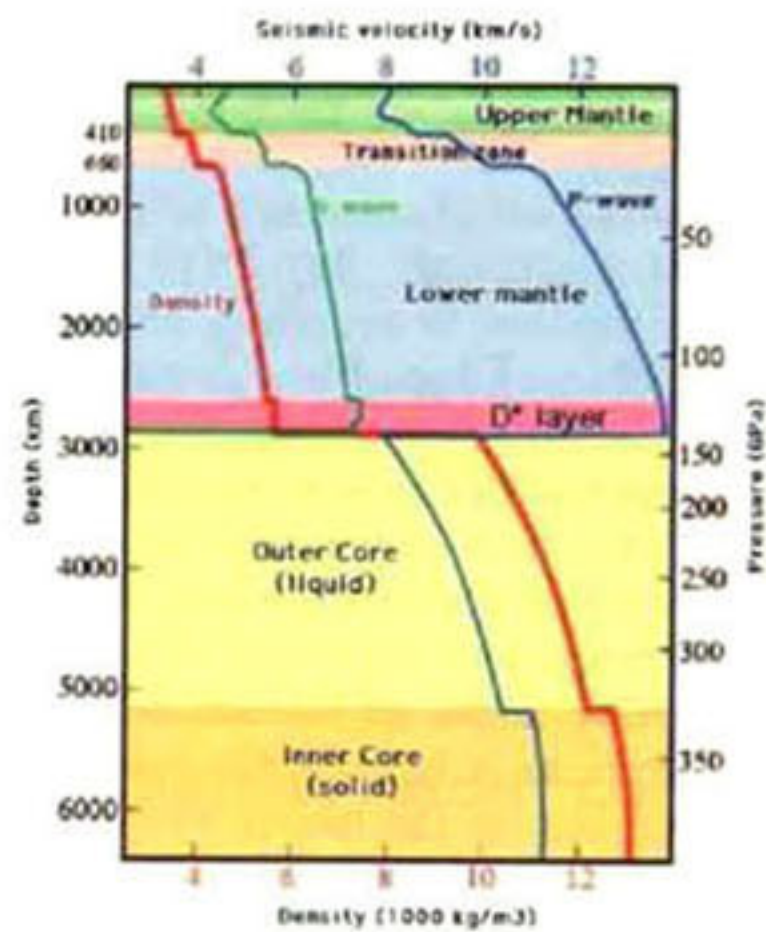


Figure 1.2: Density and wave velocity variations within the earth based on seismic observations. This model is called *PREM* after Preliminary Reference Earth Model²

¹This picture was taken from http://www.huttoncommentaries.com/subs/PSResearch/PS_Precursor/globe_w_core_labels.gif web site, Copyright 2000-2010, Hutton Commentaries, Inc. All Rights Reserved.

²This picture was taken from <http://my.opera.com/nielsol/blog/2008/11/13/core-mantle-boundary>, Ole Nielsen web site.

The core mantle boundary (*CMB*), called as well D'' layer is composed almost certainly of a new crystal structure of $MgSiO_3$ (post-perovskite). It is believed that the origin of the D'' seismic discontinuity and anisotropy may be attributed to the perovskite to post-perovskite phase transition [11].

There are several observations that have contributed to inferred the earth's core composition. For instance, it is known that the earth's must contain metallic elements in high concentration in order to generate its geomagnetic field. Cosmological abundance and meteoritics indicates that the core must consist mainly of *Fe*. Additionally, seismic measurements have shown that in the outer core shear waves are not transmitted. Since liquids do not support shear stresses, the conclusion is that this region is in liquid state. The metallic nature of the core is also beyond doubt because the only credible mechanism for the generation of the earth's magnetic field is based on convection-generated electric currents in the liquid outer core [10].

The *PREM* model state that the outer core density is about 10% less than that of liquid iron under the same temperature and pressure conditions. In spite of, it has been suggested that the outer core must be composed of liquid iron alloyed with 10wt% of lower atomic weight elements (lower than iron), plus about 4wt% of *Ni*. Due to its high cosmological abundance and other considerations the strongest candidates are *H*, *O*, *C*, *S* and *Si* (e.g. [2]). Among these elements, carbon is quite relevant because meets further constrains. From these five elements we are interested in iron alloyed with *C*, with the unit formula Fe_3C .

1.2 The Fe_3C compound

Iron Carbide, has a cementite structure (Fe_3X), is orthorhombic, space group *Pnma* with $Z = 4$. The unit cell contains 12 *Fe* atoms and 4 *C* atoms. Its cementite structure has been described as derived from a hexagonal closed packed arrangement composed of pleated layers [12] formed by trigonal prisms made by a *C* atom and its six nearest-neighbor *Fe* atoms [13]. The final cementite structure is form by the overlay of these sheets. Iron atoms occupy two different sites at the lattice with different local magnetic moment. The bonding in cementite is a complex mixture of covalent ionic and metallic contributions [13].

Iron Carbide Fe_3C (or $Fe_2C : Fe$) can be found in two different systems:

1. In its natural form (known as cohenite), as part of some iron-like meteorites mixed whit niquel and cobalt (figure 1.3).
2. As an intermediate metastable phase in the $Fe - C$ system (steel), which has led to the interest of the metallurgical field on this compound (figure 1.4).

To produce iron carbide an iron-carbon mixture is cooled from liquid to solid. Within this process two of the most important materials for the metallurgical industry are produce, steel and cast iron. The phase diagram of the $Fe - C$

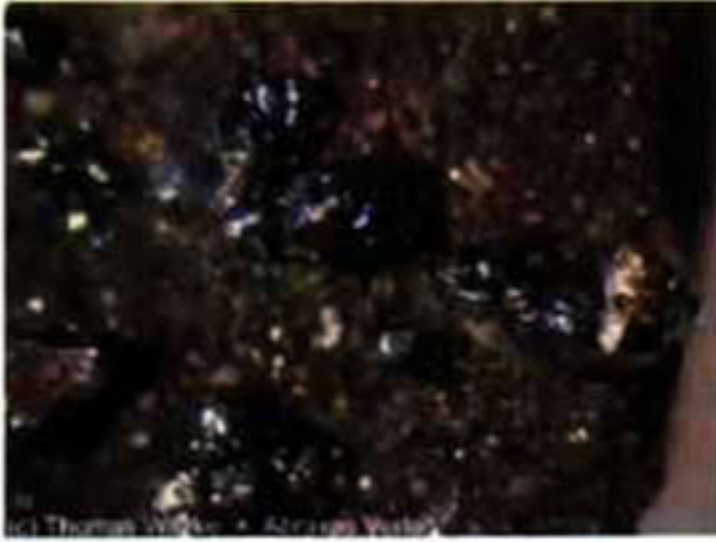


Figure 1.3: Cohenite mineral, natural iron carbide can be found in these iron-like meteorites³.

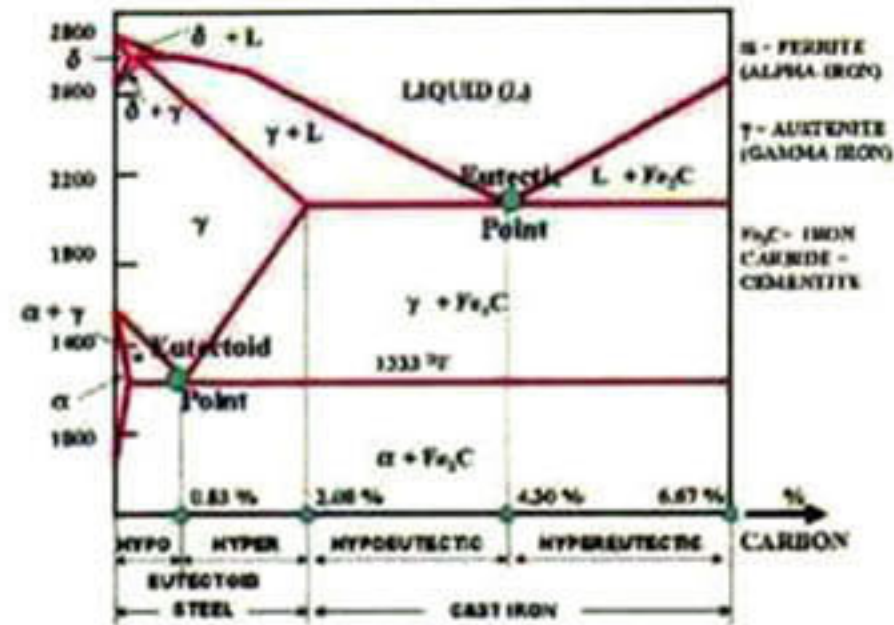


Figure 1.4: Phase diagram of the $F - C$ system⁴

system is shown in figure 1.4. The percentage of carbon determine the type of the formed alloy. Therefore, the most important feature of this system is the equilibrium between cementite and the several phases of iron, yielding to steel when $C < 2\%$. The equilibrium between graphite and the other phases yields to cast iron when $2\% < C < 4\%$. Cementite can be found alone as a metastable phase, when the mixture contains approximately 6.67% of carbon and 93.3% of iron.

At room temperature, Fe_3C is ferromagnetic. The transition to the paramagnetic state occurs at a Curie temperature, $T_C = 483^\circ K$ [14]. Recently, it has been observed that the volumetric thermal expansion coefficient of cementite is very temperature dependent, with the material showing a strong 'Invar effect' [14]. Cementite's magnetic character can be affected as well by pressure from a low-pressure magnetically ordered to a high-pressure non-magnetically ordered state [7].

1.3 What we know about Iron Carbide as a possible forming phase of the earth's inner core

Carbon alloyed with iron in the Fe_3C compound is a strong candidate for being an important forming phase of the earth's inner core. This assumption is based in the cosmological abundance of carbon in the universe. For instance, there is a high amount of carbon in the C1 carbonaceous chondrites (3.2wt%), which are the most common meteorites founded on earth (86%). The parents bodies of these meteorites are small to medium sized asteroids that were never part of any body large enough to undergo melting and planetary differentiation. Another possible evidence is the existence of cementite in its natural form (cohenite), as part of some iron-like meteorites mixed with nickel and cobalt. These mete-

³This picture was taken <http://www.webmineral.com/specimens/photos/CoheniteSmall.jpg> mineralogy database web site.

⁴This picture was taken from <http://info.lu.farmingdale.edu/depts/met/met205/fe3cdiagram.html>

orites are thought to be fragments of the core of some differentiated asteroids that have been shattered by impacts. This last is a good evidence of cementite presence on earth's core since not only iron-like meteorites but also terrestrial planets such as mercury and mars underwent mantle core differentiation and therefore its composition must be determined by the equilibrium process of accretion and subsequent differentiation.

Based on these assumptions *Wood* proposed that cementite might be the major phase forming the earth's inner core [3]. He also performed thermodynamic calculations and derived a equation of state which gave a density, incompressibility K_0 and its first derivative K' an a average inner core pressure of 338GPa, in agreement with the values obtained for density by *PREM* and the values measured by high pressure X-ray powder diffraction with diamond anvil cells experiments at room temperature for K_0 and K' [5],[4].

Cementite is ferromagnetic at ambient conditions, consequently the *EOS* derived by *Wood* was based on a ferromagnetically ordered cementite. However, the state of magnetization of Fe_3C can be affected either by temperature, from ferromagnetic to paramagnetic behavior ($T_C = 480^{\circ}K$ at room pressure) [6] or by pressure, from a low-pressure magnetically ordered to a high-pressure non-magnetically ordered state ($P = 60GPa$ at $0^{\circ}K$) [7]. Consequently, *Wood's EOS* is not necessarily accurate to model the earth's inner core, where high pressures and temperatures conditions will ensure that cementite will be in a non magnetically ordered state.

Nevertheless, recent multi-anvil press and laser-heated diamond anvil cell experiments have shown the stability of Fe_3C under high pressures and temperatures conditions. In particular, it was demonstrated that cementite is stable between $220^{\circ}K - 3700^{\circ}K$ and $25GPa - 70GPa$ [12]. Therefore, further studies are needed to constrain the possibility of cementite as a major phase in the earth's core.

Part II

Chapter 2

Theoretical Background

2.1 Introduction

This thesis proposal is a theoretical study of the electronic and structural properties of the Fe_3C compound under pressure. The methodology to be used is based on ab initio or first principles calculations, which now provide a well established methodology for the accurate prediction of properties of materials well beyond the pressures achieved by experimentation [15]. In particular this properties will be analyzed by means of Density Functional Theory (*DFT*), to take advantage of its high computational efficiency.

This chapter is devoted to the description of Density functional theory as well as the basic concepts under the Projected Augmented Wave method (*PAW*). In section 2.5 can be found a description of the code *ABINIT* through which the calculations were performed.

2.2 Ab initio methods

The accurate simulation of materials properties depend on an adequate quantum-mechanical description of the atoms, molecules or solids from which is made. Nevertheless, this task becomes impossible for anything beyond the simplest of systems without some approximations. The aim of the *Ab initio methodology* is the prediction of the electronic structure properties of atoms, molecules and solids, using a quantum mechanical approach of the many-body problem, i.e. by solving the molecular Schrödinger equation associated with the molecular Hamiltonian of a given system. The cleverness of this methods, lies in the use of several physical considerations that can be converted into feasible approximations. This makes possible to avoid the needful of a previous empirical knowledge of the system an allows an efficient computational treatment of the problem.

The core calculation of this method, is designed to obtain total energies, using as input only the atomic numbers of the constituents elements and their positions within the unit cell of a selected crystal structure [1]. This is essential since nearly all properties are related to total energies or to differences between

total energies [16]. In this way, the energy of a molecule, its vibrational frequencies, its thermodynamic properties or the values of its molecular orbitals, etc, can be computed.

2.3 Born Oppenheimer approach

The Born Oppenheimer approximation is a method to separate the variables corresponding to the nuclear and electronic coordinates in the Schrödinger equation associated to the molecular Hamiltonian. This is possible due to the fact that the mass of electrons is much smaller than the mass of ions. Hence, the nuclear velocities will be much more slower than the electronic velocities in such a way that the electrons will follow instantaneously the nuclear motion and relax to the ground-state of that nuclear configuration.

The many body Hamiltonian of a system can be expressed as:

$$\hat{H} = \hat{T}_n(\mathbf{R}_I) + \hat{V}_{nn}(\mathbf{R}_I) + \hat{T}_e(\mathbf{r}_i) + \hat{V}_{ee}(\mathbf{r}_i) + \hat{V}_{en}(\mathbf{r}_i, \mathbf{R}_I), \quad (2.1)$$

where \hat{T}_n and \hat{T}_e are the kinetic energy operators for the nuclei and electrons respectively. \hat{V}_{nn} and \hat{V}_{ee} are the potential energy operators for the nuclear and electronic interaction, and \hat{V}_{en} stands for the electron-nuclei interaction. These operators are defined as:

$$\begin{aligned} \hat{T}_n &= \sum_I -\frac{1}{2M_I} \nabla_I^2, & \hat{T}_e &= \sum_i -\frac{1}{2} \nabla_i^2, \\ \hat{V}_{nn} &= \frac{1}{2} \sum_{I \neq J} \frac{Q_I Q_J}{|\mathbf{R}_I - \mathbf{R}_J|}, & \hat{V}_{ee} &= \frac{1}{2} \sum_{i \neq j} \frac{1}{|\mathbf{r}_i - \mathbf{r}_j|}, \\ \hat{V}_{en} &= - \sum_{i,I} \frac{Q_I}{|\mathbf{R}_I - \mathbf{r}_i|.} \end{aligned} \quad (2.2)$$

In this set of relations, \mathbf{r}_i are the electronic coordinates. The sum I extends over all nuclei in the system, each with charge $Q_I = Z_I e$, mass M_I , and position \mathbf{R}_I in atomic units.

In view of the Born Oppenheimer approximation, one can solve the quantum mechanical problem (eq. 2.1) only for the system of electrons as if they were in an irrotational field due to fixed nuclei. Thus, the nuclear contribution to the total kinetic energy \hat{T}_n can be neglected. The resulting relation is known as the clamped Hamiltonian, that acts only on functions of the electronic coordinates,

$$\hat{H} = \hat{T}_e(\mathbf{r}_i) + \hat{V}_{ee}(\mathbf{r}_i) + \hat{V}_{en}(\mathbf{r}_i, \mathbf{R}_I), \quad (2.3)$$

and the electronic Schrödinger equation can be rewritten as:

$$\hat{H}\Psi = \left[\sum_i^N -\frac{\hbar^2 \nabla_i^2}{2m} + \sum_i^N V_{ee}(\mathbf{r}_i) + \sum_{i < j} V_{en}(\mathbf{r}_i, \mathbf{R}_I) \right] \Psi = E\Psi. \quad (2.4)$$

Even when the Born Oppenheimer approximation is considered, equation 2.4 is extremely difficult to solve. Several techniques has been developed to deal with it. There are two classes of methods:

- Wave function-based methods: In which an explicit form of the wave function is written down, then observables are calculated. Among these there are two subclasses; the perturbational methods, such as the Moller-Plesset diagrammatic methods and the variational methods, such as the post-Hartree-Fock conguration interaction (*CI*) method.
- Density-based methods: Instead of the wave function the electronic density is calculated. Examples are the Thomas-Fermi approximation and Density Functional Theory (*DFT*).

2.4 Density Functional Theory

The successful of *DFT* lies on the ability of the theory to map the many body problem that represents to solve the Schrödinger equation of a real system, into a problem based on electron density $n(\mathbf{r})$, which is a function only of three spatial coordinates. This theory was developed after Hohenberg and Kohn [17] demonstrate in 1964 that the ground state electronic density $n_0(\mathbf{r})$ contains exactly the same information as the ground state wave function $\Psi_0(\mathbf{r}_1)$.

2.4.1 The Hohenberg-Kohn theoremn

The aforementioned is the core of Hohenberg-Kohn's theorem. First they proved that the non-degenerated ground state wave function is a unique functional of the ground state density.

$$\Psi_0(\mathbf{r}_1, \mathbf{r}_2, \dots, \mathbf{r}_N) = \Psi [n_0(\mathbf{r})], \quad (2.5)$$

as a consequence, the ground state expectation value of any observable \hat{O} is a functional of $n_0(\mathbf{r})$ too. Among the most important observables is the ground state energy [18], that can be found by taking the the minimum value of the total energy functional i.e.,

$$E_{v,0} = E_v [n_0] = \min_{\Psi \rightarrow n_0} \langle \Psi | \hat{T}_e + \hat{V}_{ee} + \hat{V}_{en} | \Psi \rangle = \langle \Psi [n_0] | H | \Psi [n_0] \rangle, \quad (2.6)$$

therefore, the density that yields this minimum value is the exact single-particle ground-state density [16] and has the variational property,

$$E_v [n_0] \leq E_v [n'], \quad (2.7)$$

where n_0 is the ground state density in potential \hat{V}_{ee} and n' is some other density. To summarized, Hohenberg-Kohn's theorem can be stated as follows: the total energy of an electron gas (even in the presence of a static external potential) is a unique functional of the electron density. The minimum value of the total energy functional is the ground-state energy of the system, and the density that yields this minimum value is the exact single-particle ground-state density [16].

2.4.2 The Kohn-Sham method

Hohenberg-Kohn theorem is just the starting point in the execution of electronic structure calculations. The practical use of *DFT* is possible in a high extent, due to the work of W. Kohn and L. J. Sham [19]. In 1965, they introduce a set of equations that maps a system of interacting electrons, onto a fictitious non-physical system of noninteracting electrons in the presence of an effective potential. This potential, mimics the real system's many-particle electronic interaction, and is given by the next expression:

$$v_{effec}(\mathbf{r}) = v_{en}(\mathbf{r}) + v_H(\mathbf{r}) + v_{xc}(\mathbf{r}) \quad (2.8)$$

where, $v_{ee}(\mathbf{r})$ is the static total electron-ion potential of the interacting (many-body) system, $v_H(\mathbf{r})$ is the *Hartree* potential and $v_{xc}(\mathbf{r})$ is the *exchange-correlation* potential. Plugging relation 2.8 into Schrödinger's equation, one can obtaine an analogous single particle expression, i.e.,

$$\left[-\frac{\hbar^2 \nabla^2}{2m} + v_{effec}(\mathbf{r}) \right] \psi_i(\mathbf{r}) = \varepsilon_i \psi_i(\mathbf{r}). \quad (2.9)$$

The wave function $\psi_i(\mathbf{r})$ defines the single particle Kohn-Sham orbitals of the electronic state i , with eigenvalues ε_i . The key point of this method, is to set the electronic density $n_{effec}(\mathbf{r})$, equal to the ground state electronic density of the interacting system,

$$n_{effec}(\mathbf{r}) \equiv n_0(\mathbf{r}) = \sum_{i,N} f_i |\psi_i(\mathbf{r})|^2, \quad (2.10)$$

where, according to Pauli's exclusion principle, the fermionic occupation number f_i takes values between 0 and 2. In this way, it is ensured that $v_{effec}(\mathbf{r})$ reproduces the real system's many-particle electron-electron interactions, since $v_H(\mathbf{r})$ and $v_{xc}(\mathbf{r})$ are functionals of $n_0(\mathbf{r})$:

$$v_H(\mathbf{r}) = \frac{\delta \mathbf{E}_H [n_0(\mathbf{r})]}{\delta n(\mathbf{r})} = e^2 \int d^3 \mathbf{r}' \frac{n_0(\mathbf{r}')}{|\mathbf{r} - \mathbf{r}'|} \quad (2.11)$$

$$v_{xc}(\mathbf{r}) = \frac{\delta \mathbf{E}_{xc} [n_0(\mathbf{r})]}{\delta n(\mathbf{r})}. \quad (2.12)$$

The so called *Kohn-Sham equations* (eqs. 2.8, 2.9, 2.11 and 2.12), must be solved self-consistently (fig. 2.1) because they are non-linear relations. This means to take as input an initial density and then solve equation 2.8 with it. Next, $v_{effec}(\mathbf{r})$ is insert in equation 2.9 to find $\psi_i(\mathbf{r})$ from which a new $n(\mathbf{r})$ is calculated by means of equation 2.10, and used to start the cycle again. The cycle is stooped when a chosen convergence criteria is reached. With the resulting density, the ground state total energy E_0 is found. The latter, can be expressed as:

$$E_0[n(\mathbf{r})] = \sum_i f_i \varepsilon_i - \frac{e^2}{2} \int \frac{n_0(\mathbf{r})n_0(\mathbf{r}')}{|\mathbf{r} - \mathbf{r}'|} d\mathbf{r}d\mathbf{r}' + E_{xc} [n(\mathbf{r}')] - \int v_{xc}(\mathbf{r})n_0(\mathbf{r})d\mathbf{r} + E_{nn}(\mathbf{R}_I), \quad (2.13)$$

where the second term is the classical electrostatic self-interaction energy (Hartree term) of the electronic charge density distribution, and $E_{nn}(\mathbf{R}_I)$ contains the coulombic interaction among the ions.

2.4.3 Exchange correlation

The only unknown term in equation 2.13, is the *exchange-correlation* energy functional E_{xc} . This is a very complicated function of the electron positions, impossible to find exactly. The exchange part of E_{xc} , refers to the energy change of the system when two electrons of the same spin interchange positions. This happens because electrons are fermions, therefore its total wave function must be antisymmetric. The last, is a result of the Pauli's exclusion principle, which states that two electrons cannot be in the same quantum state. Moreover, each electron is affected by the motion of every other electron in the system, i.e. their motion is correlated; this is known as the correlation property [21].

Since the electron-electron interactions contained in the exchange-correlation energy functional E_{xc} , are very difficult to calculate, several methods have been conceived to approximate this property. The most simple of all, is the so called Local Density Approximation (*LDA*) in which the local exchange-correlation energy density is taken to be the same as in a uniform electron gas of the same density [22]. The exchange correlation functional under this approximation can be expressed as:

$$E_{xc}^{LDA}[n(\mathbf{r})] \approx \int e_{xc}^{hom}(n(\mathbf{r})) d^3r, \quad (2.14)$$

where, $e_{xc}^{hom}(n(\mathbf{r}))$ is the exchange-correlation energy per electron at each point in space of an homogeneous interacting electron gas of density $n(\mathbf{r})$. This method has shown to give good enough results for structural, elastic and vibrational properties. However, breaks down for systems with very strong electronic correlation, in which the charge densities are non-uniform (varies from point to point) an the exchange-correlation energy can deviate significantly from the uniform case. For instance, lattice constants and band gaps are underestimated while, cohesive energies and bulk moduli of solids are overestimated. To correct this deviation, the generalized gradient approximation (*GGA*) assumed that the exchange-correlation functional depends locally on the density as well as on the density gradient:

$$E_{xc}^{GGA}[n(\mathbf{r})] \approx \int f(n(\mathbf{r}), \nabla(\mathbf{r})) d^3r. \quad (2.15)$$

This method has proven to give a more realistic description of the relative stability of bulk phases, magnetism and cohesive energies of solids. Besides, *GGA* is computationally simpler than the *LDA* approximation.

2.4.4 Handling electron-ion interactions

Until this point it has been demonstrated that the many body problem of electron-electron interactions, can be mapped onto a fictitious non-physical system of noninteracting electrons in the presence of an effective potential (see section 2.4.2). Nevertheless, there still remains the formidable task of handling

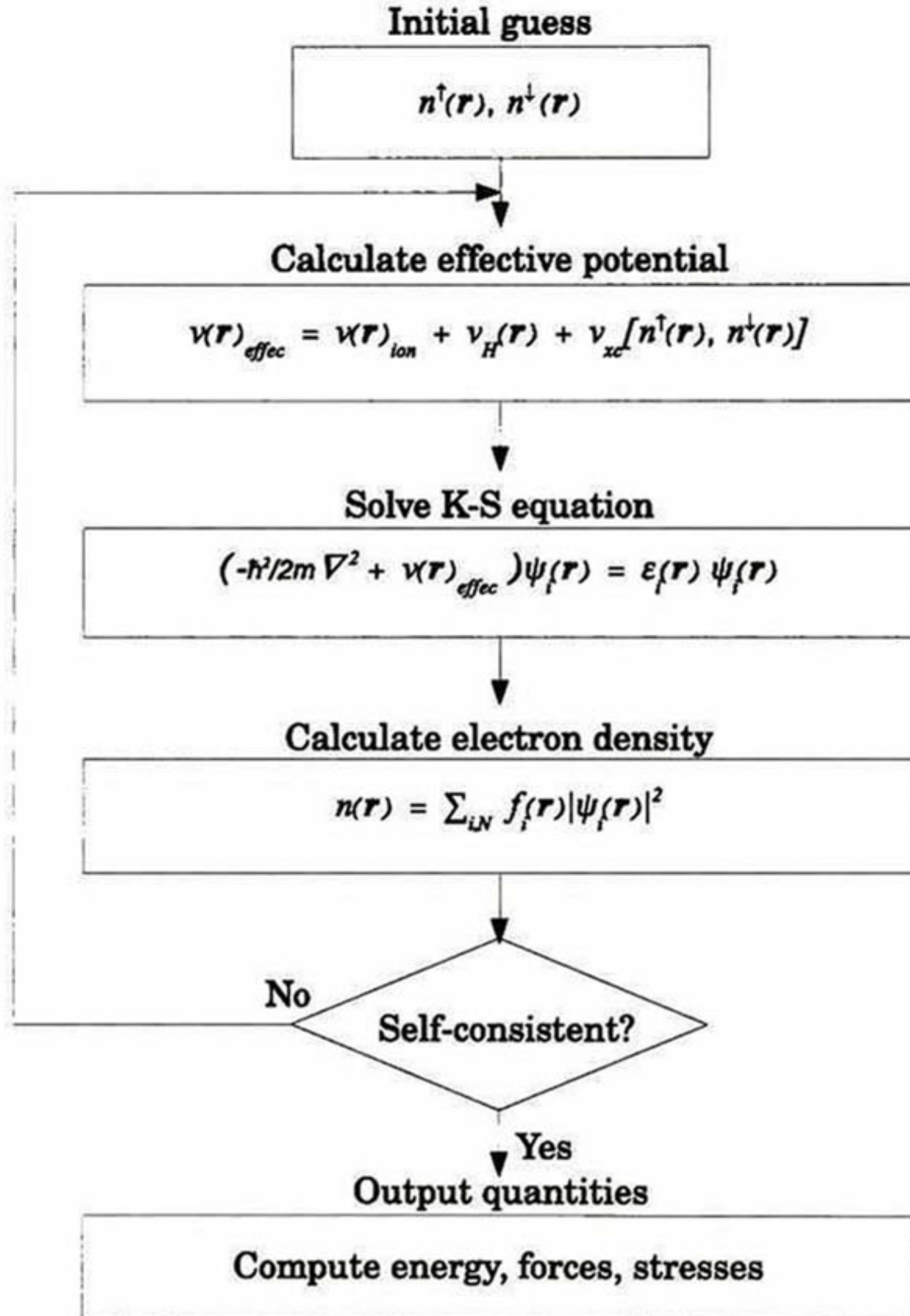


Figure 2.1: Schematic representation of the self consistent loop for solution of the Kohn-Sham equations. In general one must iterate two such loops simultaneously for the two spins, with the potential for each spin depending upon the density of both spins [20].

an infinite number of noninteracting electrons moving in the static potential of an infinite number of nuclei or ions [16].

To get a further reduction in the computational effort required to simulate these interactions, calculations are performed applying periodic boundary conditions through Bloch's theorem. This last, states that in a periodic solid each electronic wave function can be represented as a sum of plane waves [23]:

$$\psi_i(\mathbf{r}) = \sum_{\mathbf{G}} c_{i,\mathbf{k}+\mathbf{G}} \exp [i(\mathbf{k} + \mathbf{G}) \cdot \mathbf{r}], \quad (2.16)$$

this relation contains an expansion using a basis set of plane waves whose wave vectors \mathbf{k} are reciprocal lattice vectors \mathbf{G} of the crystal. With this picture, two basic problems derived from modeling electron-ion interactions, can be solved:

- There is no need to calculate a wave function for each electron in the system. This is possible because the electronic wave functions at \mathbf{k} points that are very close are almost identical. Then one can represent the electronic wave functions over a region of \mathbf{k} space by the wave function at a single \mathbf{k} point [16]. One of the most popular methods to calculate the electronic states using a small number of \mathbf{k} points in the Brillouin zone, has been devised by Monkhorst and Pack [24].
- There is no need of an infinite basis set to expand each electronic wave function. Since the coefficients $c_{i,\mathbf{k}+\mathbf{G}}$ for the plane waves with small kinetic energy are typically more important than those with large kinetic energy, the plane wave basis set can be truncated to include only plane waves with kinetic energies smaller than some particular cutoff energy [16]. This condition can be expressed as:

$$\frac{\hbar^2}{2m} |\mathbf{k} + \mathbf{G}|^2 \leq E_{cut}. \quad (2.17)$$

The magnitude in the error introduced by these approximations, can be reduced by using a denser set of \mathbf{k} -points, or a larger value of the cutoff energy respectively, but at the cost of increasing the computational effort. Thus, is very important to perform a convergence test (with respect to the \mathbf{k} -point sampling and the cutoff energy) of the property to be calculated.

2.4.5 Projector Augmented Wave Method

In the previous section (2.4.4), the advantages of considering periodic systems with electronic states that can be expanded in terms of plane waves basis set, have been elucidated. Even so, there still remain one issue that prevents the use of plane waves in order to make practical use of this approach. This difficulty is related with the different signatures of the wave function in different regions of space [25]. For instance,

- In the atomic region near the nucleus, the kinetic energy of the electrons is large, resulting in rapid oscillations of the wave function that require fine \mathbf{k} -point grids for an accurate numerical representation. On the other hand, the large kinetic energy makes the Schrödinger equation stiff, so

that a change of the chemical environment has little effect on the shape of the wave function. Therefore, the wave function in the atomic region can be well represented by a small basis set [26].

- In the bonding region between the atoms the situation is opposite. The kinetic energy is small and the wave function is smooth. However, the wave function is flexible and responds strongly to the environment. This requires large and nearly complete basis sets [26].

Several strategies have been developed to deal with this dilemmas. Among the most important are the Pseudopotential approach [27] and the Augmented wave methods [28, 29]. However, in the present work a different technique has been used, which is a natural extension of both methods. This is the so called Projector Augmented Wave Method (*PAW*) introduced by Peter Blöchl in 1994 [25].

Firstly, the *PAW* method treats different core and valence states. Core states are imported from those on an isolated atom. This is possible since core wave functions Ψ_c do not spread out into the neighboring atoms. Thus, the core wave function of the isolated atoms and the corresponding core wave functions of atoms immerse in a molecule or solid, must be identical.

To treat valence states, the *PAW* method introduces a linear transformation which produces only wave functions orthogonal to the core electrons,

$$\tau = 1 + \sum_R \hat{\tau}_R, \quad (2.18)$$

each local contribution $\hat{\tau}_R$ acting only within the core region Ω_R . This transformation, maps the true wave function Ψ_v with all its complexity onto proper auxiliary wave functions $\tilde{\Psi}_v$, that allow a computationally efficient treatment,

$$|\Psi_v\rangle = \tau|\tilde{\Psi}_v\rangle. \quad (2.19)$$

Additionally, the auxiliary wave function must be a smooth object (polynomial, gaussians or spherical bessel functions etc.) that can be expanded into auxiliary partial plane waves $|\tilde{\phi}_i\rangle$ inside the core region:

$$|\tilde{\Psi}_v\rangle = \sum_i |\tilde{\phi}_i\rangle c_i \quad \text{within } \Omega_R, \quad (2.20)$$

where the index i refers to the atomic site. Since $|\Psi_v\rangle = \tau|\tilde{\Psi}_v\rangle$, the corresponding true wave function Ψ_v is of the form,

$$|\Psi_v\rangle = \sum_i |\phi_i\rangle c_i \quad \text{within } \Omega_R, \quad (2.21)$$

with identical coefficients c_i in both expressions [25]. This set of partial waves $|\phi_i\rangle$ must be chosen to ensure a fast convergence to the Kohn-Sham wave function. A natural choice are solutions of the radial Schrödinger equation of the isolated atom, orthogonalized to the core states.

Moreover, since $1 + \hat{\tau}_R$ shall change the wave function only locally, the partial waves $|\phi_i\rangle$ and their auxiliary counter parts $|\tilde{\phi}_i\rangle$ are pairwise identical beyond the core region [26].

$$\phi_i(\mathbf{r}) = \tilde{\phi}_i(\mathbf{r}) \quad \text{outside } \Omega_R. \quad (2.22)$$

In order to determine the coefficients c_i , shall be remember that the transformation τ must be linear. As a consequence, the coefficients are linear functionals of the auxiliary wave functions. This condition can be expressed as:

$$c_i = \langle \tilde{p}_i | \tilde{\Psi}_v \rangle, \quad (2.23)$$

where $|\tilde{p}_i\rangle$ are projector functions. Then by inserting this coefficients into equation 2.20, is obtained:

$$|\Psi_v\rangle = \sum_i |\tilde{\phi}_i\rangle \langle \tilde{p}_i | \tilde{\Psi}_v \rangle \quad \text{within } \Omega_R, \quad (2.24)$$

which implies the completeness relation $\sum_i |\tilde{\phi}_i\rangle \langle \tilde{p}_i| = 1$, within Ω_R , so that the one center expansion 2.24 is identical to the auxiliary wave function $|\tilde{\Psi}_v\rangle$ itself. This indicates as well that,

$$\langle \tilde{p}_i | \tilde{\phi}_j \rangle = \delta_{i,j} \quad \text{within } \Omega_R, \quad (2.25)$$

i.e. the projector functions should be orthonormal to the smooth auxiliary partial waves inside Ω_R . There are no restrictions on \tilde{p}_i outside Ω_R , so for convenience, they are defined as local functions, i.e. $\tilde{p}_i = 0$ outside Ω_R . On the other hand, by analogy to equation 2.21, the transformation can be applied to the partial wave functions. This means that,

$$|\phi_i\rangle = \tau |\tilde{\phi}_i\rangle = (1 + \sum_R \hat{\tau}_R) |\tilde{\phi}_i\rangle, \quad (2.26)$$

therefore, the local contribution $\sum_R \hat{\tau}_R$ to the transformation operator is:

$$\tilde{\tau}_R |\tilde{\phi}_i\rangle = |\phi_i\rangle - |\tilde{\phi}_i\rangle. \quad (2.27)$$

If now we apply $\tilde{\tau}_R$ to equation 2.24,

$$\tilde{\tau}_R |\Psi_v\rangle = \sum_i \tilde{\tau}_R |\tilde{\phi}_i\rangle \langle \tilde{p}_i | \tilde{\Psi}_v \rangle \quad (2.28)$$

and insert equation 2.27, the transformation operator can be defined in terms of partial waves and projectors:

$$\tau = 1 + \sum_i (|\phi_i\rangle - |\tilde{\phi}_i\rangle) \langle \tilde{p}_i|. \quad (2.29)$$

Using this transformation the true wave function can be obtained from the auxiliary wave function by the following expression:

$$|\Psi_v\rangle = |\tilde{\Psi}_v\rangle + \sum_i (|\phi_i\rangle - |\tilde{\phi}_i\rangle) \langle \tilde{p}_i | \tilde{\Psi}_v \rangle \quad (2.30)$$

The advantages of this transformation are the following: First, by having separated the different types of waves functions, these can be treated differently.

Within the core region, can efficiently be represented on atom centered radial grids, while outside the core region, the wave functions are all smooth, thus it can be represented on coarse Fourier or real space grids [30]. Furthermore, the transformation τ consider the effects of the rapid oscillations of the true wave functions near the nucleus due to the strong attractive potential, into every expression in the *PAW* method, with the advantage that the soft auxiliary wave functions obtained can be represented with a modest number of plane-waves.

2.5 ABINIT

2.5.1 What does the code do?

The characterization of the compounds was made through the *ABINIT* [15, 31] code. This software is designed to performed density functional calculations of material properties. At the present, exists a large variety of codes that are able to perform electronic structure calculations, however, *ABINIT* has the advantage of been an open source software available under the *GNU* General Public License which makes it ideal for scientific research. Under this same spirit, was *ABINIT* created to be self-testing, self-documented and portable across platforms for serial and parallel execution.

ABINIT can perform density functional calculations, using a plane-wave basis and pseudopotentials, or the Projector Augmented Wave method [32]. For the latter, the atomic dataset containing the projectors \bar{p}_i , partial wave functions ϕ_i and auxiliary partial wave functions $\bar{\phi}_i$ can also be generated with the *AtomPAW* atomic data generator for the *PWPAW* package [33], [34] and then converted to *ABINIT's* format.

The exchange-correlation functional, can be treated as in the local density approach *LDA*, the generalized gradient approach *GGA* or as in *LDA + U*. The k-point sets can be generated automatically, following the MonkhorstPack scheme [24], or a generalization thereof. Symmetries are used to decrease the number of k-points needed to sample the Brillouin zone, so that only the irreducible part of it must be sampled. The treatment of state-dependent occupation numbers can be done in a number of ways, allowing the modeling of insulators, metals and semiconductors. Collinear magnetism can be handle (to simulate ferromagnetic and antiferromagnetic systems) using independent spin up and spin down wave functions, as well as spin orbit coupling, using spinor wave functions.

Density functional based calculations included in *ABINIT* can be divided in three major classes [15]:

Electronic ground-state capabilities

The electronic ground-state structure is calculated as follows: First, from the input initial atomic positions within the unit cell, *ABINIT* computes a set of eigenvalues and wave functions which achieve the lowest (*DFT*) energy possible for that basis set (that number of plane waves). The code takes the description of the unit cell and atomic positions and assembles a crystal potential from the

input atomic pseudopotentials, then uses either an input wave function or simple gaussians to generate the initial charge density and screening potential, then uses a self-consistent algorithm to iteratively adjust the plane wave coefficients until a sufficient convergence is reached in the energy¹. Once the ground state total energy is found, *ABINIT* can compute, the equilibrium lattice constants, density of states, and electronic band structure, among other properties.

Structure-related capabilities

When conducting structural optimization, *ABINIT* uses the *Broyden-Fletcher-Goldfarb-Shannon* minimization (*BFGS*) algorithm. In this method the optimized parameters (ionic positions and unit cell volume) are iteratively changed until the lowest energy configuration is reached. At each step a self-consistent single-point calculation is carried out to determine the forces acting on the ions and the stresses over the lattice parameters. The forces are computed through the *Hellmann-Feynman* theorem,

$$\mathbf{F}_I = -\frac{\partial E(\mathbf{R})}{\partial \mathbf{R}_I} = -\int n(\mathbf{r}) \frac{\partial V_{en}(\mathbf{r})}{\partial \mathbf{R}_I} d\mathbf{r} - \frac{\partial E_{nn}(\mathbf{R})}{\partial \mathbf{R}_I}, \quad (2.31)$$

where the subscript *I* stands for the nuclear positions. The electron-nuclei interaction $V_{en}(\mathbf{r})$, and the electrostatic ion-ion interaction are defined in equation 2.2. The computation of the stress tensor is performed under the same framework; lets consider a macroscopic an infinite solid of volume V , for which the internal stress is balanced by external forces applied at the same boundary. Such a stress is defined as the derivative of the total energy with respect to macroscopic strain, so the *Hellmann-Feynman* stress tensor can be expressed as:

$$T_{\alpha\beta} = \frac{\partial E(\mathbf{R})}{\partial \epsilon_{\alpha\beta}} = \frac{\partial E_{nn}(\mathbf{R})}{\partial \epsilon_{\alpha\beta}} + \int_V n(\mathbf{r}) \frac{\partial V_{en}(\mathbf{r})}{\partial \epsilon_{\alpha\beta}} d\mathbf{r}, \quad (2.32)$$

where the greek subscripts are cartesian components [35]. In this way, the equilibrium condition for the structural optimization is given by the condition on forces:

$$F_I = -\frac{\partial E(\mathbf{R})}{\partial \mathbf{R}_I} = 0. \quad (2.33)$$

In practice, this procedure continues until the forces and stresses converged to a minimum value, where the ground state equilibrium configuration is found. Forces and stresses can be used to generate an optimized structure using as well, the modified *Broyden* algorithm and *Verlet* algorithm. Molecular dynamics trajectories can be constructed, using the *Verlet* or *Numerov* algorithm.

Analogously, external hydrostatic pressure can be applied upon a crystal. The code performs a full optimization of cell size and shape iteratively, until the *Hellmann-Feynman* forces on the atoms are zero, and the *Hellmann-Feynman* stress tensor matches the one corresponding the imposed external pressure.

¹The information provided in this paragraph was taken from <http://www.abinit.org/documentation/helpfiles/for-v5.8/users/new-user-guide.html#6>

To avoid the *Pulay* error in the stress tensor [36], a smearing technique is applied to the kinetic energy that allows to get smooth energy curves as a function of the energy cut-off or lattice parameters, automatically including the *Pulay* stress. This error occurs, because the plane wave basis set is not complete with respect to changes of the volume. Thus, unless absolute convergence with respect to the basis set has been achieved during a structural relaxation, the calculation of the diagonal components of the stress tensor is incorrect. The error is almost isotropic, and has the effect to decrease the real fully relaxed volume.

Response-function capabilities

At the present, *ABINIT* deals with the responses to atomic displacements and static homogeneous electric elds, so that the phonon band structure can be constructed. From this, several thermodynamic properties are generated such as: the phonon free energy, the phonon internal energy, the phonon entropy and the phonon heat capacity. For insulators, one can obtain, the non-linear optical susceptibilities, the *Raman* tensor and the electro-optic coefficients. Dielectric polarization can be also computed within the *Berry* phase formulation for insulators, magnetic or non-magnetic systems, among several other capabilities.

Excited states can be computed in the framework of the Many-Body Perturbation Theory (*GW* approximation) or Time-Dependent Density Functional Theory (for molecules). Within the latter, *ABINIT* also allows the calculation of the frequency-dependent polarizability and optical spectra.

2.5.2 *ABINIT* reliability

ABINIT provide a equilibrium, between the number of atoms to be model, accuracy, speed of calculation and *CPU* memory needed. The accuracy of the properties that can be computed with *ABINIT*, relies on the chosen approximations and calculations methods. For instance, in the treatment of the exchange-correlation energy, the accuracy of the Local density approximation *LDA* for crystal bulk lattice constants is within 3%, but usually underestimated. This means that *LDA* hardens the bonds making the bulk modulus too large, (higher 10% error not uncommon for d-metals). Binding energies, activation energies in chemical reactions and relative stability of crystal bulk phases can be uncertain, however, electronic structure properties such as density of states and band structures are useful enough (except for band gaps)[37]. For band gaps a discrepancy of less than 0.2 eV can be achieved using instead the *GW* approach.

On the other hand, the Generalized Gradient approximation *GGA* corrects some of the *LDA* overbinding. *GGA* improves the accuracy in cohesive energies of solids, activation energy barriers in chemical reactions (but still too low), relative stability bulk phases and get a better description of magnetic solids [37]. In figure 2.2 are display the error in bulk lattice constant and cohesive energies calculations, for several materials with both these methods [38]. As can be seen from this figure, due to a more repulsive exchange-correlation *GGA* softens the bonds, increasing lattice constants (and decreasing the bulk moduli). In most cases, there is a notorious improvement in the accuracy of the calculation of lat-

tice constants with respect to the *LDA* approach. Nevertheless, in some others (*Ge* and *Cu*) the percentage error is almost the same for both approaches, so in this sense, there is not a consistent improvement over the *LDA* approximation.

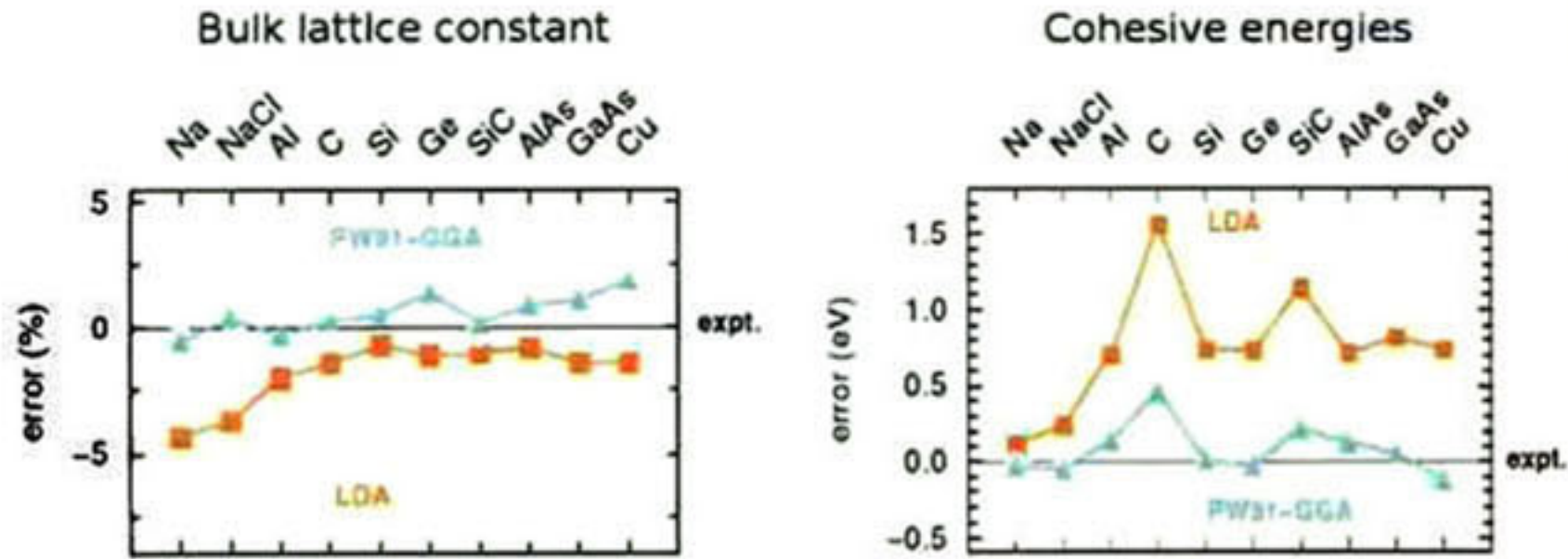


Figure 2.2: Comparisson of *LDA* versus *GGA* accuracy [38]

Concerning the Projected Augmented Wave method *PAW*, this predicts binding energies within a few tenths of an electron volt, bond lengths in the 1-2% range, and 15% for elastic constants. The *PAW* method gives the accuracy of all-electron calculations, given that the frozen core approximation is valid for the system considered, and that there are enough projector functions for all atoms. Hence is better to compare *PAW* calculations with results obtained by all-electron methods and not against pseudopotential methods, since these last only treat valence states.

Table 2.1, shows the lattice constant a and bulk moduli b for some selected crystals, as well as the magnetic moment of *Fe bcc* [39] calculated with several *ab initio* methods. These results were obtained using only one functional, namely *LDA*. As can be notice, the agreement between the results obtained with *PAW* and the different methods and experimental values is excellent.

The *PAW* formalism is only valid for non-overlapping augmentation regions (i.e the areas of space defined by core states). Therefore, great care should be taken to ensure that the distances between atoms are large enough to avoid overlap. Nontheless, in practice a small overlap ($\sim 5\%$) between spheres is acceptable, but an overlap of the compensation charge densities has to be avoided.

2.5.3 ABINIT parallelization

For ground-state calculations, the code has been parallelized on the k-points, spins, bands, and on the fast Fourier transform grid (*FFT*) and plane wave coefficients. For the k-point and spin parallelizations (using Multiprocessing by Message Passing *MPI* library of subroutines/functions), the communication load is generally very small. This allows it to be used on a cluster of workstations. However, the number of nodes that can be used in parallel might be small, and depends strongly on the physics of the problem. The band parallelization (also using *MPI*) can be used concurrently with the k point and and

Table 2.1: Properties of selected crystals, using the local density approximation and various methods that involve plane waves: norm-conserving pseudopotentials (NCPP), projected augmented waves (PAW), “ultrasoft” pseudopotentials (USPP) and linearized augmented plane waves (LAPW) [39].

Method	<i>C</i>		<i>Si</i>		<i>CaF₂</i>		<i>bcc Fe</i>		
	a	b	a	b	a	b	a	b	m
NCPP ^a	3.54	460	5.39	98	5.21	90	2.75 ^a	2.26 ^d	
PAW ^a	3.54	460	5.38	98	5.34	100			
PAW ^b	3.54	460	5.40	95	5.34	101	2.75	2.47	2.00
USPP ^b	3.54	461	5.40	95	5.34	101	2.72	2.37	2.08
LAPW ^a	3.54	470	5.41	98	5.33	110	2.72 ^d	2.45 ^d	2.04 ^d
EXP ^a	3.56	443	5.43	99	5.45	85-90	2.87 ^d	172 ^d	2.12 ^d

Since the results depend upon many details of the calculations, the values shown are mainly from two references that carried out careful comparisons: ^aHolzwarth, et al. [40] and ^bKresse and Joubert [41]. Other values for *Fe* are from ^cCho and Scheffler [42] and ^dStixrude, et al. [43]. References for experimental values are cited in [40] and [43]. This table has been taken entirely from reference [39].

spin parallelization, but is less efficient. The *FFT* grid parallelization (using Open *MPI*) works only for *SMP* machines, and is still to be optimized. Alternatively, a *MPI* version is under ²development.

²The information provided in this section was taken from http://www.abinit.org/documentation/helpfiles/for-v5.8/users/new_usr_guide.html#6

Part III

Chapter 3

Ground State Properties

3.1 Introduction

In this chapter we present an ab initio study of the ground state properties of the Fe_3C compound (cementite). We have calculated structural and electronic properties for several ground state energy configurations to identify which are the most energetically stable. The structural relaxation included different spin configurations in order to continuously change the system magnetization.

3.1.1 Thermodynamics

The total energy contained on an assembly made of atoms (molecules or periodic solids), is called the internal energy and can be viewed as the sum of the kinetic and potential energies of all the atoms. This physical property is very important, since almost all physical properties are related to total energies or to differences between total energies [16]. Therefore, if these differences can be computed, almost any physical quantity can be determined.

The first law of thermodynamics states that for an infinitesimal change within the system due to changes in the external environment:

$$dU = dQ - dW, \quad (3.1)$$

where U represents the internal energy, Q is the heat flow and W is the mechanical work made by or on the system. For instance, the change in volume due to the action of hydrostatic pressure, is given by:

$$dW = PdV, \quad (3.2)$$

and the enthalpy or heat content is given by,

$$H = U + PV, \quad (3.3)$$

Therefore, using equation 3.1,

$$dH = dU + PdV + VdP \quad (3.4)$$

Equation 3.3 is an equation of state that can be determined by first principle methods. At constant pressure (or fixed volume) and for a simple crystal in which the positions of the atoms in the unit cell are completely fixed by symmetry, one can carry out total energy first principle calculations repeated at different unit cell volumes and then determine the equilibrium volume and the ground state equation of state (eq. 3.3) of the system.

3.2 Methodology

The present results were obtained by using *DFT* as implemented in the *ABINIT*¹ software [15, 31]. The ground state relaxed geometry of Fe_3C was calculated as follows. First, the crystal structure of cementite was built from the experimental structure data [44], which provided the initial atomic positions within the unit cell, cell angles and lattice constants. Then, the structural optimization was performed, first, by modifying the ionic positions, fixing the cell and changing the inner parameters. From the relaxed coordinates obtained, a second calculation was carried out, relaxing only the volume, but allowing an homogeneous dilatation of the lattice parameters. Finally, a complete optimization of the cell geometry (nuclear positions and unit cell volume) was carried out over this configuration.

ABINIT performs the structural optimization using the *Broyden-Fletcher-Goldfarb-Shannon* minimization (*BFGS*) algorithm. In this method the optimized parameters (ionic positions and unit cell volume) are iteratively changed until the lowest energy configuration is reached. At each step a self-consistent single-point calculation is carried to determine the forces acting on the ions and the stresses over the lattice parameters. This procedure continues until the forces and stresses converged to a minimum value, and so, the ground state equilibrium configuration is found.

Once the relaxed structure at 0 *GPa* was stimated, the structure was compressed from 0 to 360 *GPa*, for all the spin configurations. The method included a full optimization of cell size and shape, combined with a target stress tensor to specify an external hydrostatic pressure applied upon the crystal from all three directions. This procedure was repited several times at different pressures, taking as input the optimized atomic positions calculated at a previous pressure, until the desired range of pressures was reached.

3.2.1 Computational details

The calculations were performed using the projector augmented wave method (*PAW*) [25], as implemented in *Abinit* [32]. The set of partial-waves and projector functions for each atomic species were taken from the *abinit* projector and basis functions database. Namely *Fe-GGA-sp_semicore-atompaw.paw* for iron and *C-GGA-hard.paw* for carbon and were generated with the computer

¹The *ABINIT* code is a common project of the Université Catholique de Louvain, Corning Incorporated, the Université de Liège, the Commissariat à l'Energie Atomique, Mitsubishi Chemical Corp., the Ecole Polytechnique Palaiseau (URL <http://www.abinit.org>).

program *AtomPaw*.

The exchange-correlation functional was described within the generalized gradient approximation (*GGA*) as parameterized by Perdew, Burke, and Ernzerhof (*PBE*). A plane-wave basis set was used with a cutoff energy of $16Ha$, while the energy cut-off for the fine "double grid" that allows the transferability from the normal fast Fourier transform (*FFT*) grid to the spherical grid around each atom, was set to $36Ha$. Additionally a $8 \times 8 \times 8$ Monkhorst-Pack k-mesh constructed in the full *Brillouin zone*, was used to define the number of k-points, in each of the three spatial dimensions [24].

3.2.2 Types of calculations

Since iron carbide (Fe_3C) was proposed to be a major phase present in the earth's core [3], there has been an avid dissertation about the effect of pressure on the magnetic state of this compound that impacts its physical properties. This situation has brought to light a shortcoming in the use of an equation of state based on an erroneous magnetic character. In view of this picture, we decide to perform a series of calculations considering different spin configurations and residual values in order to vary the magnetization of the system and to find out which spin arrangement is the most energetically favored in the considered pressure range. These calculations are:

1. **Non spin polarized (NS)**, for which spin up and spin down cannot be disentangled. Consequently this is a non magnetic configuration.
2. **Antiferromagnetic spin configuration (AFM-S)**, with a fixed local magnetic moment of atoms and providing a geometric configuration to ensure there are not magnetic domains (fig. 3.1). This structure belongs to the magnetic space group *Shubnikov type III Fedorov* space group $P2_12_12_1$ #19.
3. **Spin polarized**, with separate and different wave functions for spin up or spin down electrons for each band and k-point. This allow the atoms to have a net magnetic moment if that is the state that minimizes the energy of the system. The code determines at every self-consistent cycle, the spin-up and spin-down densities and the difference is define as the spin polarization or spin magnetic moment. Of these calculations, several possibilities were considered. These are:
 - **Ferromagnetic (FM)**, providing the initial electronic spin magnetization of each atom to break the symmetry.
 - **Antiferromagnetic (AFM)**, fixing the total magnetic moment to zero.
 - **Fixed magnetic moment (FMM)** to 0, 4, 8, 10, 12, 16, 20, 24, 36 and 48 Bohr's magneton calculations, which is the maximum number of unpaired electrons that the 12Fe atoms of the unit cell could contribute. An initial spin magnetization per atom to break the symmetry was included as well.

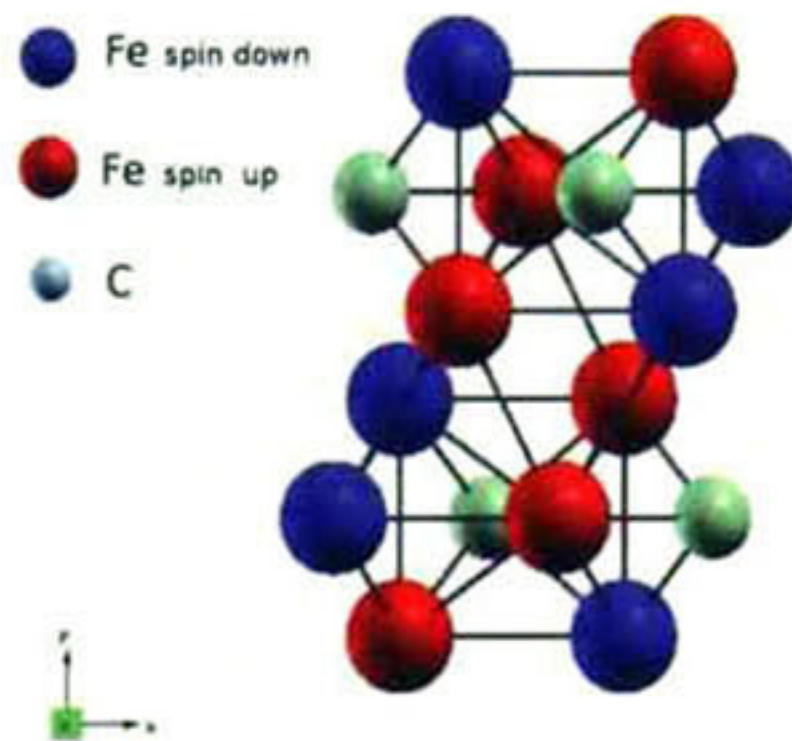


Figure 3.1: Unit cell for the Antiferromagnetic spin configuration (AFM-S). This structure belongs to the magnetic space group *Shubnikov type III Fedorov* space group $P2_12_12_1$ #19.

From this point, the abbreviations shown in parenthesis will be used in some cases when referred to the performed calculations for different types of configurations.

3.3 Results

3.3.1 Structural relaxation

Iron Carbide Fe_3C , has a cementite structure, and crystallizes in an orthorhombic space group $Pnma$ (*No.62*), with four formula units $Z = 4$ in the unit cell. The unit cell contains 12 Fe iron atoms and 4 C carbon atoms. Cementite unit cell [44] has been described as derived from a hexagonal closed packed arrangement composed of pleated layers [12] formed by trigonal prisms made by a C atom and its six nearest-neighbor Fe atoms [13]. These iron atoms occupy two different sites with slightly different magnetic moments. Within the trigonal prism there are two Fe atoms in special positions (labeled as Fe_s) which have 14 nearest-neighbor's with twelve $Fe_s - Fe$ bonds and two $Fe_s - C$ bonds; four iron atoms in general positions (labeled as Fe_g), also with 14 nearest-neighbor's but with eleven $Fe_g - Fe$ bonds and three $Fe_g - C$ bonds. The carbon atoms have 8 nearest-neighbor's. The Wyckoff positions of the atoms are $Fe_s(x1, y1, z1)$, $Fe_g(x2, 0.25, z2)$ and $C(x3, 0.25, z3)$. The final cementite structure is formed by the overlay of these sheets (fig. 3.2).

In table 3.1 and 3.2 are listed the equilibrium lattice constants at $0GPa$ obtained for the different configurations. The last three columns show the relative error with respect to the experimental data [44]. Since cementite exhibits a ferromagnetic behavior at ambient conditions, the calculated lattice param-

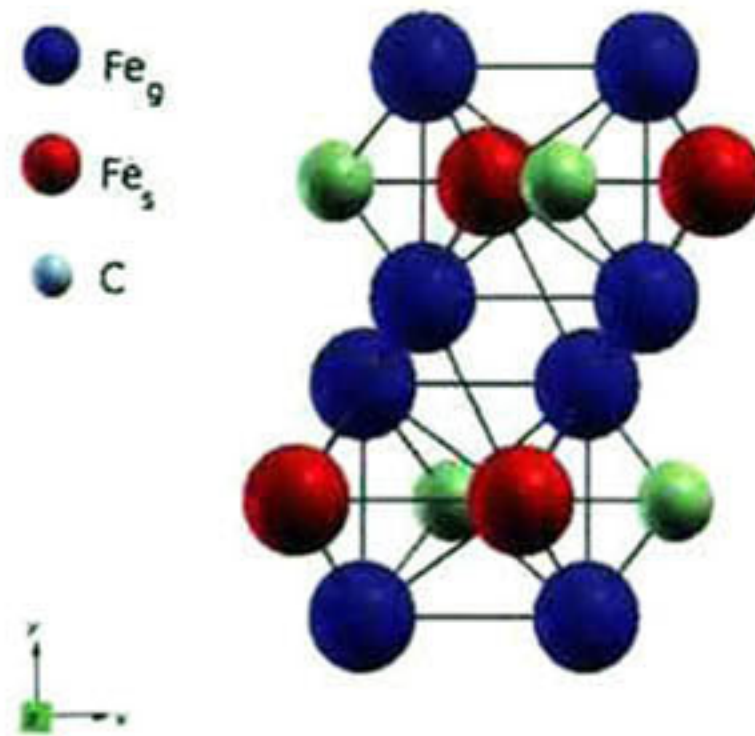


Figure 3.2: Unit cell of cementite, showing iron atoms in general positions Fe_g , special positions Fe_s and the four carbon atoms C .

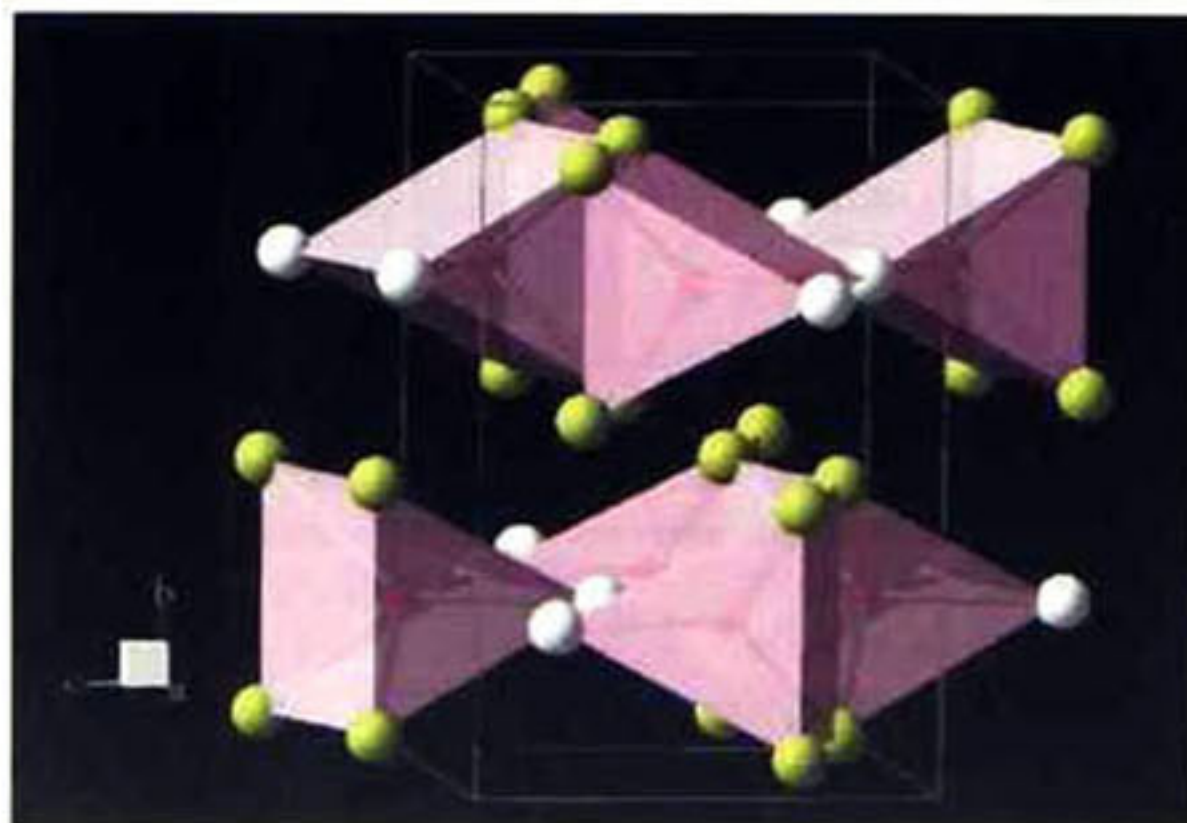


Figure 3.3: Crystal structure of cementite. Iron atoms in general Fe_g and special Fe_s positions, are shown as white and yellow spheres respectively, the carbon correspond to red spheres [13].

eters are in better agreement with experiment for those calculations in which the magnetic state of cementite has been considered. For example, the relative error in the ferromagnetic calculation (table 3.1) is less than 2% for all the three unit cell parameters and similarly, the relative error is lower than 2%, for those configurations with fixed magnetic moment between $16\mu_B$ and $24\mu_B$ (table 3.2). This is an excellent result that give us confidence in the capability of *DFT* to simulate ground state properties of materials.

Table 3.1. Unit cell parameters and volume V_0 at 0GPa

Configuration	V_0 (\AA^3)	a (\AA)	b (\AA)	c (\AA)	Err. a (%)	Err. b (%)	Err. c (%)
NS	144.380	4.916	6.684	4.394	3.27	0.73	2.81
AFM	144.359	4.916	6.683	4.394	3.27	0.74	2.81
AFM-S	145.496	4.938	6.698	4.399	2.83	0.52	2.7
FM	148.211	5.008	6.661	4.443	1.46	1.07	1.73
Exp. [44]	154.70	5.082	6.733	4.521			

Table 3.2. Unit cell parameters of Fe_3C and volume V_0 at 0GPa for fixed magnetic moment calculations (FMM).

Configuration	V_0 (\AA^3)	a (\AA)	b (\AA)	c (\AA)	Err. a (%)	Err. b (%)	Err. c (%)
<i>FMM</i> $\mu_0 = 0$	144.380	4.916	6.684	4.394	3.27	0.73	2.81
<i>FMM</i> $\mu_0 = 4$	146.256	4.950	6.706	4.406	2.59	0.41	2.54
<i>FMM</i> $\mu_0 = 8$	145.496	4.938	6.698	4.399	2.82	0.52	2.7
<i>FMM</i> $\mu_0 = 10$	145.818	4.947	6.693	4.404	2.65	0.59	2.58
<i>FMM</i> $\mu_0 = 12$	146.390	4.960	6.688	4.413	2.4	0.67	2.39
<i>FMM</i> $\mu_0 = 16$	147.955	4.996	6.676	4.436	1.69	0.84	1.87
<i>FMM</i> $\mu_0 = 20$	150.302	5.045	6.659	4.474	0.73	1.10	1.05
<i>FMM</i> $\mu_0 = 24$	153.429	5.100	6.644	4.528	0.35	1.32	0.15
<i>FMM</i> $\mu_0 = 36$	170.500	5.306	6.738	4.769	4.41	0.07	5.49
<i>FMM</i> $\mu_0 = 48$	201.763	5.450	7.360	5.030	7.24	9.31	11.26
Experimental [44]	154.70	5.082	6.733	4.521			

We have also calculated the inter-atomic distances in cementite. Figure 3.4, 3.5 and 3.7, show the computed bond lengths as a function of magnetic moment at the ground state ($P = 0GPa$). The data shown in these figures, corresponds to the fixed magnetic moment calculations FMM. The figures can be read as follows: the letters in the subscripts labels indicate the two possible sites for iron atoms ($g = general$, $s = special$) and the numbers refer to the specific location in the unit cell, that can be tracked from figure 3.6. For comparison it is depicted as well the bond length for the ground state stable phase of iron (Fe bcc) at its equivalent magnetic moment.

The net effect of magnetization is to expand the structure. Indeed the ground state volume obtained for the magnetic phases FM and AFM-S, is larger than that of the non-magnetic phases, NM and AFM calculation (table 3.1). The

3.3. F

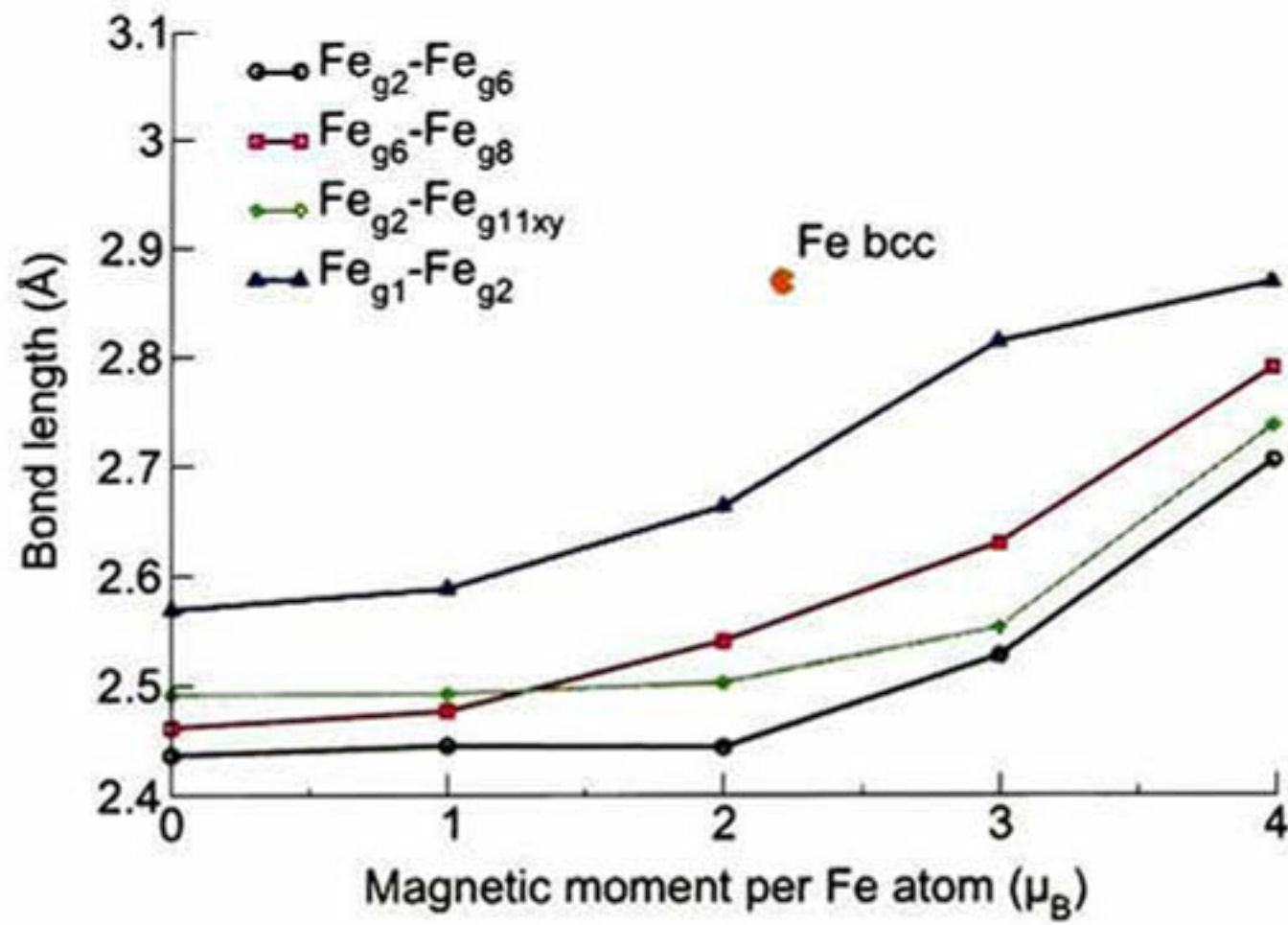


Figure 3.4: Bond lengths between iron atoms in general Fe_g positions. For Fe_{bcc} reference is [45]. Label Fe_{g11xy} indicates, that this atom is found when the unit cell in figure 3.6, is repeated one's along the x and y directions.

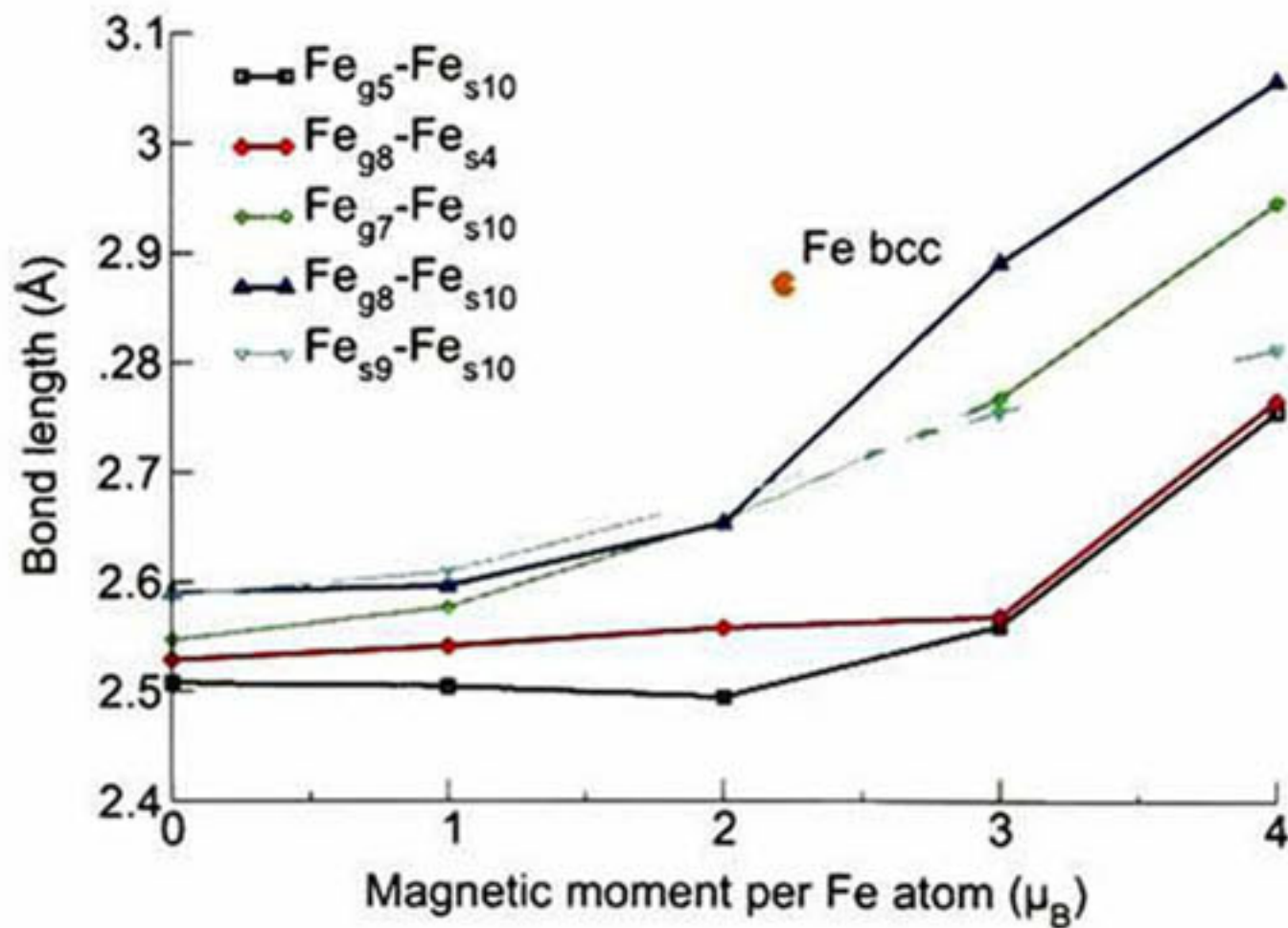


Figure 3.5: Bond lengths between iron atoms in general Fe_g and special Fe_s . For Fe_{bcc} reference is [45].

effect is more obvious from table 3.2, where one can see a constant increase of V_0 as a function of the magnetic moment for the FMM calculation.

Considering that carbon is much more smaller than iron, it seems at a first

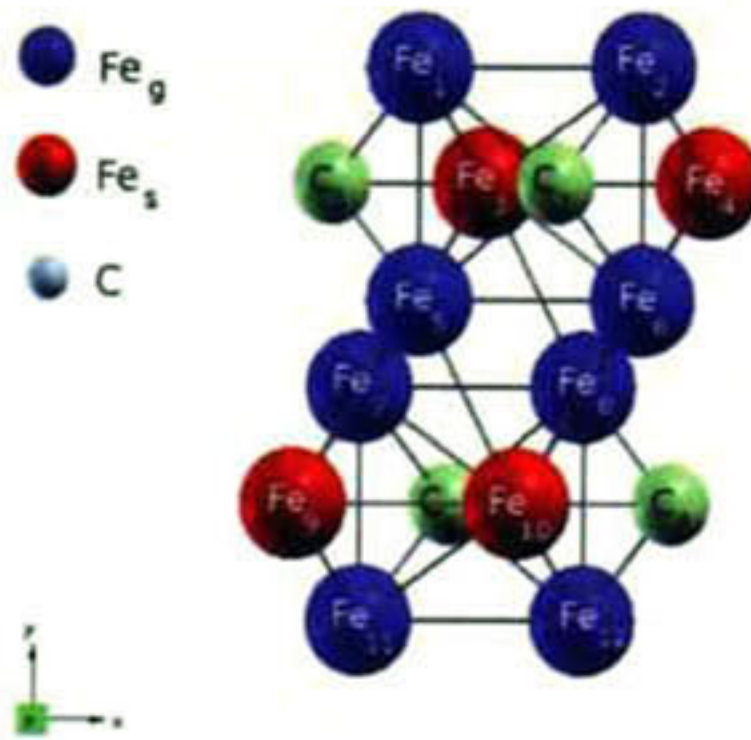


Figure 3.6: Unit cell of Fe_3C . This picture depicts the labels to identify the bonds.

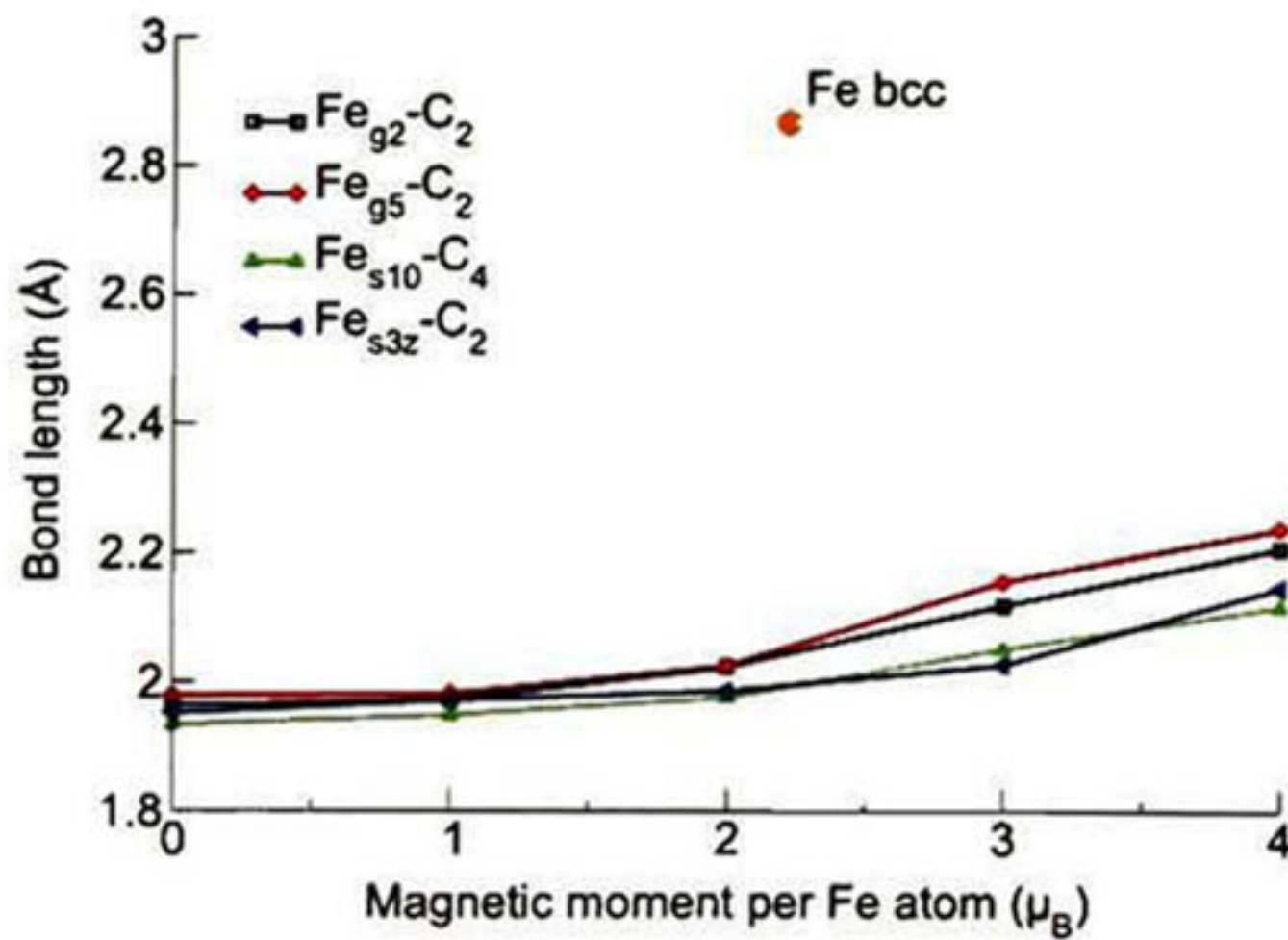


Figure 3.7: Bond lengths between iron and carbon atoms. For $Fe\ bcc$ reference is [45]. Label Fe_{s3z} indicates, that this atom is found when the unit cell in figure 3.6, is repeated one's along the z direction.

sight that the carbon atoms could occupy interstitial sites in the $Fe-Fe$ lattice. In fact, when carbon atoms are added interstitially to $Fe\ bcc$, the net effect is a volume expansion generated because carbon atoms push iron atoms apart increasing interatomic distances [46]. Nevertheless, from figure 3.4, 3.5, and 3.7 one can see that at the average magnetization per Fe atom of $Fe\ bcc$, all the interatomic distances of Fe_3C are smaller than those of iron, indicating

Table 3.3: Magnetic moment and inter-atomic distances in Fe_3C at 0GPa.

Magnetic moment (μ_B)	AFM-S	FM
$M_0 Fe_g$	0.5	1.38, 1.93 ¹
$M_0 Fe_s$	1.35	1.65, 1.98 ¹
$M_0 Fe$	0.93	1.45, 1.72 ² , 1.78 ³
Inter-atomic distance (Å)	AFM-S	FM
$d(Fe_{g2} - Fe_{g6})$	2.45	2.44
$d(Fe_{g6} - Fe_{g8})$	2.47	2.49
$d(Fe_{g2} - Fe_{g11z})$	2.50	2.49
$d(Fe_{g1} - Fe_{g2})$	2.57	2.61
$d(Fe_{g5} - Fe_{s10})$	2.52	2.49
$d(Fe_{g8} - Fe_{s4})$	2.54	2.54
$d(Fe_{g7} - Fe_{s10})$	2.56	2.60
$d(Fe_{g8} - Fe_{s10})$	2.59	2.61
$d(Fe_{s9} - Fe_{s10})$	2.59	2.63
$d(Fe_{g2} - C_2)$	1.96	1.99
$d(Fe_{g5} - C_2)$	1.97	1.99
$d(Fe_{s10} - C_4)$	1.97	1.98
$d(Fe_{s3xy} - C_2)$	1.95	1.96
$d(C_1 - C_2)$	3.01	2.95
$d(C_2 - C_4)$	4.21	4.22
$d(C_3 - C_2)$	5.08	5.21

¹ Theoretical value from reference [47]² Experimental value from reference [48]³ Experimental value from reference [49]

that the stability of Fe_3C is related to a different matter. In particular the $Fe-Fe$ distances range from 2.45 Å to 2.7 Å, which indicates a relative difference from pure Fe (2.86 Å) of 14.3% to 5.6% respectively. The same behavior was observed for the antiferromagnetic AFM-S and ferromagnetic FM structures and the results are displayed in table 3.3. From these same figures and more clearly from table 3.3, is evident that in Fe_3C all $Fe-C$ interatomic distances are smaller than $Fe-Fe$ distances. Meaning that $Fe-C$ interactions are stronger and probably covalent. If the covalent bonding dominates, this must be the main source, firstly because each carbon atom possesses six nearest-neighbor atoms, all iron: $2Fe_s$ and $4Fe_g$ and secondly because $C-C$ bonds are too far away from each other to play an important role. Actually $C-C$ interatomic distances in Fe_3C are about twice the bond length in pure carbon [46].

3.3.2 Magnetic properties

In table 3.3 are presented some of the magnetic properties of Fe_3C at the ground state (0GPa) for ferromagnetic FM and antiferromagnetic spin AFM-S configurations. Because of the covalent $Fe-C$ bonds in Fe_3C , the net magnetic

moment is smaller than that of iron ($2.29\mu_B$ [23]). In fact the existence of a $p-d$ hybrid band formed by the transferred $2p$ electrons of carbon atoms to the d electrons of iron atoms reflected on its density of states, is the main reason for the relative weakening of the Fe moment in cementite as compared to Fe bcc [50]. The average magnetic moment per Fe atom obtained was $\sim 1.45\mu_B$ in the ferromagnetic case and ~ 1.67 for fixed magnetic moment calculations (fig. 4.3 in next chapter).

There are some other factors affecting the magnetic state of iron atoms in Fe_3C , such as their coordination, the type of neighbors and the corresponding inter-atomic distances. These components are the reason for the difference in local magnetic moment of iron atoms at different positions. As can be observed, the local magnetic moment obtained for Fe_g iron atoms (see table 3.3) is smaller than that for Fe_s . This effect has been described before as a consequence of the stronger interactions between Fe_g and its iron environment. Due to shorter $Fe_g - Fe$ distances and the bonding interactions between Fe and C atoms ($d(Fe_g - C) > d(Fe_s - C)$), there is a reduction of the *exchange splitting*² of Fe_g d electrons that determine the lower local magnetic moments for Fe_g atoms [47].

For example, from figures 3.4, 3.5, 3.7, can be observed that the different kinds of atomic bonds follow the trend $d(Fe_s - Fe_s) > d(Fe_g - Fe_s) > d(Fe_g - Fe_g) > d(Fe_g - C) > d(Fe_s - C)$ [44]. This shows that the bonds between Fe_s atoms present the largest length, due to the higher electronic interaction which is reflected in a larger local magnetic moment. Additionally, the two main factors that determine the exchange splitting (shorter $Fe_g - Fe$ distances and $d(Fe_g - C) > d(Fe_s - C)$) are enhanced with increasing magnetic moment. All the above mentioned is true in the case of the fixed magnetic moment calculations FMM, but the interatomic distance tendency $d(Fe_s - Fe_s) > d(Fe_g - Fe_s) > d(Fe_g - Fe_g) > d(Fe_g - C) > d(Fe_s - C)$ is not followed so severely for the antiferromagnetic AFM-S and ferromagnetic calculations FM (see table 3.3).

To visualize the magnetism in Fe_3C , the spin polarization charge density ($\Delta n(\mathbf{r}) = n^\uparrow(\mathbf{r}) - n^\downarrow(\mathbf{r})$) maps for two different planes of the unit cell are shown in figures 3.8 and 3.9 for the FM and AFM-S configurations respectively. This charge density difference can be interpreted as a rough approximation of a local magnetic moment. As it can be observed, in the FM configuration the electronic charge density is located mainly around the iron atoms located at special positions Fe_s , which confirm our estimation of a higher local magnetic moment for these type of atoms.

For the AFM-S structure the situation is similar. The spin polarization charge density is located as well mainly around the iron atoms located at special positions Fe_s , but this time, there is a combination of spin down and spin up charge density (with the same absolute value for $\Delta n(\mathbf{r})$ but opposite in sign in the scale). The overall effect of this configuration is to cancel the local magnetic

²The exchange splitting refers to the separation between the spin-up and spin-down energy levels that results from the exchange interaction in magnetic systems.

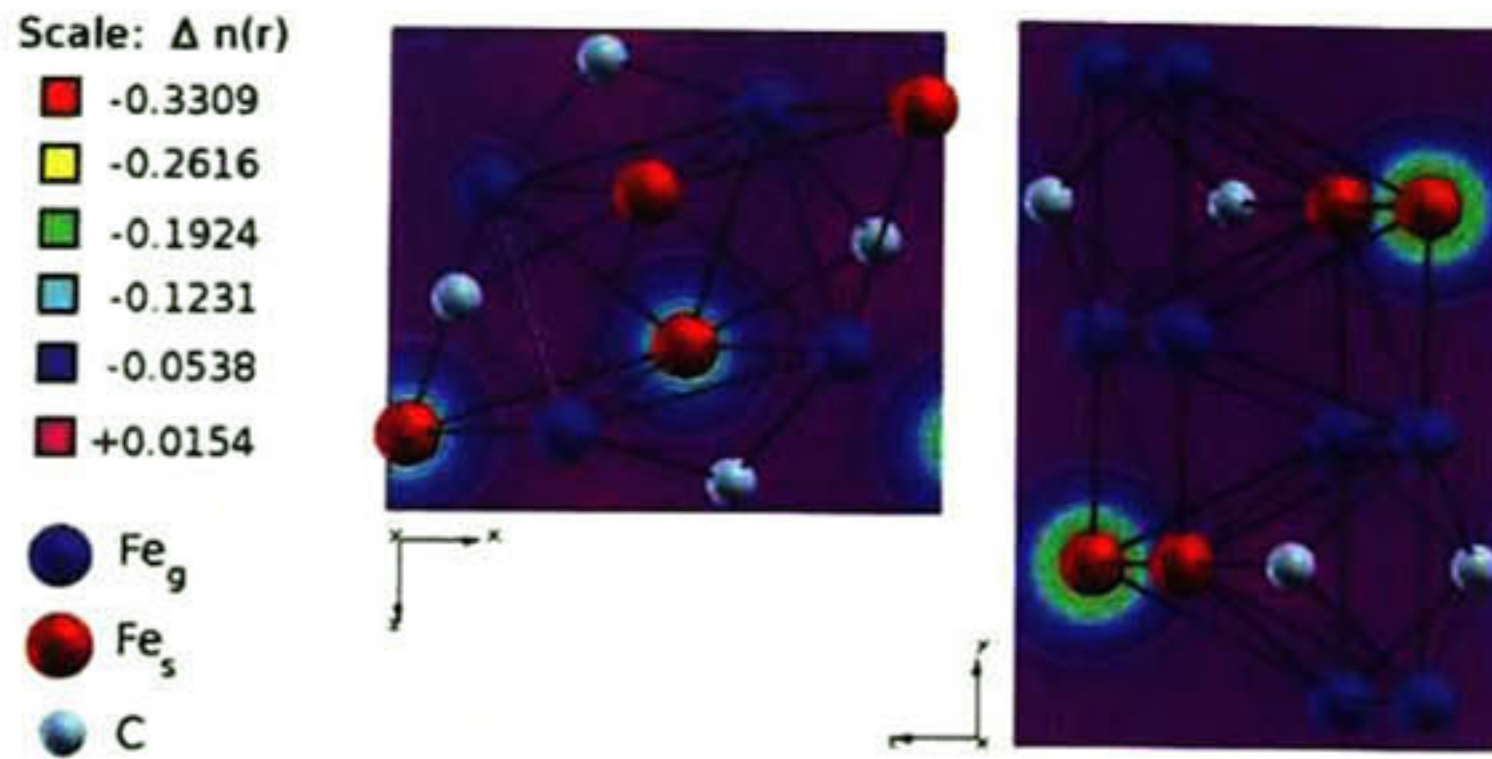


Figure 3.8: Polar charge density map for the ferromagnetic (FM) configuration.

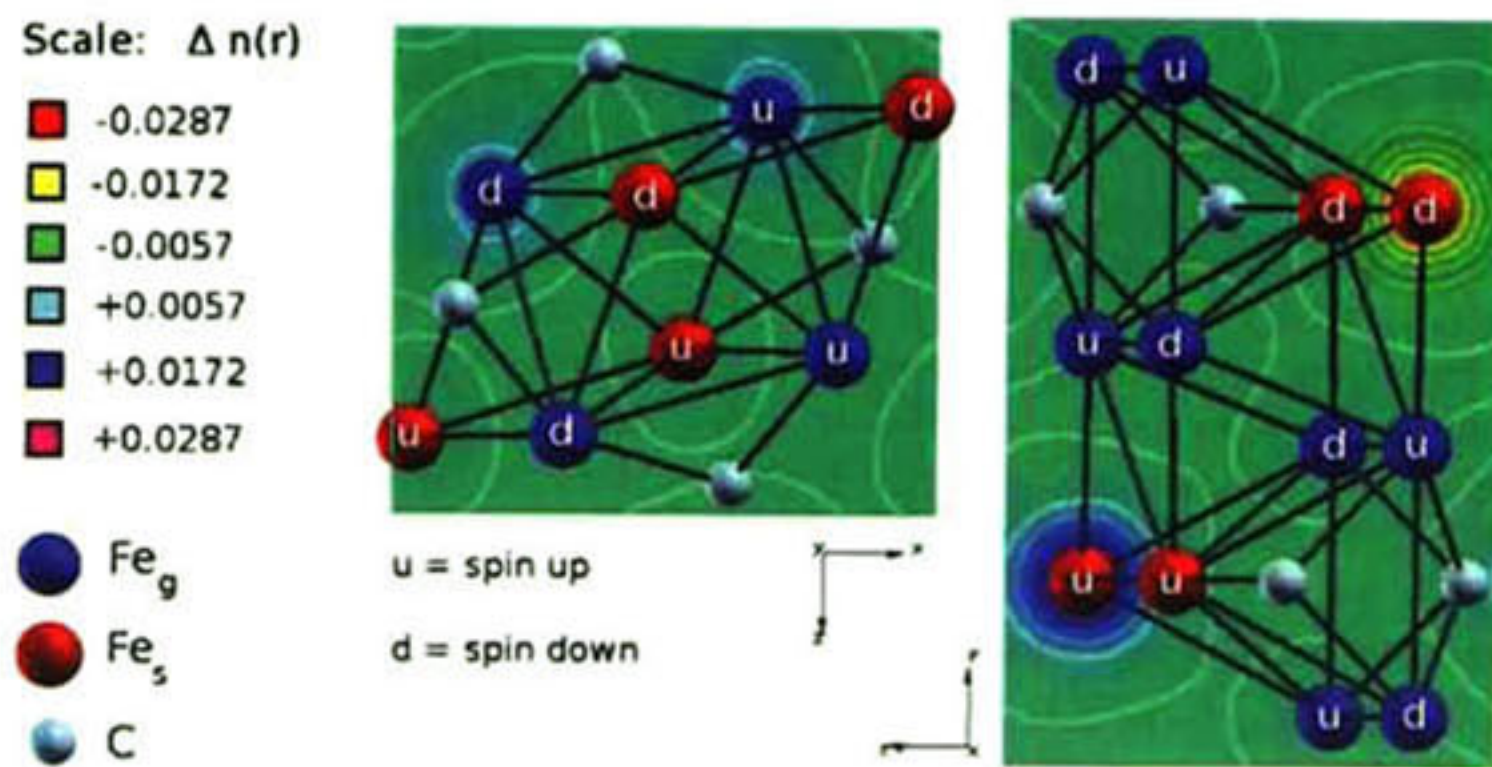


Figure 3.9: Polar charge density map for the antiferromagnetic spin (AFM-S) configuration.

moments of atoms and produce an antiferromagnetic material.

Part IV

Chapter 4

Effect of pressure on the magnetic state of Fe_3C

4.1 Introduction

The structural ground state properties of Fe_3C have been presented in chapter 3. In this chapter we aim to investigate in large detail the structural and magnetic evolution of Fe_3C , when subjected to pressure. Previous studies have shown that Fe_3C undergoes two main magnetic states under compression, that can affect its elastic, thermodynamic, and vibrational properties. For this reason, calculations over a large variety of spin configurations and residual values were performed in this study. All the configurations were compressed from zero to 300GPa . In this way the *EOS* was determined and the data was fitted to the third order *Birch-Murnaghan* equation of state.

4.1.1 Thermodynamics

The *Gibbs* energy G is a chemical potential that is minimized when a system reaches equilibrium at constant pressure and temperature. In consequence, between two phases of a material, phase 1 is more stable than phase 2 when $G_1 < G_2$, and the reverse is true when $G_2 < G_1$. The two phases co-exist in thermodynamic equilibrium when $G_1(P, T) = G_2(P, T)$, and this condition determines the relation between P and T on the phase boundary [9]. The *Gibbs* energy is defined as:

$$G(V, P, T) = U + PV - ST, \quad (4.1)$$

where U is the internal energy, S the entropy and T the temperature. Equation 4.1 can also be expressed in terms of the enthalpy H as,

$$G(V, P, T) = H + ST. \quad (4.2)$$

For a process at zero temperature, equation 4.2 indicates that $H(V, P) = G(V, P)$. Under this condition, the enthalpy can be used as the physical quantity that determines the stability of a system, and a transition between two phases can be established when both have the same enthalpy.

Under the *Ehrenfest* classification scheme, phase transitions are classified according to the degree of non-analyticity involved. For instance, a first-order phase transition involves a discontinuity in the first derivative of the *Gibbs* free energy with respect to a thermodynamic variable. In a second-order transition the first derivatives of the *Gibbs* free energy (or chemical potentials) are continuous but the second derivatives with respect to temperature and pressure (i.e. heat capacity, thermal expansion or compressibility) are discontinuous [51].

4.1.2 The invar effect

The invar phenomena refers to a decrease of the volumetric expansion coefficient, over some temperature range. It has been observed in several transition metal alloys. In the ground state Invar-type alloys, the atomic volume dependence of the binding energy incorporates a high-spin (HS) state in the vicinity of the equilibrium volume V_0 . At volumes about 5% less than V_0 , a low-spin (LS) is energetically favorable over the HS state [52]. Therefore this magnetostriction can be induced as well by pressure. Recently it has been observed that the volumetric thermal expansion coefficient of cementite is very temperature dependent, with the material showing a strong 'Invar effect' [14]. In this study we are concerned only about the magnetostriction effects induced by pressure, however some of our results can be used to elucidate the origin of the Invar phenomena in Fe_3C with respect to that in $Fe_{72}Pt_{28}$.

4.1.3 Equation of state

An equation of state is a relation that describes how a material behaves under a given set of physical conditions. In geophysics, we are particularly interested in those *EOS*'s concerning the thermodynamic state of solids under the influence of high temperature and pressure conditions, prevalent in the earth's interior. Nevertheless, for solids the effect of temperature is very light compared to gases and as a result it is commonly introduced only as a thermal expansion correction to the isothermal equation of state [14].

One of the most commonly used equations of state to fit high pressure volume-energy data, is the so called *Birch-Murnaghan EOS*. This relation is based on a non-linear, finite strain, elastic description, that takes into account that at high pressures it is more difficult to compress a solid. Under these circumstances the inter-atomic forces opposing further compression, generate large strains in the crystal volume and lattice parameters, which produces an enlargement of the bulk modulus at high pressures [9][53].

The third-order *Birch-Murnaghan* isothermal equation of state is given by,

$$P(V) = \frac{3K_0}{2} \left[\left(\frac{V_0}{V} \right)^{\frac{7}{3}} - \left(\frac{V_0}{V} \right)^{\frac{5}{3}} \right] \left\{ 1 + \frac{3}{4}(K'_0 - 4) \left[\left(\frac{V}{V_0} \right)^{\frac{2}{3}} - 1 \right] \right\}. \quad (4.3)$$

where V_0 and K_0 are the equilibrium volume and isothermal bulk modulus respectively and K'_0 is the first pressure derivative of K_0 . By integration of equation 4.3, an analogous equation of state for the energy can be obtained,

$$E(V) = E_0 + \frac{9V_0K_0}{16} \left\{ \left[\left(\frac{V_0}{V} \right)^{\frac{2}{3}} - 1 \right]^3 K'_0 + \left[\left(\frac{V_0}{V} \right)^{\frac{2}{3}} - 1 \right]^2 \left[6 - 4 \left(\frac{V_0}{V} \right)^{\frac{2}{3}} \right]^2 \right\}$$

where E_0 , stands for the equilibrium Helmholtz free energy.

The isothermal bulk modulus K is given by the expression,

$$K = -V \left(\frac{\partial P}{\partial V} \right)_T, \quad (4.4)$$

i.e. a volume derivative at fixed temperature. Additionally, the compressibility β is defined as the reciprocal value of the bulk modulus and represents the difficulty of changing the volume under pressure. Thus, a material with low compressibility β and high bulk modulus K would be very easy to compress.

4.2 Methodology

In order to investigate the structural and magnetic evolution of Fe_3C as a function of pressure, the ground state equation of state was determined from zero to 300 GPa for all calculations. Afterwards, the obtained $E - V$ data was fitted to a third order Murnaghan equation of state and estimated the zero pressure parameters such as its zero pressure volume V_0 bulk modulus K_0 and its first derivative K'_0 . The enthalpy was employed as the physical descriptor to define the stability of the structure and thus determined which of the proposed magnetic configurations is the most stable over the proposed range of pressures.

4.3 Results

4.3.1 Pressure-induced magnetic phase transition

In the search of the lowest-energy phase of Fe_3C among the calculated spin configurations, the enthalpy as a function of pressure was determined as shown in figure 4.1. To be more precise, this picture contains the difference between the enthalpy of one of the phases and the enthalpy of the non spin polarized configuration H_{NS} , i.e. $\Delta H = H - H_{NS}$. Calculating ΔH makes easier to distinguish between the stability one phase an another, since the difference become more numerically pronounced than for the enthalpy alone.

At high pressures, the non-magnetic phases considered, stabilizes over the magnetic configurations. However, the differences in enthalpy between the non-magnetic phases are within the computational error ($\sim \pm 1 mHa$), therefore, we assumed that at high pressures the magnetic state of Fe_3C is better modeled by the NS calculation. What happens at low pressures is more legible from figure 4.2, where the evolution of ΔH is plotted only to 30 GPa. Clearly in the low pressure regime the lowest enthalpy phase correspond to the ferromagnetic case. This result is in agreement with previous observations of the high spin to low

spin magnetic phase transition in Fe_3C [7].

Although this situation, the calculation of the FMM phases is well justified, since its curves intersect in a smooth manner, resembling the behavior of the FM configuration. In fact, at $0GPa$ the most stable phase correspond to the FMM calculations with $\mu_0 = 16\mu_B$ and $\mu_0 = 20\mu_B$, these two phases are degenerate and exhibit the lattice parameters and unit cell volume closer to the experimental value (see table 3.2). Is also important to note that between zero and $15GPa$, there is a lack of data at intermediate pressures for the FM calculation. Is in this region where the FMM calculations can provide a better insight of the evolution of the transition from a high spin to a low spin state.

Magnetic transitions like this have been observed as well by *XES* and synchrotron Mössbauer spectroscopy experiments for Fe_3S at approximately $21GPa$. Therefore is also possible to encounter a similar magnetic transition for other Fe_3X compounds [54].

The calculations of the antiferromagnetic phases, support the idea pointed out by Khmelevskiy *et al* [50], who observed that for Fe_3C "the transition occurs between a high moment ferromagnetic state and a non-magnetic (non-spin-polarized) state without stabilization of any intermediate antiferromagnetic-like state" However, there are a large number of ways in which antiferromagnetic configurations (of the type of the AFM-S) can be arranged for the crystal structure of cementite, therefore, the calculations presented in this work, can serve only to exclude them to be stable phases across the transition in Fe_3C . This feature is important to elucidate the origin of the Invar phenomena in Fe_3C with respect to that in $Fe_{72}Pt_{28}$. For the latter, Matsuhita *et al* [55], found experimental evidence of the formation of an intermediate antiferromagnetic-like phase between ferromagnetic and non magnetic phases under applied pressure. In addition a broad hysteresis was detected when high pressure X-ray magnetic circular dichroism (*XMCD*) measurements of a $Fe_{72}Pt_{28}$ disordered sample where performed [56]. This experiment showed different magnetic states with the same crystallographic structure under compression as compared when pressure was released from the sample. The appearance of the intermediate antiferromagnetic-like state in $Fe_{72}Pt_{28}$ could be the desire 'pinning' entity, which causes the observed hysteresis in $Fe_{72}Pt_{28}$, and if such a feature is absent in Fe_3C it may serve as an explanation for the difference in character of the transitions between these materials [50].

4.3.2 Magnetic transition parameters

Figures 4.3 and 4.4 show the evolution of magnetization as a function of pressure and volume respectively. For all three calculations, there is a collapse in local magnetic moment of iron atoms in Fe_3C , with increasing pressure or decreasing volume. Nevertheless, there are notable differences for each calculations. For the *AFM - S* calculation, the collapse doesn't represent a change on the magnetic state for the whole crystal. Instead for the *FM* and *FMM* structures this magnetic collapse is the responsible of the aforementioned magnetic phase transition. Additionally the drop in the local magnetic moment of iron atoms is larger for the *AFM - S* structure, and takes place in a smaller gap of pressures.

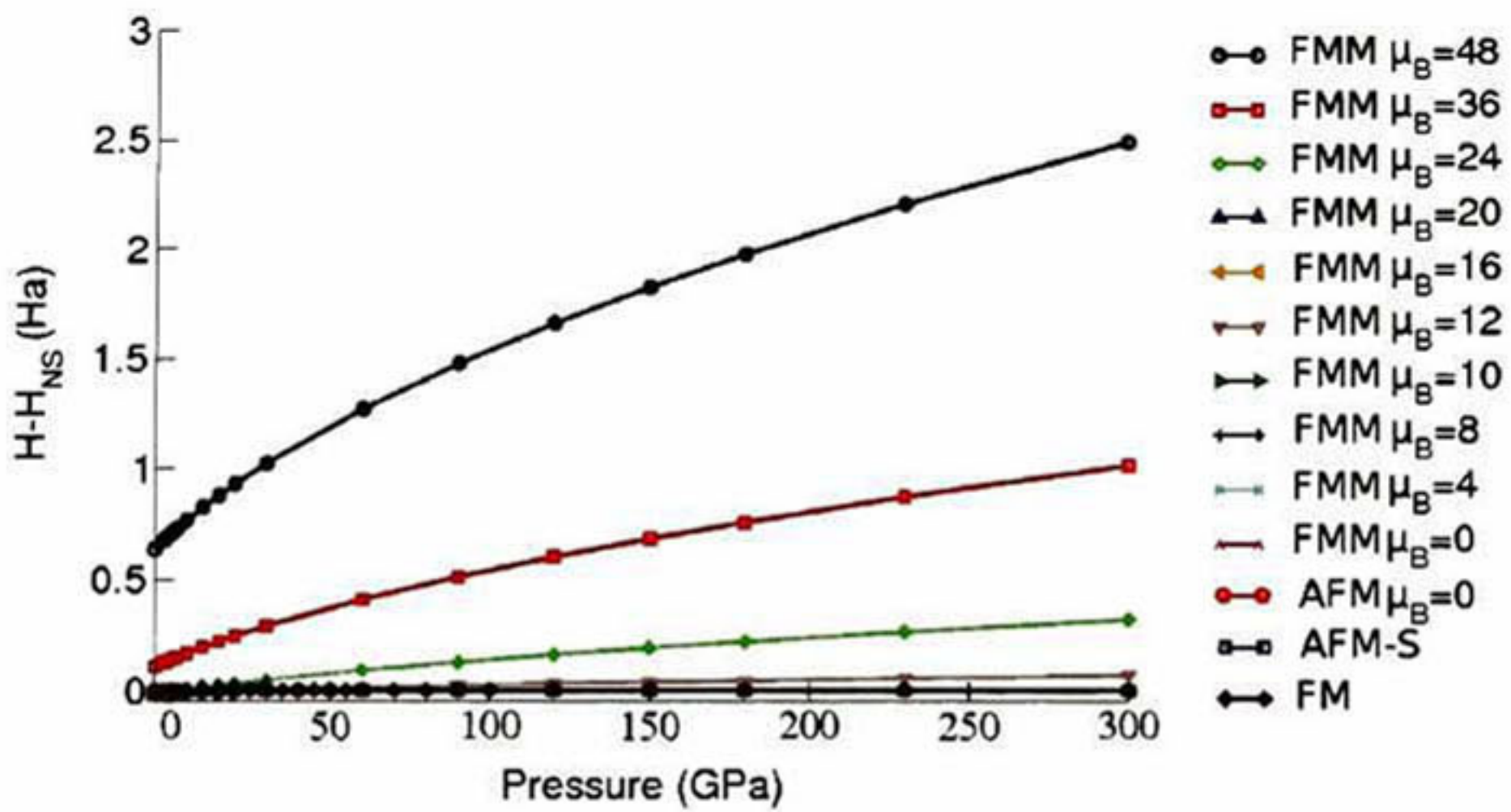


Figure 4.1: Relative enthalpy with respect to the non-spin polarized calculation, from zero to 300 GPa. For an explanation about the abbreviations corresponding to a type of configuration go to section 3.2.2.

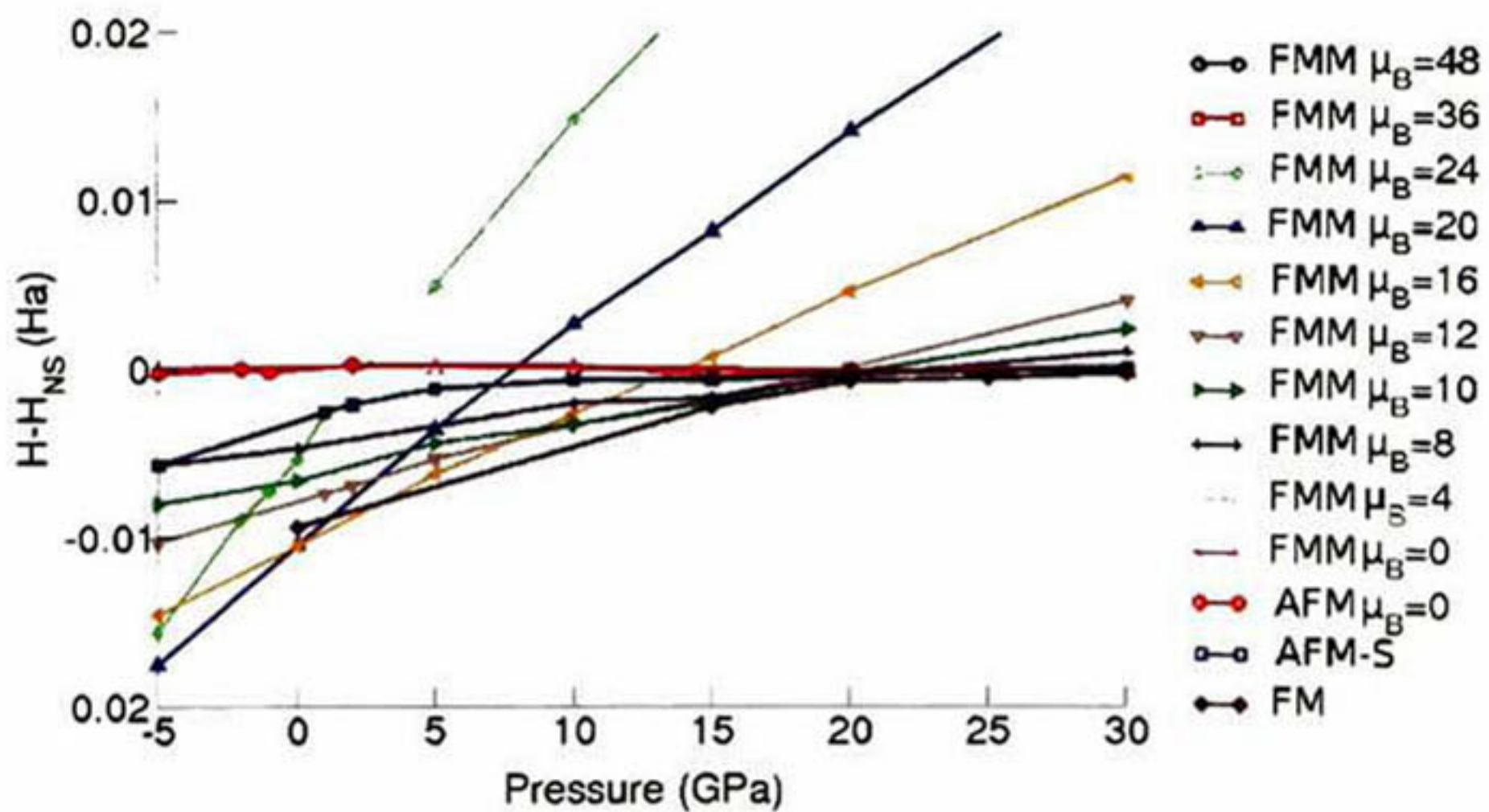


Figure 4.2: Relative enthalpy with respect to the non-spin polarized calculation H_{NS} , from zero to 30 GPa. For an explanation about the abbreviations corresponding to a type of configuration go to section 3.2.2.

In table 4.1 are enlisted the magnetic transition parameters for these three calculations, plus some available experimental and theoretical results concerning the effect of compression on Fe_3C . As can be observed there is a big discrepancy between the results obtained by these previous studies. For instance, experimental studies lack of accuracy because hydrostaticity is very difficult to achieve in practice. On the other hand, the pressure induced magnetic phase transition of cementite was predicted for the first time by Vocadlo et. al. [7], and they demonstrated as well that this transition affect the parameters necessary to defined a correct high pressure regime equation of state. Before this study, theoretical calculations didn't take into account this feature and end up with wrong results. In special, based on thermodynamical calculations, Wood et. al [3] predicted that cementite could be a major phase forming the earth's inner core. This assumption was derived from the determination of density at inner core conditions arising out of an equation of state that didn't consider this issue. Vocadlo et. al. come out with a different result, questioning the validity of this assumption. This study, pretends to bring light into this affair, by performing a more consistent study of the magnetic state of cementite at high pressures. It has been showed that the calculations presented here, portrait correctly the announced magnetic phase transition, and it would be pointed out more clearly that this calculations are in agreement with experimental evidence.

Comparison between experimental and theoretical results is not straightforward. The former are performed at room temperature and the later (if these are done by means of *DFT*) are calculated at zero kelvin since *DFT* can only calculate ground state properties.

Having pointed out this constrains, here there are some remarks:

In contrast to Wood et. al. in the present work it has been consider the correct magnetic state of cementite when subjected to pressure. By performing calculations over a large variety of spin configurations and residual values (FMM calculation) we were able to investigate the actual magnetic phase transition through a more reliable procedure than by performing spin polarized calculations. Here are presented both methods and the results are consistent with another. There is a shortcoming on executing spin polarized calculations to examine magnetic character. In many cases is common that from some start configuration the energy function has many local minima separated by large energy barriers. Codes often get trapped in a local-minimum spin state. Therefore it is difficult to determine the magnetization state of the arrangement. Trying different starting points can help, for instance by changing the initial electronic spin-magnetization for each atom to break the spin symmetry, allows to find stable local spin fluctuations. For this reasons this work represents a more systematic study of the magnetic character of Fe_3C under pressure than the one of Vocadlo et. al.

According to table, 4.1, the values of the transition volume V_T and the volume change associated to the magnetic collapse ΔV , corresponding to the FM and FMM calculations, are closer to the theoretical results obtain by Vocadlo et. al. than those obtained by Khamelevsty et. al.. ΔV was calculated by

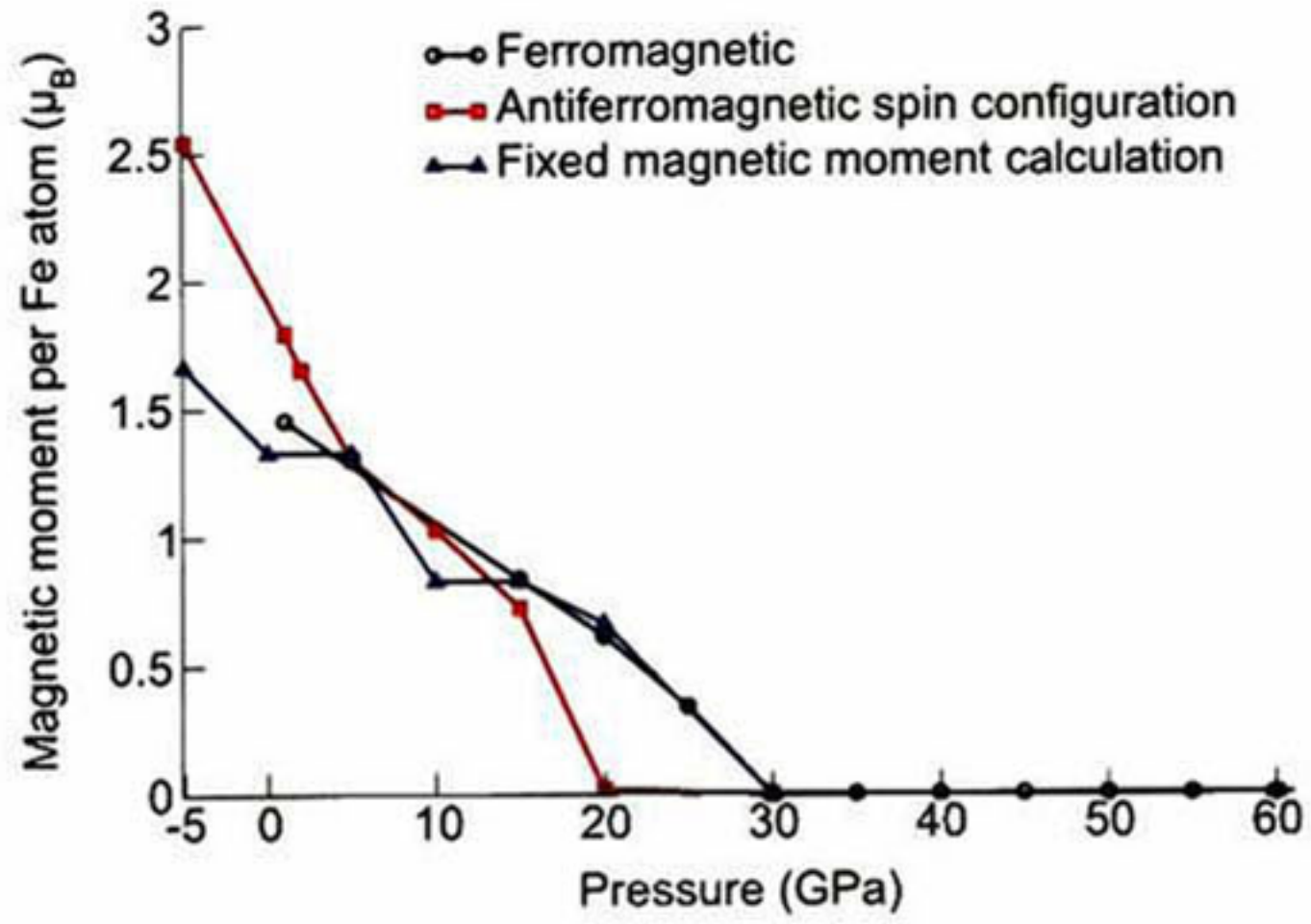


Figure 4.3: Magnetic moment as a function of pressure.

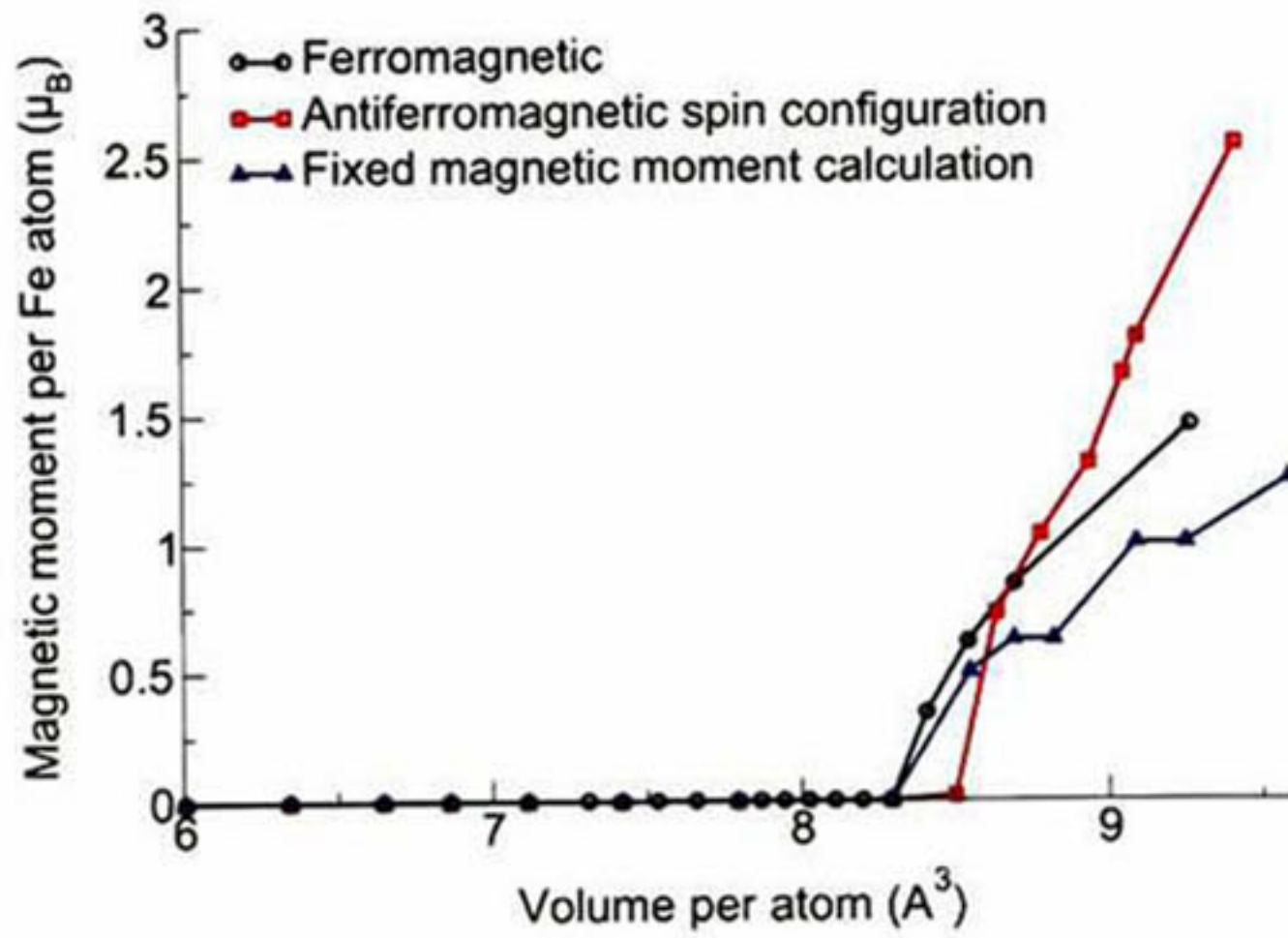


Figure 4.4: Magnetic moment as a function of volume

considering the difference in volume between the ground state V_0 volume and the transition volume V_T . Nevertheless the transition pressure P_T is far away from the value obtained by Vocadlo et. al..

Also important is that our results (V_T and ΔV) are more consistent with the experimental data showed in this table, than the results obtained by Vocadlo et. al.. A remarkable agreement is found for V_T and P_T with the results of Scott et. al. and Lin et. al.. It must be mentioned that the study of Scott et. al. consisted on a synchrotron-based x-ray diffraction experiment, hence the magnetic transition was not measured and no structural phase transition was detected. Nevertheless, the compression data clearly showed a discontinuity at 30 GPa in the axial ratios (c/a and b/a) and in the pressure-volume plot. Therefore V_T , ΔV and P_T showed in table 4.1 correspond to this discontinuity. There is more to be said about it, therefore we will come back to this in the next section 4.3.3. For the moment, it has been shown clearly enough, that the P_T lies near 30 GPa and not around 60 GPa as Vocadlo et. al. conclude.

These calculations show an improvement of accuracy with respect to the work performed by Vocadlo et. al. because the Projected Augmented Wave Method PAW to treat electron-ion interactions was used. Kresse et. al. [41] derived a formal relationship between both methods, and presented critical tests to compare the accuracy and efficiency of the PAW and the US-PP method with relaxed core all electron methods, paying particular attention to the bulk properties and magnetic energies Fe, Co and Ni. In contrast to the US-PP method employed by Vocadlo et. al., the PAW method demonstrated to give very accurate results for transition metals with large magnetic moment. In especial, its study of the structural properties of bcc ferromagnetic Fe and hcp non magnetic Fe, showed that the US-PP seriously overestimates the magnetic energy. Moreover, they evaluated the transition from the ferromagnetic bcc to non magnetic hcp phase and obtained (using PAW) a transition pressure in excellent agreement with other theoretical studies. However, the standard US-PP calculation predicted a transition pressure value too high in comparison with all the other methods. The same situation can be appreciated in table 4.1. The transition pressure obtained by Vocadlo et. al. is too high in comparison with theoretical calculations (including this study) and with experimental data.

4.3.3 Effect on Compressibility

During the compression the unit cell deforms in a continuous way and the material retains orthorhombic symmetry. Nevertheless, this deformation is not completely isotropic. Figures 4.5 and 4.6 give a clue about the deformation mechanism taking place. These figures show the relative axial compressibility for both ferromagnetic and fixed magnetic moment calculations, that is to say in which direction the structure compresses more relative to another axis at a given pressure. Note the presence of a small discontinuity; from 0 GPa to approximately 30 GPa the axial ratios a/b and a/c decrease while the b/c ratio increases significantly. This means that a is more compressible relative to c and b in the low pressure region, following the relative compression trend $a < c < b$. From this point the compression mechanism is inverted ($a > c > b$), and turns out to be quite isotropic at high pressures.

Table 4.1: Magnetic transition parameters for Fe_3C , showing ground state volumen V_0 , transition volumen V_T , pressure P_T and change of volumen required to induce the transition ΔV .

This study ^a	V_0 (\AA^3)	V_T (\AA^3)	ΔV (%)	P_T (GPa)
AFM-S	145.44	132.7	8.84	20
FM	148.16	132.7	10.50	30
FMM	150.24	132.7	11.75	30
Experimental ^b				
[5] Scott et al. ^d	155.26±.14	137.41	11.50	30
[4] Li et al.	155.2	No transition detected	-	No transition detected
[57] Lin et al	148	133.2	10	25
[58] Duman et al.	151	144	4.64	10-12
[59] Gao et al.	154.97	-	-	4.3-6.5
Theoretical ^c				
[3] Wood et al.	154.82	No transition predicted	-	No transition predicted
[7] Vocadlo et al.	143.36	126.4	11.83	60
[50] Khmelevstyi	150	145	3.33	-

^a Values at 0K.

^b Values at 300K.

^c Values at 0K except for refence [3] which were calculated at 300K.

^d No structural phase transition was detected, nevertheless, the compression data clearly showed a discontinuity at 30 GPa in the axial ratios (c/a and b/a) and in the pressure-volume plot. Therefore V_T , ΔV and P_T correspond to this dicontinuity.

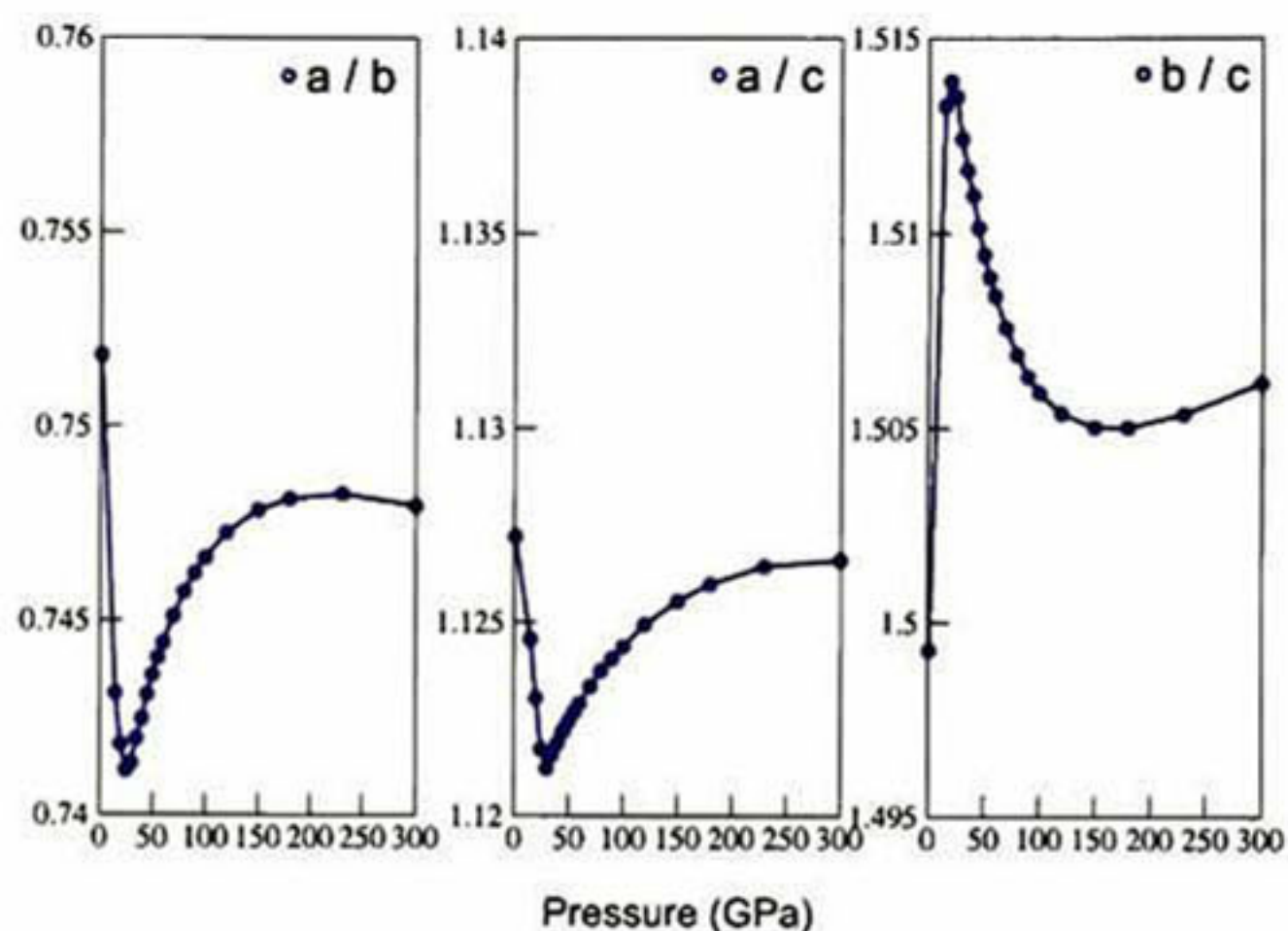


Figure 4.5: Relative compressibility for ferromagnetic (FM) calculation.

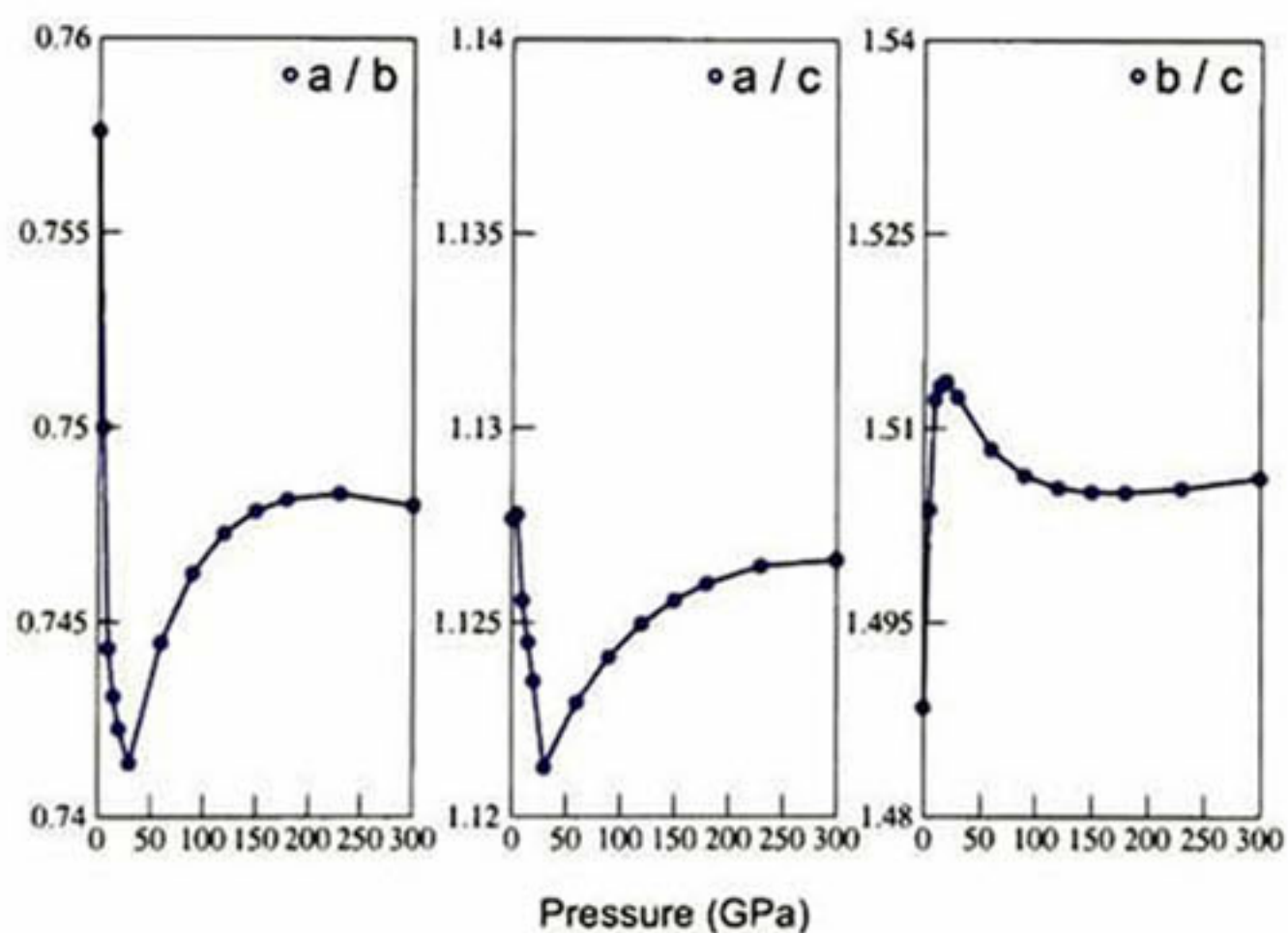


Figure 4.6: Relative compressibility for fixed magnetic moment (FMM) calculation.

To corroborate the above mentioned, the axial compression for both, ferromagnetic and fixed magnetic moment calculations, is depicted in figures 4.7 and 4.8. By this we mean the decrease in volume when the structure is subjected to hydrostatic pressure. The compressibility curve extracted from the fixed magnetic moment data, was constructed by taking the most stable magnetic phase

at each pressure (i.e. the minimal enthalpy configuration). With these data, the unit cell parameters evolution is thereby traced in a compressibility curve of the ratio $\frac{l}{l_0}$ as a function of pressure, l being any of the unit cell parameters at a given pressure and l_0 , any of the the unit cell parameters measured at $0GPa$. As expected, the a axis has the largest compressibility, followed by the compressibility of the c and b axis. The same trend is observed for both calculations, although this difference is greater for the constrained magnetic moment calculations.

It is also interesting to notice, that even when the discontinuity in the relative axial compressibility is small, it takes place approximately at the same pressure ($\sim 30GPa$) where the magnetic transition was identify in this study. There is another feature that supports the idea of this, being a consequence of the magnetic transition, namely, that a similar discontinuity in the a/b and a/c ratios has been observed at the same pressure, experimentally by Scott et. al. [5]. As has been already mention, that study consisted on a synchrotron-based x-ray diffraction experiment, hence the magnetic transition was no measured. Nevertheless, just as here, no structural phase transition was detected and there is a remarkable agreement between the magnetic transition parameters of such study, and this work (see table 4.1).

All of this means that the volume reduction due to the magnetic collapse is accompanied by a small structural rearregment that does not affect the whole symetry of the structure. In order to investigate this in more detail, the bond lengths and angle compressibility as a function of pressure, are depicted in figures 4.10, 4.9, 4.12 and 4.11 for both FM and FMM calculations. Only some of the most illustrative bonds an angles have been considered. Ones again, the letters in the subscripts labels indicate the two possible sites for iron atoms ($g = general$, $s = special$) and the numbers refer to the specific location in the unit cell, that can be tracked from figure 3.6. In addition, in figure 4.13 are displayed the considered angles with its respectives labels.

After a detailed analisis of figures 4.10, 4.9, 4.12 and 4.11, one can obtain the next observations holding for both calculations:

1. The angle $Fe_{g2} - Fe_{g6} - Fe_{g5}$ (figure 4.13 A) remains constant and as a result the bond $Fe_{g2} - Fe_{g6}$ is the less compressible.
2. The structure is been compressed more or less in the xz plane, accordingly the angles with larger positive compressibility (increasing value) are $Fe_{g4} - Fe_{g6} - Fe_{g5}$ and $Fe_{g1} - Fe_{s3} - Fe_{g2}$ (figure 4.13 B and G respectively).
3. By the contrary the angle with larger negative compressibility (decreasing value) is $Fe_{g6} - Fe_{s4} - Fe_{g8}$ (figure 4.13 D). While the angle $Fe_{g4} - Fe_{g6} - Fe_{s10}$ (figure 4.13 E) remains almost constant.
4. This means that the upper and lower part of the structure, are getting closer along to the line that joins atoms Fe_{g6} and Fe_{g8} (see the arrows in figure 4.13 D and E). This is corroborated by the fact that the bond $Fe_{g6} - Fe_{g8}$ presents the smaller compressibility.

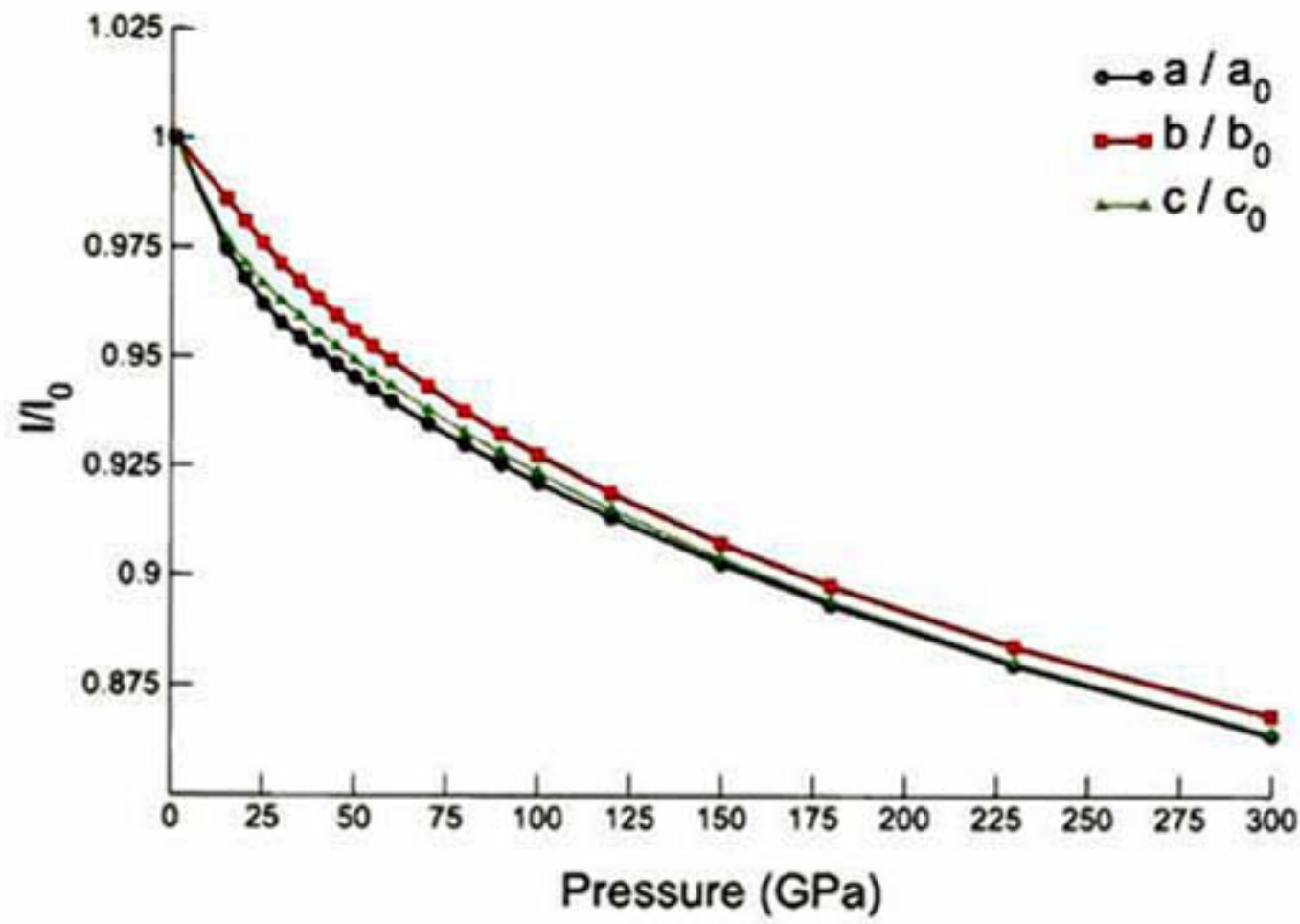


Figure 4.7: Compressibility for fixed magnetic moment (FMM) calculation.

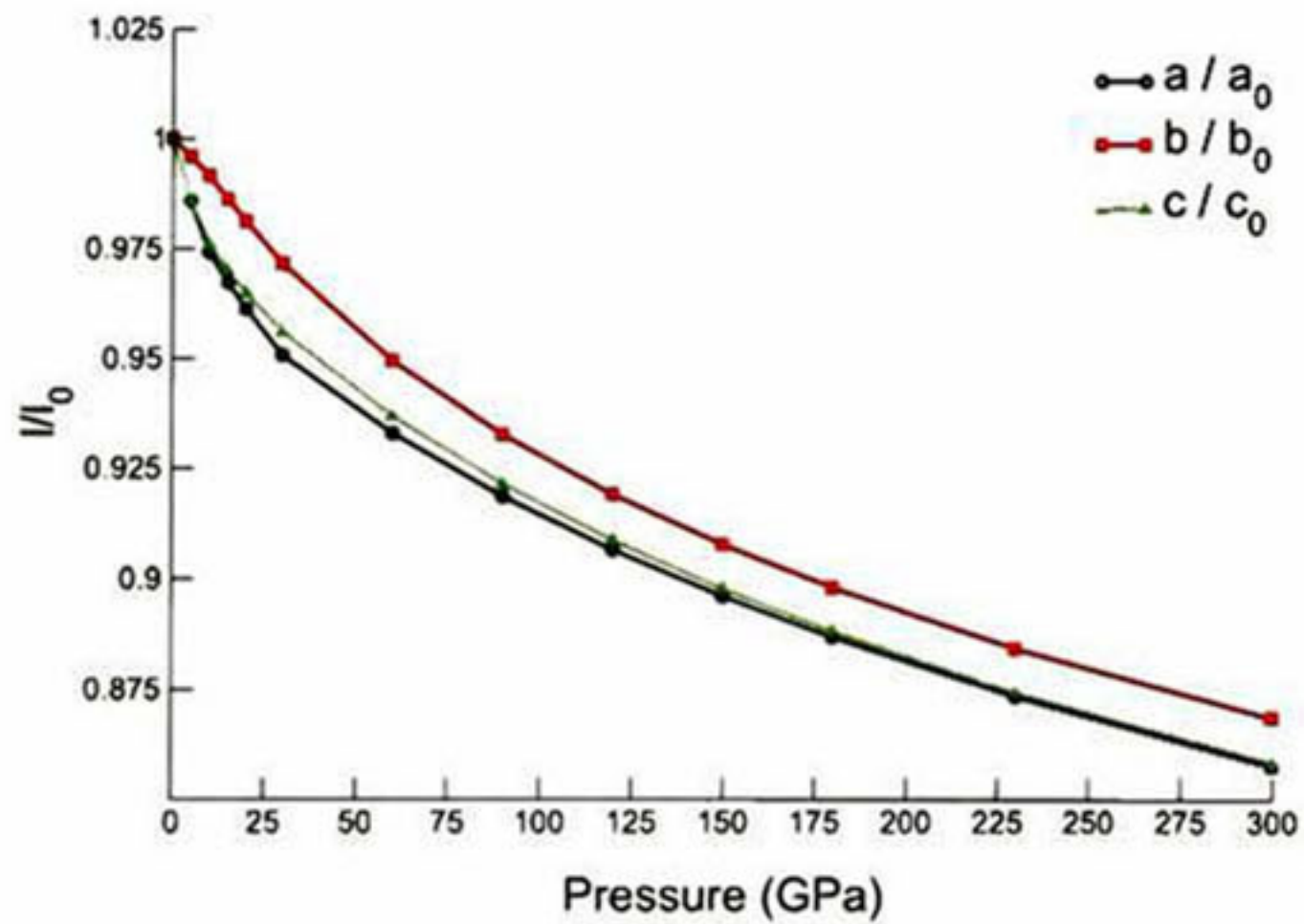


Figure 4.8: Compressibility for ferromagnetic (FM) calculation.

Also interesting, is that the discontinuity in the relative axial compressibility is reflected in the angle compressibility as well. In figures 4.9 and 4.11 one can recognize an abrupt change in the slope of the compressibility of angles $C_2 - Fe_{g2} - Fe_{g6}$ and $Fe_{g1} - C_2 - Fe_{g2}$ at low pressures, while the compressibility curves of all the other angles are quite smooth. For both calculations, at the beginning the slope is very sharp and suddenly (around 30 GPa) the slope

becomes less pronounced. Note that these bonds involve C and Fe atoms. This makes sense because as mentioned before, at the ground state, the existence of a $p-d$ hybrid band formed by the transferred $2p$ electrons of carbon atoms to the d electrons of iron atoms reflected on its density of states, is the main reason for the relative weakening of the Fe moment in cementite as compared to pure $bcc Fe$ [50]. Therefore the loss of magnetization induced by pressure, is related as well to the bonding interactions between Fe and C atoms.

The magnetism in Fe_3C is a result of the contributions of local magnetic moments of iron atoms in general Fe_g and special positions Fe_s . At the ground state (see section 3.3.2), the magnetic moment of Fe_g atoms is larger than that of Fe_s atoms. Here, it hasn't been measured the magnetic moment evolution of Fe_g and Fe_s atoms as a function of pressure. Nevertheless according to figures 4.10 and 4.12 the same characteristics responsible for the difference in the magnetic moment of iron atoms at different sites, still holds at large pressures. That is to say, stronger interactions between Fe_g and its iron environment due to shorter $Fe_g - Fe$ distances and the bonding interactions between Fe and C atoms ($d(Fe_g - C) > d(Fe_s - C)$). Therefore, it is possible that one of the ingredients for the loss of magnetization, is the reduction of local magnetic moment of Fe_g atoms enhanced by pressure.

4.3.4 Equation of state

There are two main considerations that were taken into account to adjust the data of the calculations to an equation of state, and to the interpretation of the results obtained. Firstly, to select an *EOS* proper to adjust high pressure volume-energy data, which means to choose an *EOS* that takes into account the fact that at high pressures it is more difficult to compress the solid. And secondly, the magnetic state of the calculations.

Here, all calculations have been adjusted to the so called third order *Birch-Murnaghan EOS* which is one of the most commonly used *EOS* to fit high pressure volume-energy data. Nevertheless, in this special case one must be careful, since we are dealing with a second order magnetic transition and therefore, there is a different trend of the $V - P$ data before and after the transition.

To illustrate the effect of magnetization on the equation of state, in fig 4.2 are shown the equation of state parameters obtained for each of the FMM configurations. As can be seen, the ground state volume V_0 increases directly with the value of the magnetization while the bulk modulus K_0 decreases. This is because magnetism produces an interatomic repulsion that increases the atomic volume and softens the structure giving rise to a corresponding decrease in the bulk modulus.

Due to the presence of a high pressure phase transition, the behavior of the material can not be represented by a solely *EOS* such as the third order *Birch-Murnaghan EOS*. One option is to merely fit the corresponding $P-V$ data to differently parametrized *EOS* for each phase. Actually a second-order magnetic phase transition requires that there is a discontinuity in the second derivative of the *Gibbs* free energy. At constant temperature, $\frac{\partial^2 G}{\partial P^2} = \frac{\partial V}{\partial P}$; however, a dis-

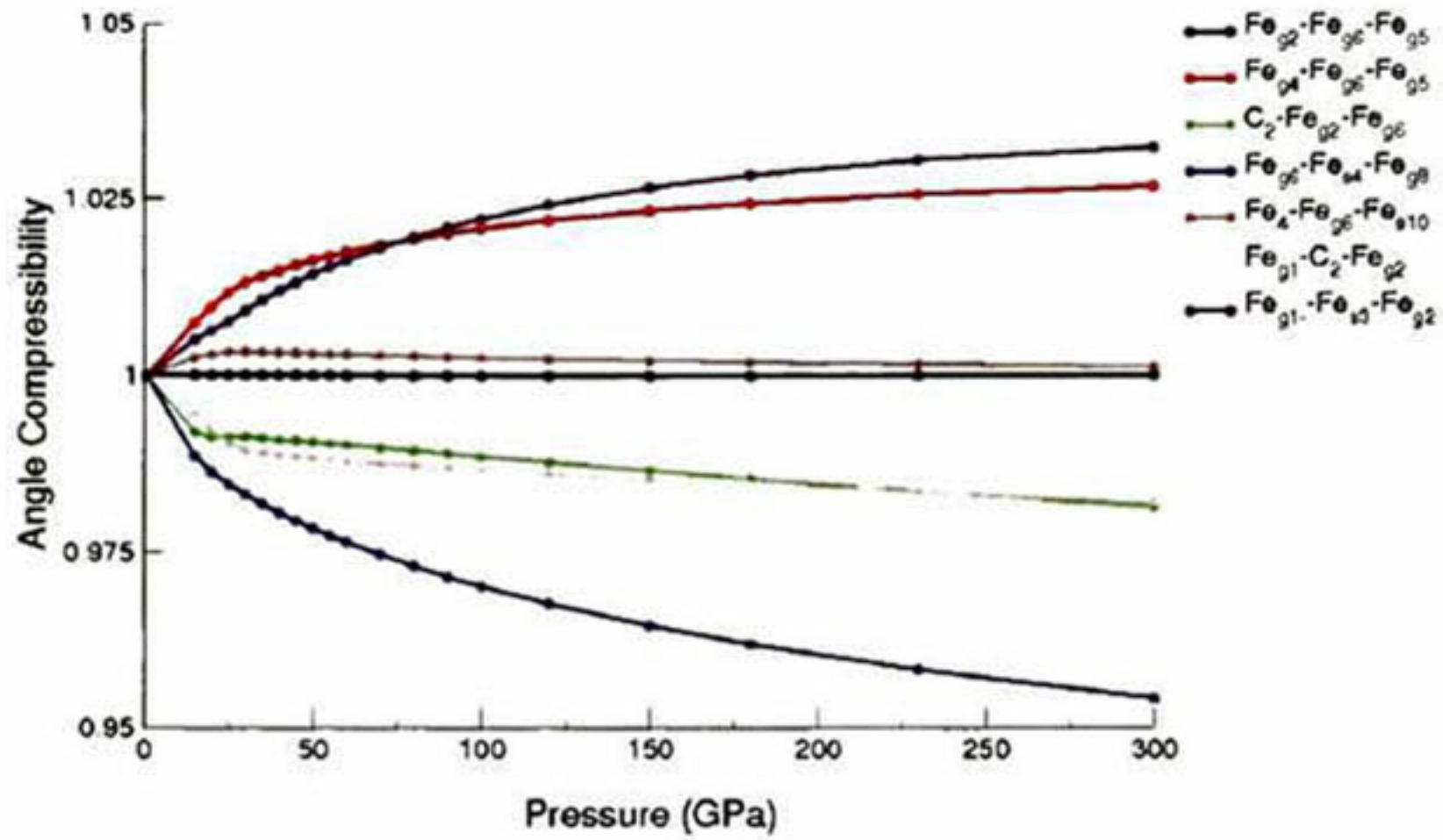


Figure 4.9: Angle compressibility as a function of pressure, FM calculation.

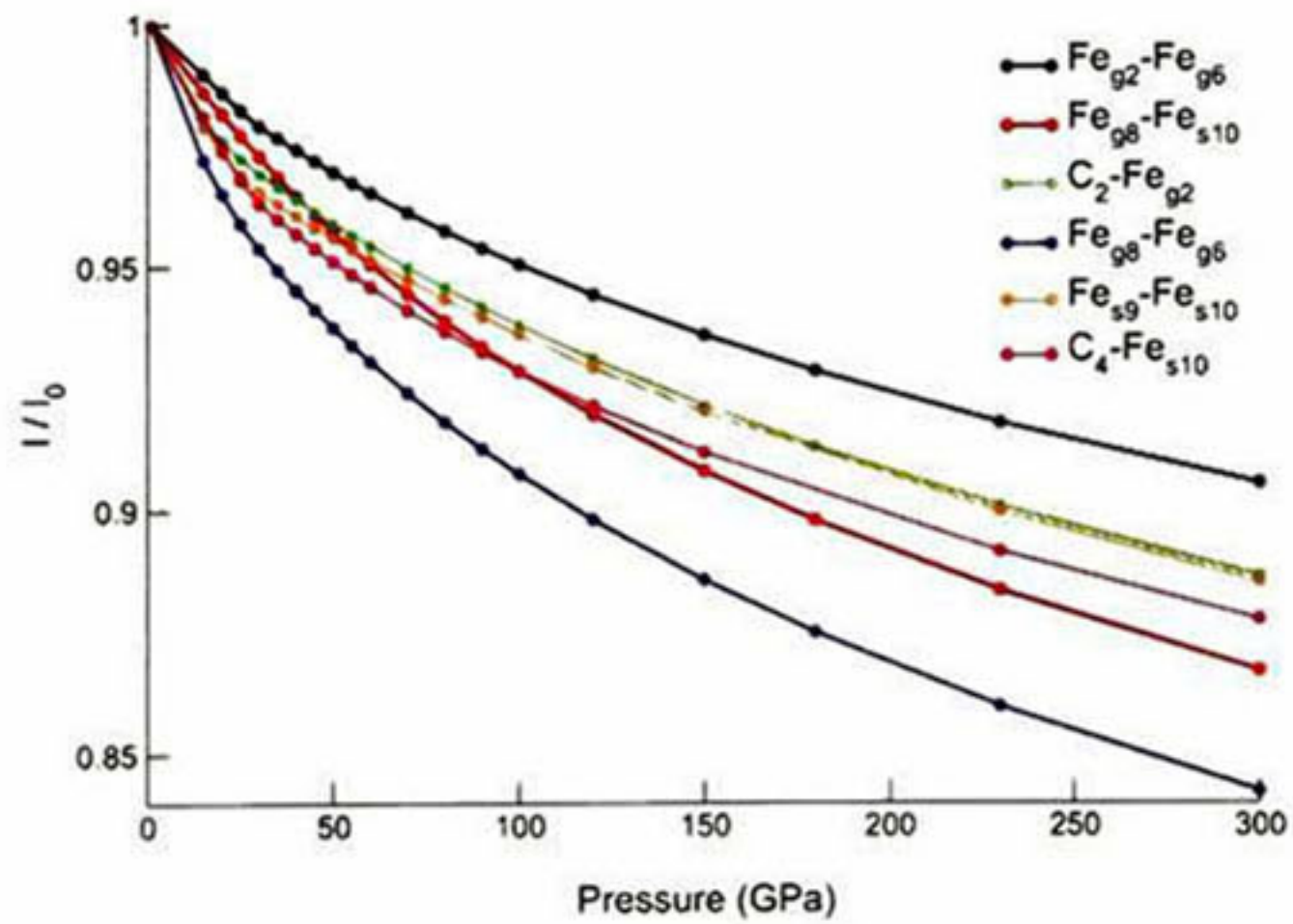


Figure 4.10: Bond length compressibility as a function of pressure, FM calculation.

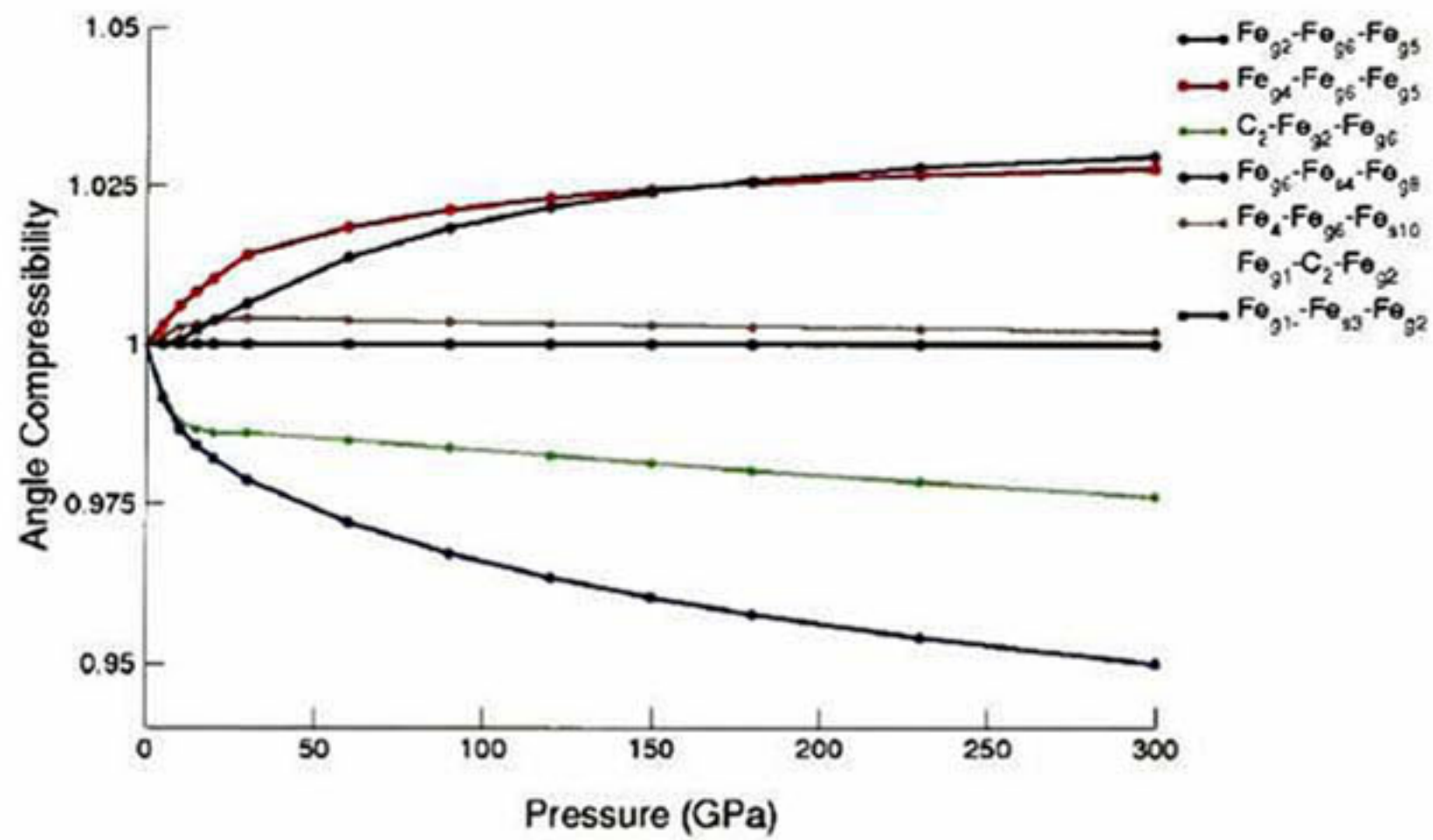


Figure 4.11: Angle compressibility as a function of pressure, FMM calculation.

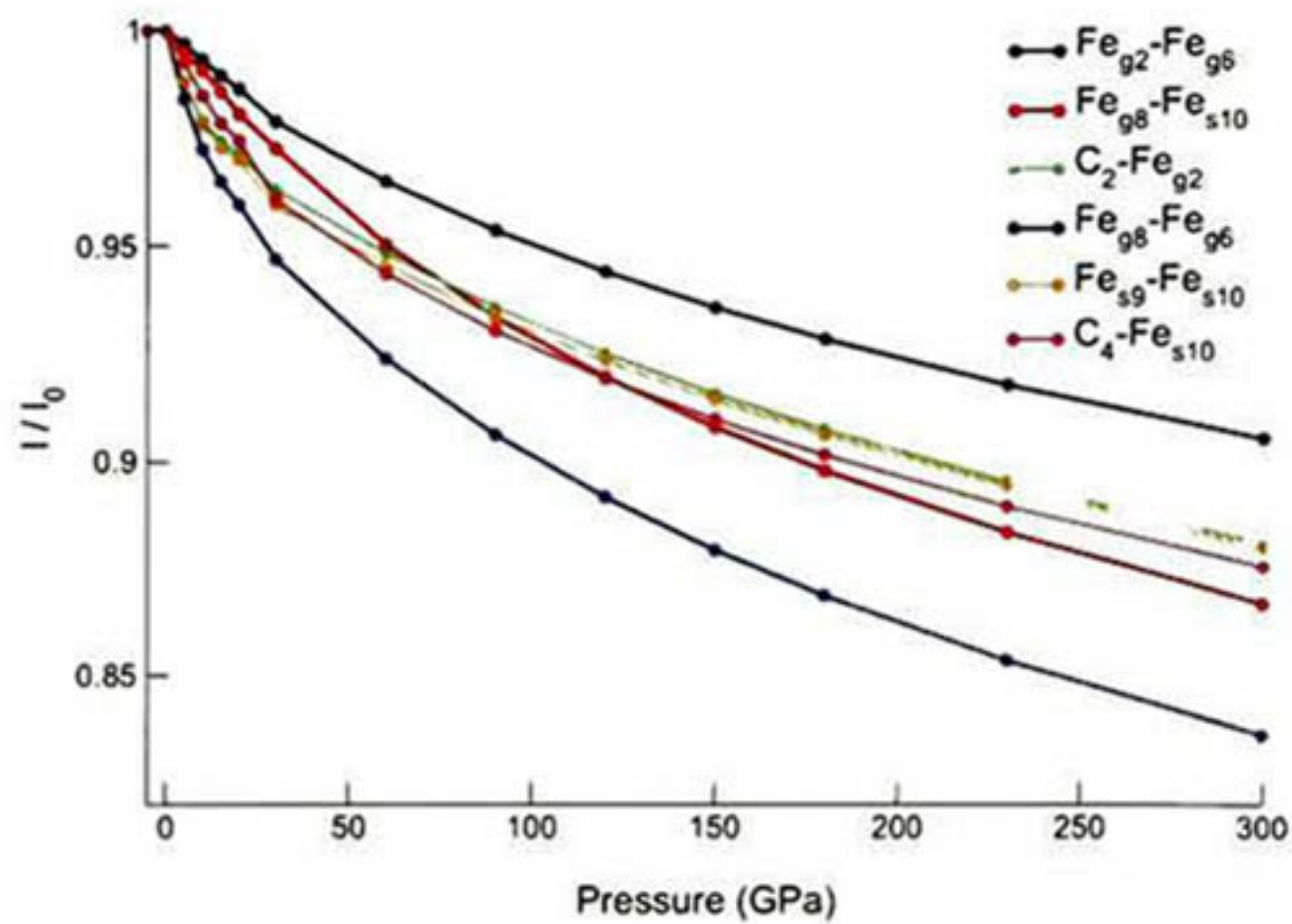


Figure 4.12: Bond length compressibility as a function of pressure, FMM calculation.

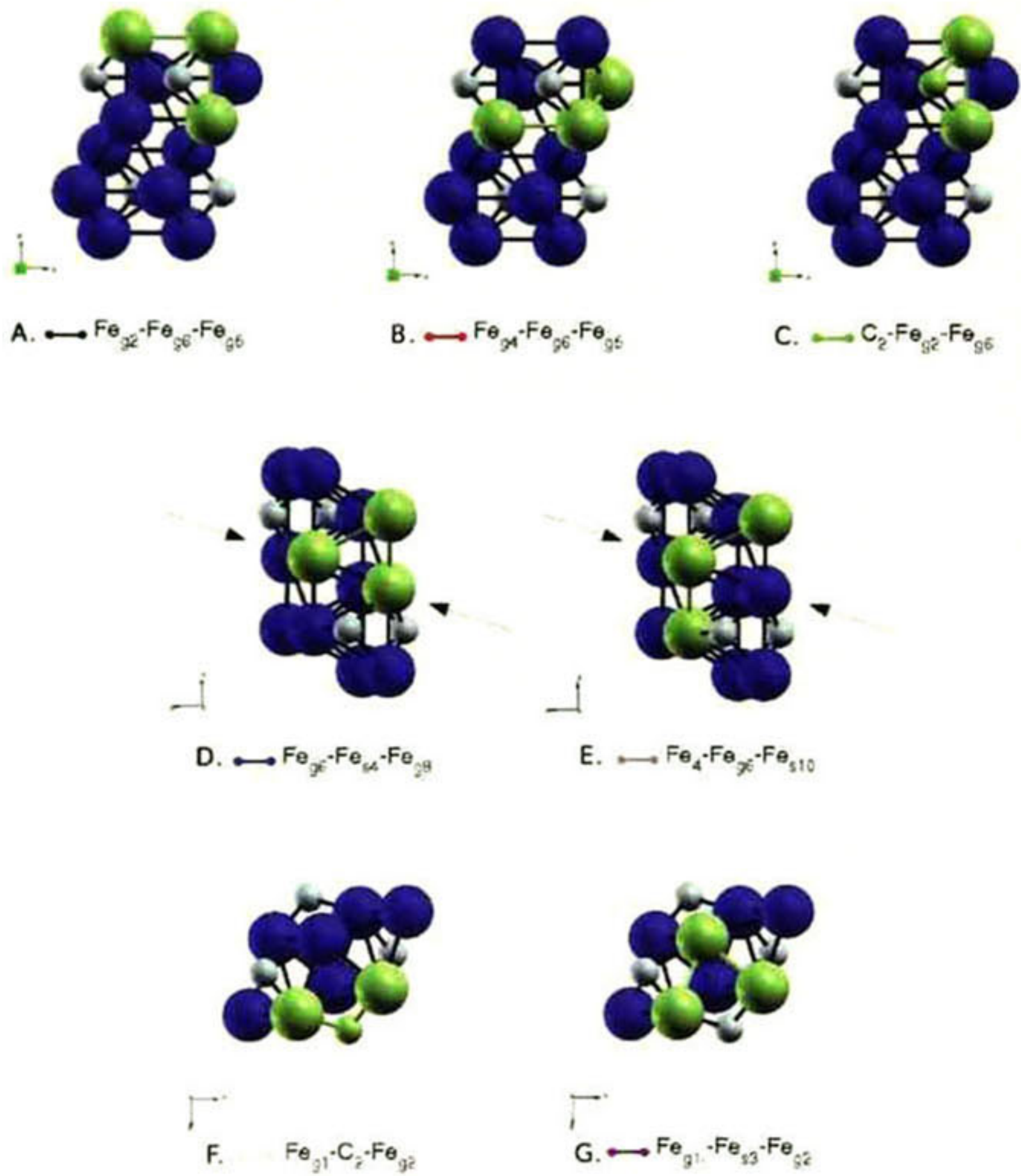


Figure 4.13: Unit cell of cementite, showing the angles considered in figures 4.9 and 4.11.

Table 4.2: Equation of state parameters for FMM calculations. The data was fitted to a third order *Birch-Murnaghan* equation of state between 0 and 30GPa.

Configuration	V_0 (\AA^3)	K_0 (G Pa)	K'_0 (Ha/ua ⁴)
$\mu_0 = 0\mu_B$	144.38	292.68	4.53
$\mu_0 = 4\mu_B$	144.46	329.3	1.69
$\mu_0 = 8\mu_B$	145.54	269.12	5.68
$\mu_0 = 10\mu_B$	145.88	276.5	5.18
$\mu_0 = 12\mu_B$	146.43	274.47	5.32
$\mu_0 = 16\mu_B$	147.99	276.03	4.62
$\mu_0 = 20\mu_B$	150.29	264.64	4.77
$\mu_0 = 24\mu_B$	153.4	254.63	4.54
$\mu_0 = 36\mu_B$	170.52	195.12	4.86
$\mu_0 = 48\mu_B$	201.85	119.42	5.99

continuity in $\frac{\partial V}{\partial P}$ is incompatible with the third order *Birch-Murnaghan* EOS, in which $\frac{\partial V}{\partial P}$ is a continuous function [7].

A consequence of this, is that the EOS turn out to be pressure dependent. To demonstrated this, in table 4.3 are compared the EOS parameters acquired by fitting our results to the third order *Birch-Murnaghan* EOS using different pressure ranges.

The $P - V$ data has to different trends before and after the transition. This is reflected in the large difference of EOS parameters for different pressure regimes. The responsible, is the magnetic state of the material. In the low pressure regime, the material is magnetic, therefore the EOS predicts a large V_0 which in turn produces large values of K_0 . But for the same calculations in the high pressure regime, the material is in a not magnetic state hence, V_0 is lower and K_0 increases considerably. Note that K_0 is extremely high, if we take into account that the bulk moduli of iron is about 165GPa and for diamond, one of the most incompressible substances is 442GPa.

In table 4.3 are reported as well, the results from fit the data to a solely EOS. As can be observed, the value of K_0 is more reasonable. However, it has been mentioned that because of the presence of a high pressure magnetic phase transition, this is not a valid procedure. In fact, the only way to overcome this difficulty, it would be to fit the data to an EOS that consider analytically the effect of the magnetization. At the moment, there is no such EOS and deeper research is desirable in this field. A lot of progress could be made in the study of matter at high pressure conditions, where is commonly to encounter this kind of phenomena.

Table 4.3: Equation of state parameters. The data was fitted to a third order *Birch-Murnhagan EOS*

	V_0 (Å^3)	K_0 (G Pa)	K'_0 (Ha/ua^4)
$0 \leq P_T(\text{GPa}) \leq 30$			
FM	149.23	160.57	8.11
FMM	149.02	167.86	7.42
NM	144.38	291.54	4.75
$30 \leq P_T(\text{GPa}) \leq 360$			
FM	144.07	304.133	4.35
FMM	143.97	306.91	4.32
NM	143.92	308.11	4.31
$0 \leq P_T(\text{GPa}) \leq 360$			
FM	146.30	256.36	4.88
FMM	146.52	254.66	4.84
NM	144.19	302.41	4.35

In table 4.4 are displayed the *EOS* parameters of some recent experimental and theoretical studies. Some of this results suffer of the same problems we found when calculating the *EOS* parameters. For instance the first two experimental results ([5], [4]), where fitted to a unique *EOS*. Following the same procedure (third set of table 4.3), we obtained values of K_0 that are as much as 47% higher. This huge discrepancy is due to the fact that in these experiments the compression reached at the best 73GPa [5], while in the present study a compression of 300GPa was achieved. Thus, the experimental K_0 resemble more the behavior of the material on its low-pressure non-magnetized state. One proof of this is that the K_0 extracted for FM and FMM calculations, is higher only about 8.5% for FM and 4.3% for FMM, when the data was fitted to the low pressure regime (first set of table 4.3).

On the other hand, our results are in better agreement with *Lin et. al* [57] and *Vocadlo et. al* [7], since they calculated the *EOS* parameters by fitting the corresponding $P - V$ data to differently parametrized *EOS* for each phase. In particular the calculated value of K_0 is closer than the obtained by *Vocadlo et. al* to the experimental results of *Lin et. al*. For instance, in the low-pressure magnetized regime (first set of table 4.3), the computed K_0 is 10.5% lower for FM and 6.4% for FMM, whereas *Vocadlo et. al* show a disagreement of 27.4%. In the high-pressure non magnetized regime (second set of table 4.3) the agreement is improved since the calculated K_0 are off by about 5.6% for FM, 6.6% for FMM and 7% for NM, whereas for *Vocadlo et. al* the error reaches 10%.

A consequence of the high K_0 obtained by *Vocadlo et. al*, is their prediction of a extremely high transition pressure ($P_T = 60\text{GPa}$). Indeed, if the bulk

Table 4.4: References for equation of state parameters of Fe_3C , showing ground state volumen V_0 , bulk modulus K_0 and its first derivative with respect to pressure K'_0 .

	V_0 (\AA^3)	K_0 (GPa)	K'_0 (Ha/ua^4)
Experimental ^a			
[5] Scott et al.	155.26 ± 14^c	175.4 ± 3.5	5.1 ± 0.3
[4] Li et al.	155.2	174.0 ± 6	4.8 ± 0.8
[57] Lin et al	148.0	179.4 ± 7.8^d	4.8 ± 1.6^d
	–	288.0 ± 42^e	4^e
Theoretical ^b			
[3] Wood et al.	154.88	174.0	5.1
[7] Vocadlo et al.	153.04^f	228.55^f	5.36^f
	143.36^g	316.62^g	4.3^g
[50] Khmelevsty	150.0^h	203^h	–

All data were fitted to a third order Birch-Murnaghan EoS with exception of [3] which are thermodynamic estimates, and [50] obtained from a third order fit, but the type is not specified.

^a Values at 300K.

^b Values at 0K except for refence [3] which were calculated at 300K.

^c Not extracted from the fitting.

^d Ferromagnetic state.

^e Non-magnetic state, with fixed $K' = 4$

^f Spin polarized calculation.

^g Non-spin polarized calculation.

^h Ferromagnetic calculation.

moduli is high, then the material is less compressible, and a higher pressure is needed to induce the transition. This is why the predicted $P_T = 30GPa$ is closer to the experimental results of *Lin et. al* ($P_T = 25GPa$).

To conclude this section it can be stated that the *EOS* parameters depend notably on the state of magnetization and the pressure (or volume) range over which the fit is performed. Therefore, one has to be careful, when making predictions about the physical properties of Fe_3C under high pressure conditions.

Part V

Chapter 5

Elastic Properties

5.1 Introduction

For elastic properties, one should understand the ability of a material to return to its original condition after stress is applied. This is exactly the information that can be obtained from a seismic measurement. For instance, when a stress is suddenly released, such as in an earthquake, the change in strain of the earth's forming material propagates as an elastic seismic wave. Seismic measurements of the travel and arrival times of these waves, allows to construct models in order to constrain the composition, structure and elastic properties of the earth's interior. Therefore, to have some knowledge of elastic properties of the materials that presumably form the earth's interior is extremely important. This chapter is devoted to the study of the elastic properties of Fe_3C , and to the comparison of the results with the Preliminary Reference Earth Model (*PREM*).

5.1.1 Stress-strain relations

The response of an isotropic, homogeneous solid to the application of stress or strain, is given by the so-called generalized Hooke's law [9],

$$\sigma_{ij} = c_{ijkl}\varepsilon_{kl}. \quad (5.1)$$

Equation 5.1 relates the second order tensor of stress σ_{ij} and strain ε_{kl} , through the fourth rank elastic constant tensor c_{ijkl} . This equation defines nine equations with nine terms each, giving it a total of 81 components. However, σ_{ij} and ε_{kl} are symmetric reducing it to only 36 components. Also, in the linear elastic regime where Hooke's law applies and under isothermal conditions, the free energy is dependent only on the state of the body. This makes the c_{ijkl} tensor symmetric and thereby further reduces the 36 components to 21 independent ones. Symmetry constraints imposed in crystal systems above triclinic reduce the number of independent components even more, down to only three in the cubic system [60]. Fe_3C has an orthorhombic crystal structure, for this symmetry the number of independent components reduces to nine and equation 5.1 in *Voigt's* notation looks like:

$$\begin{pmatrix} \sigma_{11} \\ \sigma_{22} \\ \sigma_{33} \\ \sigma_{23} \\ \sigma_{13} \\ \sigma_{12} \end{pmatrix} = \begin{pmatrix} c_{11} & c_{12} & c_{13} & 0 & 0 & 0 \\ c_{12} & c_{22} & c_{23} & 0 & 0 & 0 \\ c_{13} & c_{23} & c_{33} & 0 & 0 & 0 \\ 0 & 0 & 0 & c_{44} & 0 & 0 \\ 0 & 0 & 0 & 0 & c_{55} & 0 \\ 0 & 0 & 0 & 0 & 0 & c_{66} \end{pmatrix} \begin{pmatrix} \epsilon_{11} \\ \epsilon_{22} \\ \epsilon_{33} \\ \epsilon_{23} \\ \epsilon_{13} \\ \epsilon_{12} \end{pmatrix}$$

The mechanical stability of a crystal implies that its strain energy must be positive against any homogeneous elastic deformation [13]. For an orthorhombic crystal as Fe_3C , this condition is given by the following constrains:

$$C_{11} + C_{22} + C_{33} + 2C_{12} + 2C_{23} + 2C_{13} > 0 \quad C_{ii} > 0 \quad (\text{for } i = 1, 6).$$

$$C_{11} + C_{22} > 2C_{12}, \quad \text{and} \quad C_{22} + C_{33} > 2C_{23}. \quad (5.2)$$

5.1.2 The Voigt-Reuss scheme

The elastic properties of a crystal, can be computed straightforward from the single-crystal elastic constants c_{ij} . Nevertheless, in general, the elastic moduli of a single crystal will give an anisotropic elastic moduli tensor reflecting the symmetry of the crystal lattice. Instead, one aims to calculate properties of a polycrystalline aggregate and not single-crystal properties, if a comparison with seismological models wants to be done.

For this reason, an arithmetic average can be performed taking as extremes two bounds, namely a lower bound calculated assuming that the stress is uniform in the aggregate and that the strain is the total sum of all the strains of the individual grains in series (*Reuss* bound), and an upper bound calculated assuming that the strain is uniform and that the stress is supported by the individual grains in parallel (*Voigt* bound). The arithmetic average of the two bounds is called the *Voigt - Reuss* scheme.

Once the single-crystal elastic constants c_{ij} are obtained, the elastic properties for both bounds can be derived from the next set of equations. Where G_R and K_R stands for the *Reuss's* shear and bulk modulus respectively, and G_V , K_V for the *Voigt's* shear and bulk modulus respectively.

$$G_R = \frac{15}{4(s_{11} + s_{22} + s_{33}) - 4(s_{12} + s_{13} + s_{23}) + 3(s_{44} + s_{55} + s_{66})} \quad (5.3)$$

$$G_V = \frac{1}{15}(c_{11} + c_{22} + c_{33} - c_{12} - c_{13} - c_{23}) + \frac{1}{5}(c_{44} + c_{55} + c_{66}) \quad (5.4)$$

$$K_R = \frac{1}{(s_{11} + s_{22} + s_{33}) + 2(s_{12} + s_{13} + s_{23})} \quad (5.5)$$

$$K_V = \frac{1}{9}(c_{11} + c_{22} + c_{33}) + \frac{2}{9}(c_{12} + c_{13} + c_{23}). \quad (5.6)$$

In this equations, s_{ij} are the components of the compliance tensor, related to the elastic constant matrix by $S = C^{-1}$

With these elements, the *Vogit – Reuss* scheme can be applied (equations 5.1.2 and 5.1.2), and then the whole elastic modulus tensor for an isotropic material can be determined. This last, has only two independent variables, which can be the shear G and bulk modulus K , therefore, the *Young's* modulus E and the *Poisson's* ratio ν can be derived, using equations 5.1.2 and 5.1.2.

$$G = \frac{1}{2}(G_R + G_V) \quad (5.7)$$

$$K = \frac{1}{2}(K_R + K_V) \quad (5.8)$$

$$E = \frac{9KG}{3K + G} \quad (5.9)$$

$$\nu = \frac{3K - 2G}{2(3K + G)} \quad (5.10)$$

5.1.3 Seismic waves and density

As a result of an earthquake, explosion or impact, the change in strain of the earth's forming material propagates as an elastic seismic wave. There are three types of seismic waves, surface waves, *P – waves* and *S – waves*. The last two are body waves, since they propagates through the earth's interior.

P-waves

P – waves are longitudinal or compressional waves and can travel through any type of material. This ability allows the waves to travel through the earth's core and outer crust.

S-waves

S – waves are transverse or shear waves and can travel only through solids, since fluids do not support shear stresses. This phenomenon was original evidence for the now well-established observation that the earth has a liquid outer core, as demonstrated by Richard Dixon Oldham [9]. In general, their speed is about 60% of that of *P* waves.

Body waves propagation velocity depends on several factors such as the density and elasticity of the medium. In turn, density and elasticity, vary according to temperature, composition, phase and pressure from depth. The velocity in the medium is inversely dependent on the density of the medium. Therefore the velocity and the attenuation of the wave are used to determine the density. Changing density causes seismic energy to reflect and change direction incrementally or abruptly. Mapping the travel times of P – waves allows inferences on the density and composition of layers in the earth. Mapping of P and S wave arrival times show significant circular regions where P and/or S waves do not arrive allowing inference on size, structure and composition of earth's core.

The speed of P – waves is given by the next expression:

$$v_P = \sqrt{\frac{K + \frac{4}{3}G}{\rho}}, \quad (5.11)$$

where K is the bulk modulus, G is the shear modulus and ρ is the density of the material through which propagates. Similarly, the S – wave propagation speed is given by:

$$v_S = \sqrt{\frac{G}{\rho}}. \quad (5.12)$$

It is known that density and seismic wave velocities in the earth's interior, increase with depth (and therefore with pressure). Looking at both expression one might expect that both S and P wave speeds to decrease in the earth's interior. However, the opposite happens (figure 1.2). The reason is that the elastic modulus increases more rapidly. This is an example of how important is to study the pressure effect on the elastic properties of Fe_3C

5.2 Methodology

The elastic constants tensor was determined for a set of pressures that goes from the mantle-core boundary to the earth's inner core pressure conditions. Consequently, as a first step the equilibrium structure of the NM unit cell configuration was determined for 100, 150, 230, 300, 330 and 360 GPa. Secondly, for each structure at a given pressure, small positive and negative strains of an amplitude of 1% were applied. For an orthorhombic crystal only six distortion matrices are needed to compute all nine elastic constants. Then, to obtain the stress tensor, the atomic positions are re-optimized in the strained configuration. And finally the elastic constants are calculated from strain-stress relations by solving equation 5.1.

5.3 Results

5.3.1 Ground state elastic properties

Single crystal elastic constants

The elastic constant tensor at the ground state was determined for the FM calculation and FMM with $\mu_0 = 16$ and $\mu_0 = 20$ Bohr's magneton since these are the calculations that resemble better the magnetic state of cementite at the ground state. The results are displayed in table 5.1, together with some theoretical ([13], [61]) references. Just as in the present study, in both references, ab initio calculations were performed under the projected augmented wave method (PAW) and the generalized gradient approximation (GGA).

In general for C_{11} , C_{22} , C_{12} , C_{23} , C_{55} and C_{66} elastic constants the agreement between the obtained results and both references is at the most 15%. But can be bigger for the rest of elastic constants. In special for the FM calculation, C_{44} is negative, which violates the elastic stability conditions for the orthorhombic symmetry (equation 5.2).

The results of reference [61], revealed an extreme elastic anisotropy with a very small C_{44} amounting to only about 1/10 of C_{55} and C_{66} . Additionally, by performing X-ray diffraction stress measurements, on the basis of analysis of the hkl-dependence of the stress-induced reflection shifts, experimental confirmation of the extreme elastic anisotropy of Fe_3C was provided in the same study. Similarly to reference [13], for FMM calculations with $\mu_0 = 16$ and $\mu_0 = 20$, C_{44} amounts about 1/15 of C_{55} , C_{66} . Moreover for FM calculation C_{44} even becomes negative, indicating an elastic instability, which could hint at a ferroelastic elastic phase transition or at melting [62], [63], [61]. However, no observations, hinting at an unusual effect due to a negative C_{44} of Fe_3C , have been reported in the literature [61]. As a remainder it should be mentioned that for this calculation the obtained ground state magnetic moment is 17 Bohr's magneton per unit cell. Nevertheless FMM with $\mu_0 = 16$ and $\mu_0 = 20$ are elastically stable, indicating that elastic stabilization can be induced by a small change of the magnetic state.

At the ground state FMM $\mu_0 = 16$ and $\mu_0 = 20$ are degenerate, have the lowest enthalpy (figure 4.2) and are elastically stable (table 5.1). FM calculation is very closed but higher in enthalpy, and is not elastically stable. Which means that the calculation is probably trapped in a local minimum. To determined the right magnetic character at the ground state is necessary to perform a more refined scanning of magnetization between $\mu_0 = 16$ and $\mu_0 = 20$ Bohr's magneton.

Since magnetization plays such an important role on the elastic properties, the differences between the obtained results and theoretical references must be attributed to it. For instance, magnetization tends to expand the structure. Besides, the magnetic moment of FMM $\mu_0 = 16$ and $\mu_0 = 20$ is smaller than the obtained by [13], and [61]. As a result the predicted ground state volume is smaller and this increases the bulk modulus. The shear modulus is a more complex quantity and is difficult to say in which way the magnetic state is affecting

this parameter. It is known that depends mostly on the C_{44} elastic constant and that is directly proportional to it. However, for all shown theoretical results (including this work) an unusual small value of C_{44} was obtained. Additionally the shear modulus is inversely proportional to the off-diagonal shear elastic constants. Hence the discrepancy arises mainly from the high values predicted for the off-diagonal shear elastic constants as compared to references [13] and [61]. In consequence, such a low value of G , is responsible for the low *Young's* modulus reported.

After 0GPa, the enthalpy difference evolution of the FM and FMM $\mu_0 = 16$, $\mu_0 = 20$ remains very closed along the compression and the differences in enthalpy are within the computational error (figure 4.2). The C_{ij} 's for these calculations were not measured after 0GPa, therefore there is no way to know if elastic stability was reached. However the stability of Fe_3C has been experimentally measured up to 73 GPa at room temperature [5] and between 220°K-3700°K and 25GPa-70GPa [12].

For cementite the full set of single-crystal elastic constants has not been reported experimentally. For the experimental polycrystalline elastic properties some data can be found in literature, and they are reported as well in table 5.1. Comparison between experimental and theoretical results must be done carefully, since many factors might affect the accuracy of both theoretical and experimental results. Experimental accuracy can be affected by microstructural defects and by alloy preparation. On the other hand, the calculation of elastic constants, involves second derivatives of the total energy with respect to lattice distortion (which implies a lowering of the crystal symmetry and that the strain energy is very small), the relative error will certainly be larger than that for isotropic properties such as equilibrium volume which needs only the first derivatives of the total energy. Therefore a highly precise approach is necessary for the calculation of the elastic constants [64].

Additionally, experiments are performed at room temperature while theoretical studies involve zero temperature measurements. Because of thermal expansion experimental results show a lower bulk modulus than theoretical studies, as can be corroborated in table 5.1.

5.3.2 High pressure elastic properties

Polycrystalline elastic constants

The elastic constants tensor was determined for the high-pressure non-magnetized phase of Fe_3C . Accordingly, calculations were carried out for the NM configuration. Figure 5.1 shows the calculated variation of C_{ij} with pressure together with the theoretical results for the elastic constants of the high pressure stable phase of iron (Fe *hcp*) taken from reference [66]. This last results have been included because a direct comparison between the high pressure elastic properties of Fe_3C and *hcp* iron, is desirable in order to investigate the possibility of carbon being one of the iron alloying elements in the earth's core (section 5.3.2 and 5.3.3). In that study the full-potential linearized-augmented plane-wave method *LAPW* and the generalized gradient approximations *GGA* to the

Table 5.1: Elastic constants and elastic moduli at 0GPa. The bulk K , shear G , and *Young's* moduli are in GPa, while *Poisson's* ratio ν is a dimensionless quantity.

Elastic constants	C_{11}	C_{22}	C_{33}	C_{12}	C_{13}	C_{23}	C_{44}	C_{55}	C_{66}
FM	414	380	422	189	188	158	-22	139	139
FMM $\mu_0 = 16$	469	326	401	124	213	166	21	136	145
FMM $\mu_0 = 20$	449	368	366	196	207	207	18	132	140
Ref. [13]	495	347	325	158	169	163	18	134	135
Ref. [61]	385	341	316	157	162	167	13	131	131
Elastic moduli	K	G	Y	ν					
FMM $\mu_0 = 16$	240	55	152	0.39					
FMM $\mu_0 = 20$	266	47	132	0.42					
Ref. [13]	227	75	203	0.35					
Ref. [61]	224	68	185	0.52					
Experimental	174[4]	74[65]							

exchange-correlation potential was employed.

At the moment we do not have knowledge, of first principle calculations made to determine the elastic properties of Fe_3C on such a high pressure regime. Additionally, experiments are very extremally difficult to perform, not only because high pressure experiments are difficult and expensive, but also from problems preparing a sample that is pure, void-free, homogeneous, texture-free, stoichiometric and sufficiently large [46]. Therefore there is no experimental data which to compare the present results. These calculations allow for the first time the comparison of the high-pressure elastic properties of Fe_3C with iron and *PREM* values.

According to the obtained results, under compression the elastic constants of Fe_3C obey all conditions in equation 5.2, indicating that cementite is an elastically stable structure at high pressures.

The compression is quite isotropic, this is reflected in the permanent increase for all the C_{ij} with pressure and the fact that non of the curves cross with each other. The same can be deduce from figures 4.5 and 4.6 of chapter 3, where the relative axial compressibility showed a nearly constant variation of the a/b , a/c and b/c ratios in the high pressure regime, for both FM and FMM calculations.

One can distinguish three groups among the C'_{ij} s. The first group is composed by the uniaxial constants C_{11} , C_{22} and C_{33} , and they present the largest values. Following them is the off-diagonal shear elastic onstants integrated by C_{12} , C_{13} , C_{23} and finally the diagonal shear elastic constants group (C_{44} , C_{55} and C_{66}) with the lowest values and also the smallest slope. Although this last, in average all constants duplicate its value from 100GPa to 360GPa, with some

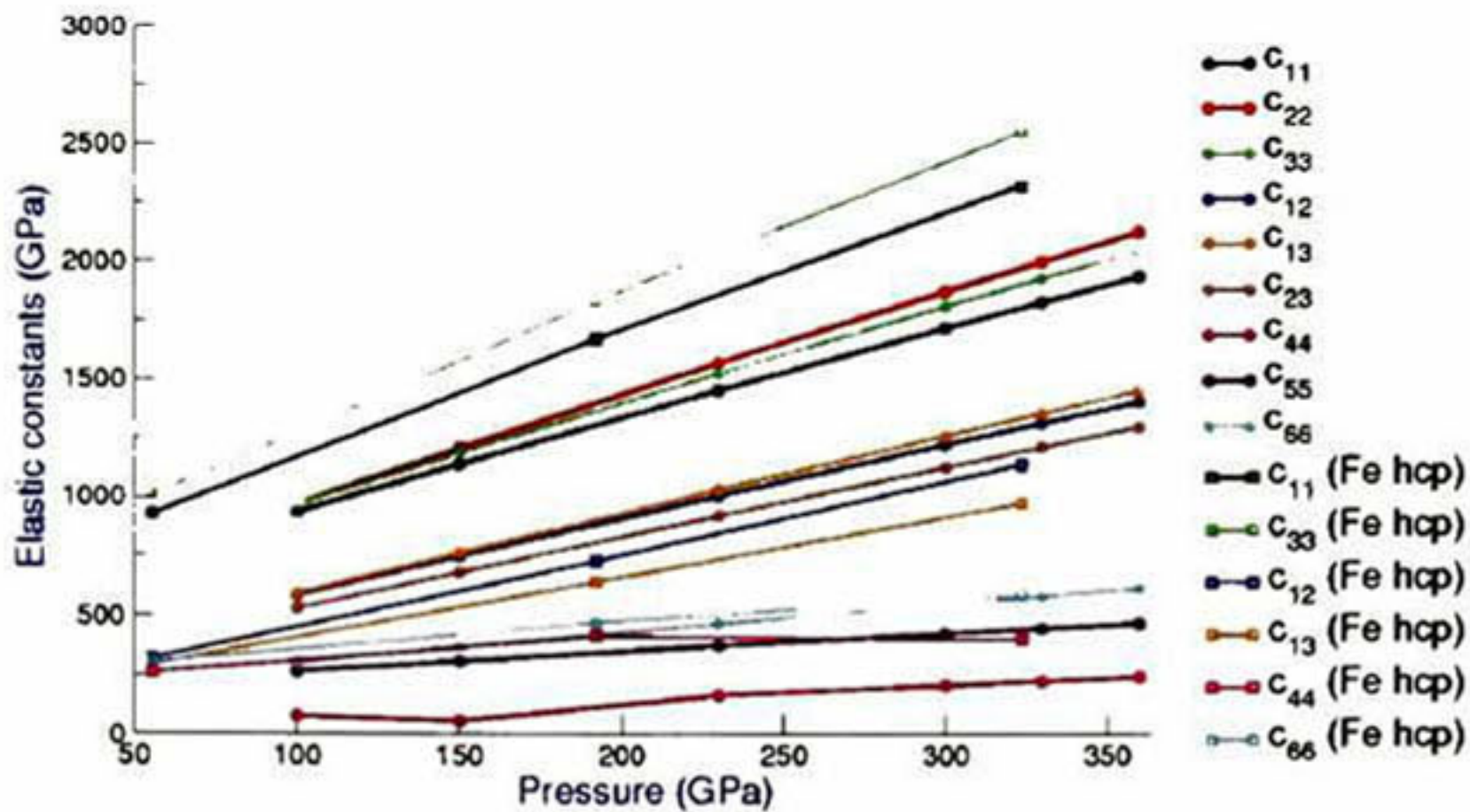


Figure 5.1: Elastic constants as a function of pressure, NS calculation. Also in the picture, are displayed theoretical results for the high pressure stable phase of iron [66].

marked exceptions, for instance C_{44} increases $\sim 200\%$ and C_{55} only $\sim 76\%$.

Among the uniaxial elastic constants, it can be noted that Fe_3C possess some elastical anisotropy. For instance C_{22} presents the highest value, followed by C_{33} and C_{11} . This indicates that the crystal is less compressible in the b axis followed by the c and a axis. The same compression mechanism was deduced by computing the axial compressibility in section 4.3.3 for FM and FMM calculations above 30GPa (see figures 4.5, 4.6, 4.7 and 4.8).

There are some similarities between cementite and $Fe\ hcp$ at high pressures. Both iron and cementite are non magnetic. Just as for cementite, the compression is quite isotropic. Therefore for $Fe\ hcp$ the elastic constants increase with pressure and non of the curves cross with each other. Nevertheless, with the exception of C_{12} , and C_{13} , all elastic constants of $Fe\ hcp$ are higher or equal (C_{66}) to those of Fe_3C . This could imply that the packing is denser in Fe than in cementite.

For hcp iron anisotropy is larger. For instance the difference between C_{11} and C_{33} in Fe is bigger than in Fe_3C . At 100GPa , the discrepancy between both uniaxial elastic constants is about 3.6% , in Fe_3C and 9.2% for $Fe\ hcp$. Similarly at 323GPa , the difference is about 5.7% in Fe_3C and 9.7% for $Fe\ hcp$. This means that at high pressures $Fe\ hcp$ is more anisotropic, but the degree of anisotropy increases more as a function of pressure for Fe_3C .

Although these observations, it is known that temperature greatly affects the elastic constants of $Fe\ hcp$. And it is possible that the same applies for cementite. Therefore a more accurate comparison of the elastic properties of these materials must include temperature effects.

Bulk and shear modulus

From the single crystal elastic constants, the polycrystalline bulk (K) and shear modulus (G) were determined and its evolution up to 360 GPa is shown in figure 5.2 along with the results for $Fe\ hcp$ [66] and $PREM$ values up to inner's core conditions.

Interestingly, despite the difference in the predicted single crystal elastic constants, different crystal structure, mass density and composition, the predicted evolution of Fe_3C bulk modulus differ little from that of hcp iron. By the contrary the shear modulus of Fe_3C is quite lower.

This implies two things. As observed before, the degree of anisotropy is higher for hcp iron, which yields a higher shear modulus. On the other side, one could guess that the presence of carbon in Fe_3C enhance covalency. Accordingly the shear modulus of Fe_3C should be higher than that of iron. However, this is not the case, not even at the ground state. Therefore, this probes that the bonding in cementite is dominated in a higher extent by ionic interactions than by covalency. For instance, in ionic compounds electrostatic interactions are omnidirectional yielding low bond bending force constants which result in low shear modulus [67]. At the ground state, it has been found that the chemical bonding in Fe_3C exhibits a complex mixture of metallic, covalent, and ionic characters [13].

When comparing with $PREM$'s elastic moduli, one must take into account a few aspects:

Due to stratification of the earth's interior and because it is been considering Fe_3C as a crystalline solid, it is more pertinent to compare results with $PREM$ values for the inner core region. The mantle (lower mantle 100-127 GPa in figure 5.2) is solid but composed mainly of silicates. The outer core is liquid (therefore G approaches zero) and the inner core is solid. Furthermore, the $PREM$ model state that the core's density (both liquid outer core and solid inner core) is lower than that of pure iron measured experimentally at high pressure and temperature conditions. This led to the conclusion that the earth's core must be composed of iron alloyed with some lower atomic weight elements (lower than iron) such as carbon.

By adding carbon, density decreases and one expects a decrease of the bulk modulus that would equal better $PREM$ values. However in the form of Fe_3C , adding carbon does not have a considerable effect on the bulk modulus over that of iron hcp . But it does help to match better the shear modulus with $PREM$ at the inner core. By extrapolating *teinle – Neumann et. al* [66] G results for hcp iron up to inner's core pressure, one can see that the agreement with $PREM$ is highly improved by Fe_3C . At the outer-inner core boundary ($P = 230\text{GPa}$) the percentage difference is 49% for Fe_3C whilst the shear modulus of hcp iron is 280% higher than $PREM$. This difference decrease a little bit at the earth's center, being 36.8% for Fe_3C and 263% for hcp iron.

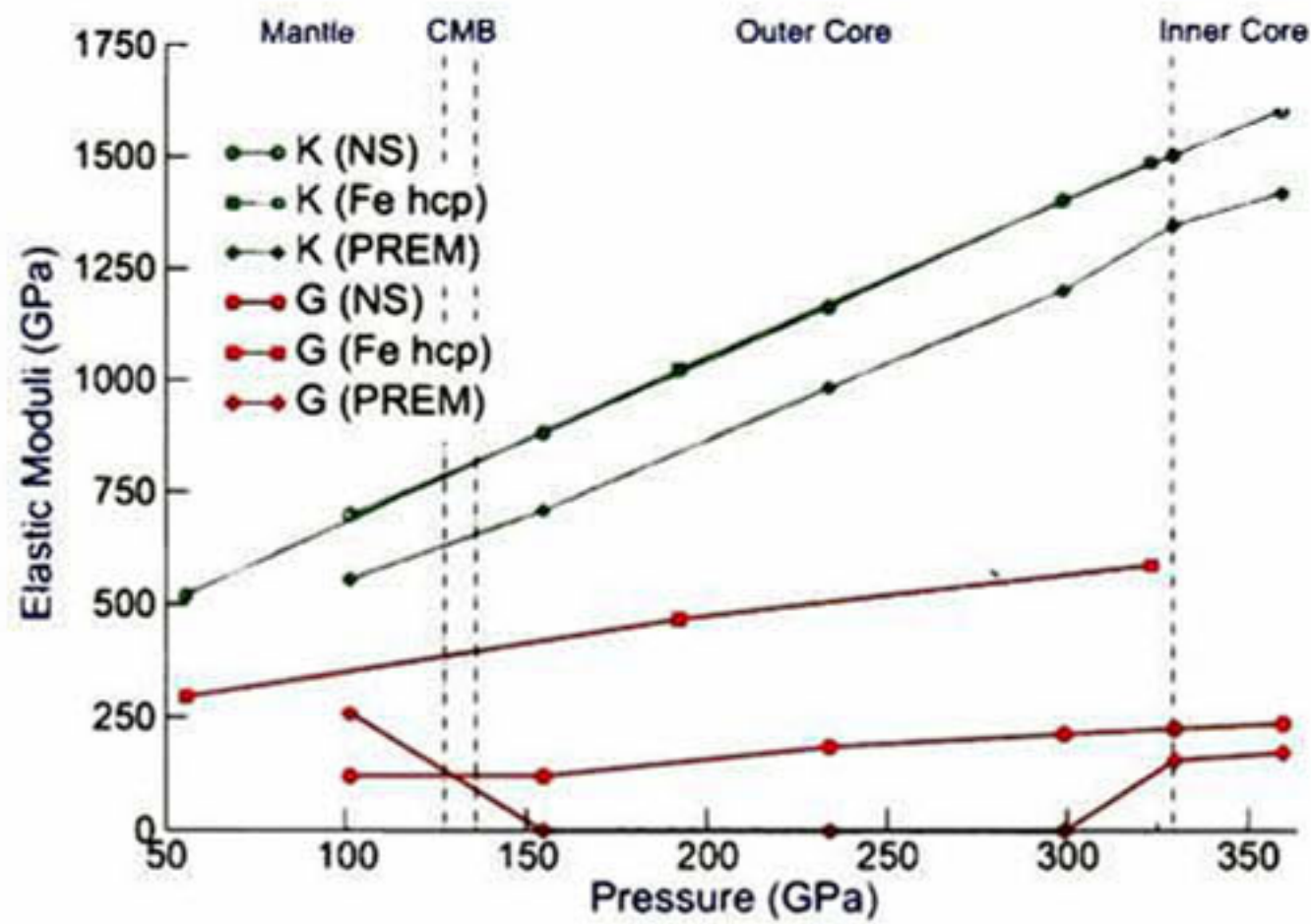


Figure 5.2: Bulk K and shear G modulus.

Poisson's ratio

Figure 5.3.2, shows the computed Poisson's ratio for Fe_3C along with iron hcp and PREM results. In general the Poisson's ratio for Fe_3C shows little pressure dependence with an average value of 0.43.

0.5 is the upper limit, infinite elastic anisotropy i.e. liquids Poisson's ratio is associated with the volume change during uniaxial deformation, 0.5 no volume change occurs during elastic deformation.

In average the observed value of the inner core is 0.44

At 300 K, the measured Poisson's ratios of iron, Fe-Ni alloys, FeHx, Fe₃S and Fe_{0.85}Si_{0.15} are smaller than 0.35 and show little pressure dependence [Mao et al., 2001; Lin et al., 2003, 2004b, 2005; Mao et al., 2004]. The Poisson's ratio of the non-magnetic Fe₃C at 300 K falls into a comparable range to other iron-rich alloys, but gradually increases from 0.30 at 6.6 GPa to 0.36 at 50 GPa, approaching the PREM value.

How is affected Poisson by temperature.

Note that the Poisson's ratio of the outer core is equal to 0.5 as expected for a liquid, but the Poisson's ratio of the inner core is also quite high (: 0.44). Various explanations have been given, including the possibility of liquid inclusions in the inner core. However, such conclusions are unnecessary, since a high Poisson's ratio does not necessarily imply the

important to realize that Poisson's ratio results from a complicated combination of elastic constants and can take widely different values depending on the material. A value of close to 0.5 does not mean that there is some proportion of liquid present: solid gold, for instance, at room temperature, has a Poisson's ratio of about 0.42. Poisson's ratio can be negative, if cracks

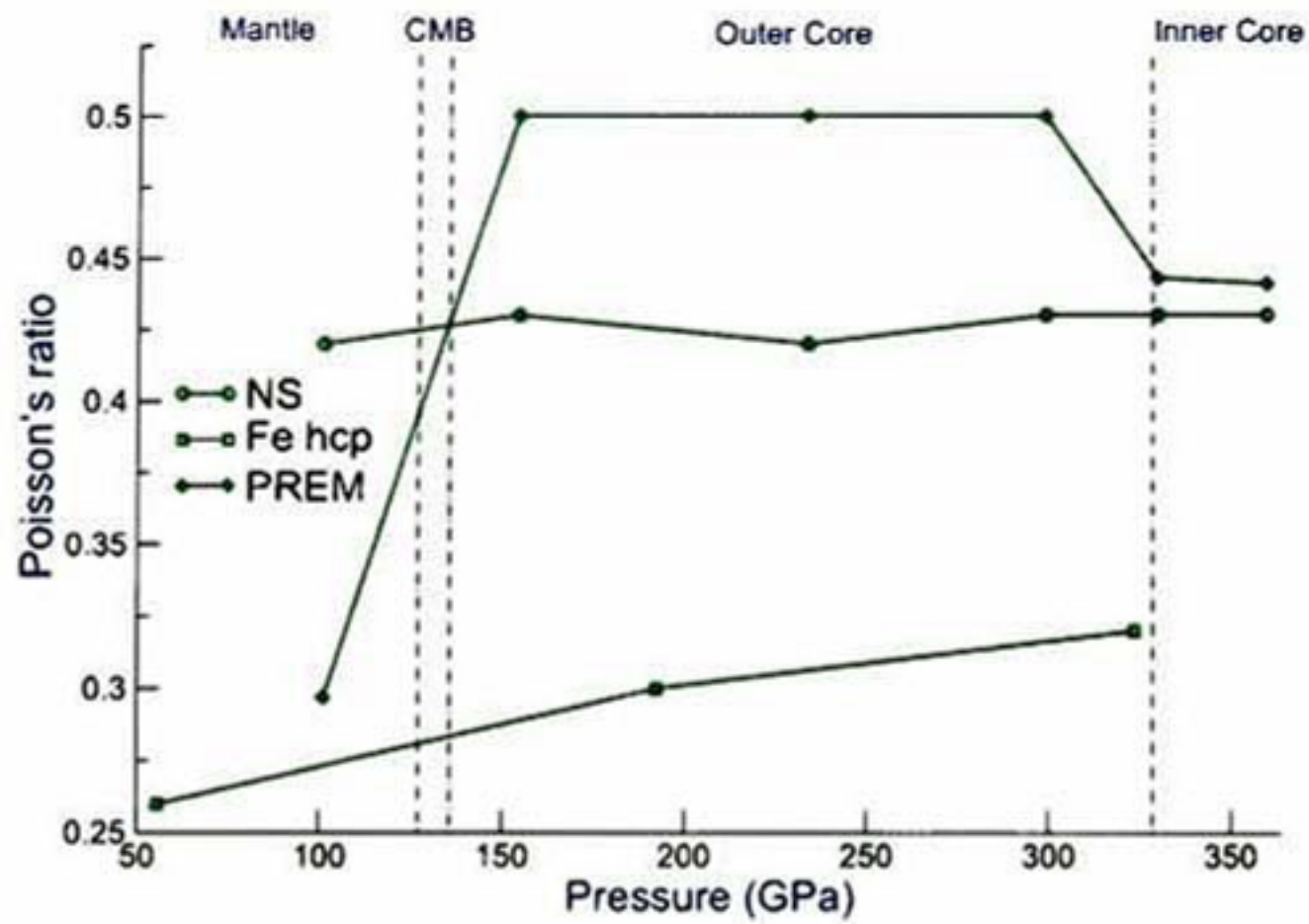


Figure 5.3: Poisson's ratio as a function of pressure

5.3.3 Sound Velocities and Density

Sound velocities

Figure 5.4 shows the computed sound wave velocities as a function of pressure along with *PREM* and *hcp* iron data [66]. As explained in chapter 1, it is now well established that the earth's core must consist mainly of iron. Differences in density and sound wave velocities between iron and the earth's core, indicate the presence of elements with lower atomic weight than iron. As can be observed, compared to *hcp* iron Fe_3C provides a better match of compressional (V_P) and shear (V_S) wave velocities to the seismically observed values of the earth's core, supporting carbon as a light element in the earth's core.

For instance, at 233 GPa in the middle of the outer core V_P of Fe_3C is about 7.8% smaller than that of *hcp* iron, while *PREM's* value is 14.7% lower than Fe_3C and 23% lower than *hcp* iron. Although, this region is in liquid state (V_S approach to zero) and both Fe_3C and *hcp* iron results correspond to a crystalline solid. In reality, V_P of Fe_3C and *hcp* iron in liquid state must be smaller and therefore closer to *PREM*.

For the same reason the agreement for both V_P and V_S at the solid inner core region is improved. At the outer-inner core boundary *PREM's* V_P are 7.8% smaller than Fe_3C and 13.7% smaller than iron *hcp*. Likewise *PREM's* V_S is 21.7% smaller than Fe_3C and 46.6% smaller than *hcp* iron. In contrast, up to 360 GPa the difference for V_P shows a narrow increment whilst for V_S diminish. *PREM's* V_P are 7.9% smaller than Fe_3C and 14.7% smaller than iron *hcp*. And *PREM's* V_S is 15.3% smaller than Fe_3C and 45.3% smaller than *hcp* iron at 360 GPa.

Here it has been shown that Fe_3C is elastically anisotropic at ambient con-

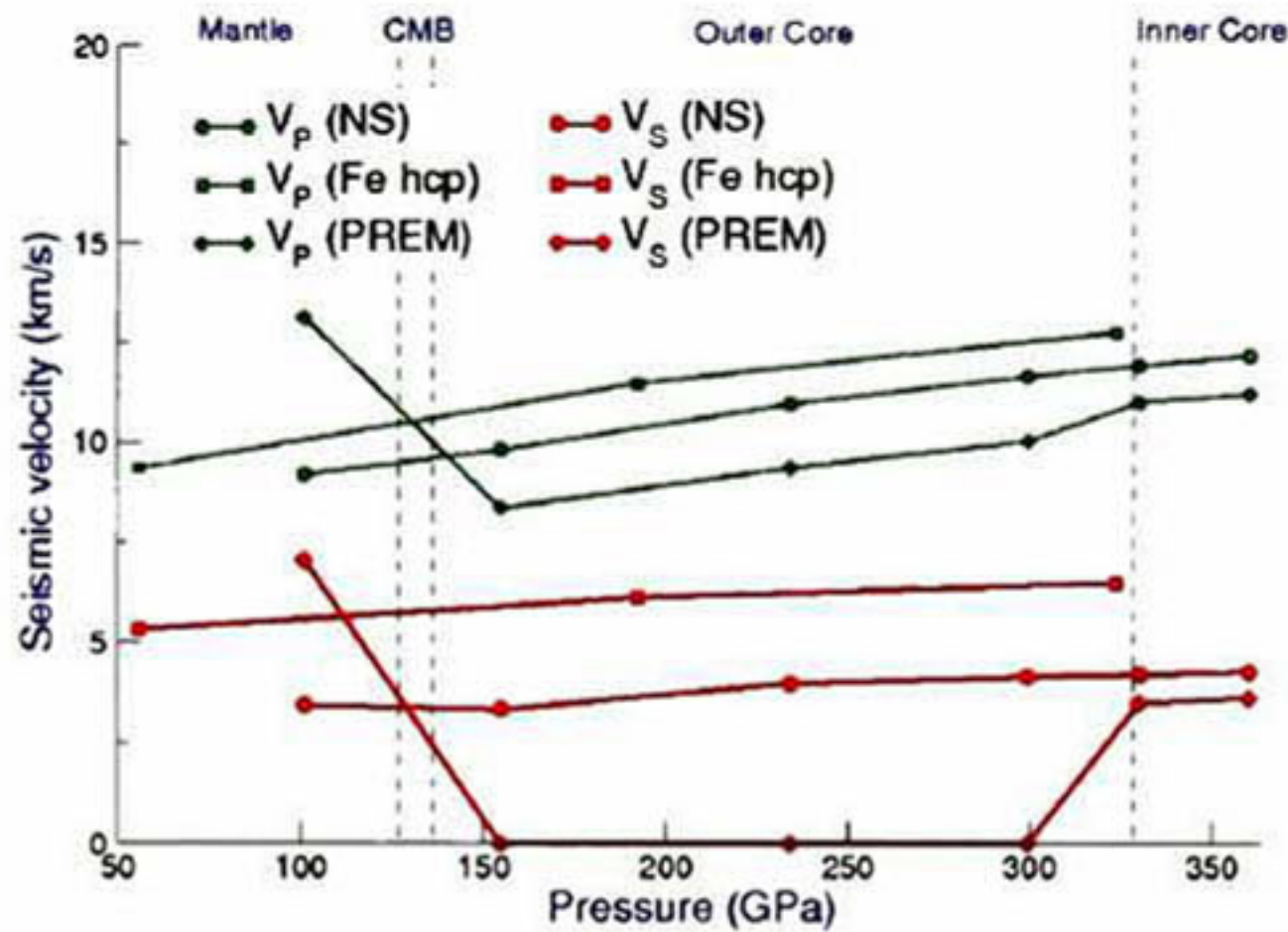


Figure 5.4: Compressional V_P and shear V_S wave velocities

ditions. Additionally, the high pressure elastic constants show as well that some degree of anisotropy persists up to core conditions. Besides, the earth's inner core is seismically anisotropic, compressional sound waves travel 3-4% faster along the spin axis than in the equatorial plane. Therefore the anisotropy of Fe_3C is consistent with similar observations for the inner core.

Density

The computed density as a function of pressure is showed in figure 5.5. These results indicated that in comparison to *hcp* iron, Fe_3C is considerably lighter at high pressures. Therefore Fe_3C provides a better match of the density to the seismically observed values of the earth's core. For instance Fe_3C density is about 9% lighter than *hcp* iron at 150 GPa, and by extrapolating *Steinle – Neumann* [66] results up to 364 GPa one can see that the difference reaches 10%.

A similar analysis can be done to compare these results with *PREM* values. According to [66] at 150 GPa *PREM's* density is about 15% lighter than *hcp* iron and the difference decreases to around 8.5% at the outer-inner core boundary. This discrepancy is larger than the reported difference in the literature for the outer core. At the moment it is believed that the outer core is about 6-10% less dense than pure liquid *Fe*, while the solid inner-core is a few percent less dense than crystalline *Fe* [2]. As mentioned before, *Steinle – Neumann* calculations correspond to a crystalline solid while the outer core is in liquid state and it must present lower density. The same applies for Fe_3C , but the agreement is substantially better. In the outer core pressure domain *PREM's* density are about 6.5% lighter than Fe_3C and becomes about 1% heavier in the inner core region.

Using the *EOS* parameters of table 4.4, *Wood* derived the density of Fe_3C

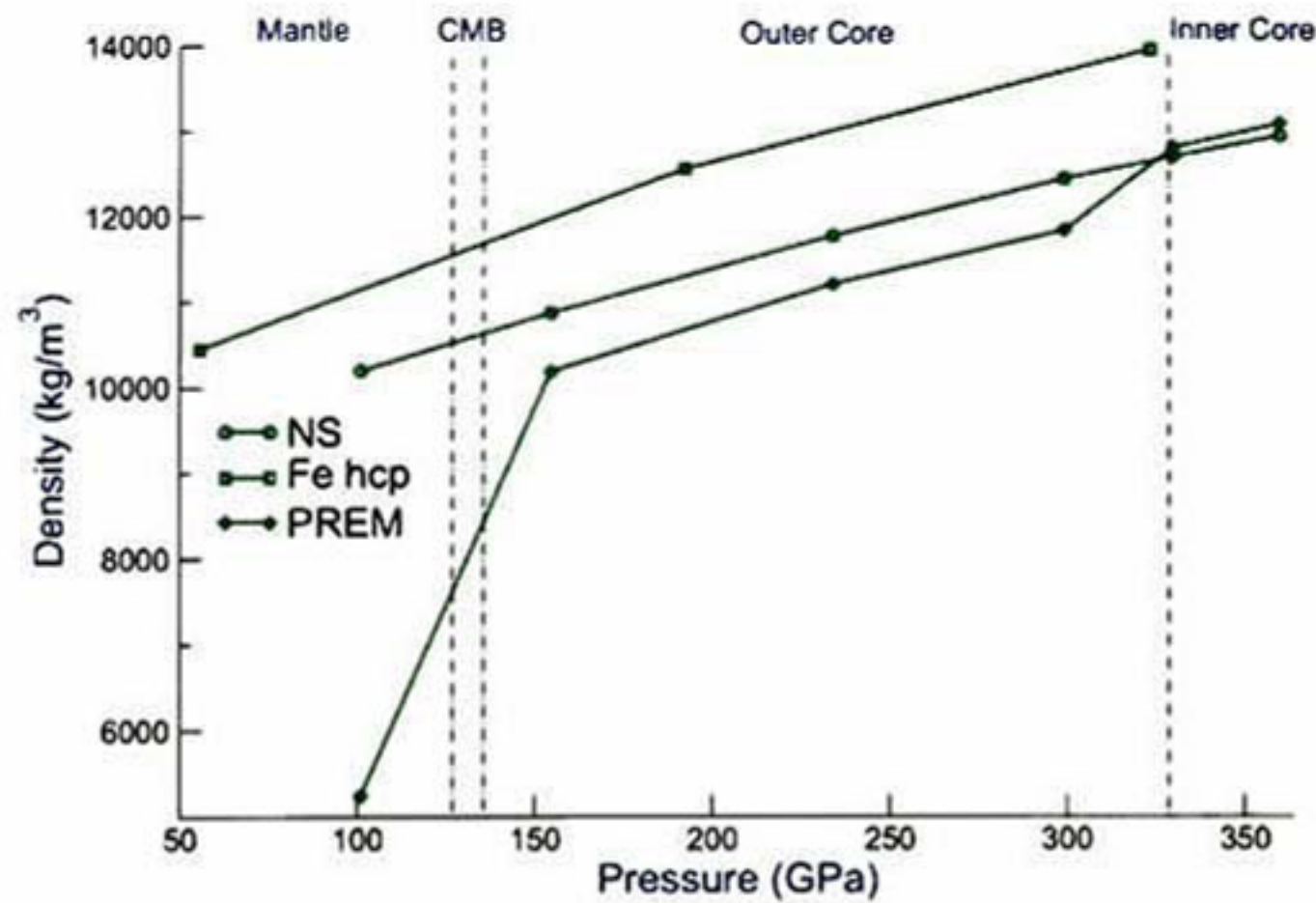


Figure 5.5: Density for NS calculation and comparison with *hcp* iron and *PREM*.

considering an average inner core pressure of 338 GPa, and obtained 12.94 Mg/m^3 . Then he applied a thermal expansion correction to an average inner core temperature of 5300 K and calculated a final density of 12.74 Mg/m^3 in excellent agreement with *PREM's* inner core data [3]. *Vocadlo et al.* did the same and obtained 12.71 Mg/m^3 and 12.35 Mg/m^3 ones they considered temperature effects. These values are well below the *PREM* range for inner core density ($12.76 - 13.09 \text{ Mg/m}^3$).

The computed density of Fe_3C at the inner core region, takes values going from 12.66 Mg/m^3 at 330 GPa (outer-inner core boundary), to 12.91 Mg/m^3 at 364 GPa. Nevertheless thermal expansion can further reduce the density. With the calculations performed in this study there is no way to estimate directly temperature effects. On the other hand, in *Wood's* and *Vocadlo's et al.* studies density decreased about 1.5% and 3% from their initial values once thermal correction was applied.

According to our zero temperature results, the density at an average inner core pressure of 338 GPa for Fe_3C , is about 12.73 Mg/m^3 and 12.91 Mg/m^3 at 364 GPa which is inside *PREM's* inner core density range ($12.76 - 13.09 \text{ Mg/m}^3$). However, if we consider that the density decreases in the same amount as *Wood* did, one comes out with no so favorable results, being 12.53 Mg/m^3 at 338 GPa and 12.72 Mg/m^3 at 364 GPa. These values are too low and were obtained considering the minimal thermal expansion effect reported in both studies. This procedure gives some idea about the temperature dependence of Fe_3C density, but definitely a more rigorous study is needed in order to exclude completely the presence of Fe_3C in the earth's core.

Here can only be stated that in comparison to *hcp* iron, Fe_3C provides a better match of density, compressional and shear wave velocities to the seismic-

cally observed values, supporting carbon as a light iron alloying element in the earth's core. In order to constrain further the possibility of Fe_3C as a major forming phase, some extra considerations has to be taken into account. For instance, is important to revisited the exact nature of the anisotropy in Fe_3C in relation with seismic observations for the inner core. On the other hand, recent studies shown that high temperature conditions greatly affects the sound velocities of *hcp* iron. The V_P and V_S of *hcp* iron decrease significantly with increasing temperature under high pressures [68]. Therefore, the temperature dependence on the V_P and V_S must be further investigated for Fe_3C as well. And finally, is extremely important to study the presence of other light alloying elements in the earth's core.

Conclusions

In this work a first principle study of iron carbide Fe_3C under pressure was performed. The main goal is to get a deeper understanding of the pressure induced magnetic transition from a low-pressure magnetically ordered state to a high-pressure magnetically disordered state observed for this compound. Consequently, structural and electronic properties for different spin configurations and residual values were computed over a large pressure range. Then the enthalpy was employed as the parameter that determines the stability of each configuration. Additionally, this alloy has been considered as a strong candidate to be a major forming constituent phase of the Earth's inner core. Therefore, elastic properties for the high-pressure non-magnetized phase were computed as well. The following conclusions were obtained.

- At the ground state the most stable phases correspond to FMM calculations with $\mu_0 = 16\mu_B$ and $\mu_0 = 20\mu_B$ per unit cell. These two phases are degenerate in enthalpy and exhibit the lattice parameters and unit cell volume closer to the experimental value.
- A transition occurs at 30 GPa, between a high moment ferromagnetic state and a non-magnetic state without stabilization of any intermediate antiferromagnetic-like state" in agreement with previous experimental results. However, there are a large number of ways in which antiferromagnetic configurations (of the type of the AFM-S) can be arranged for the crystal structure of cementite. Therefore, the antiferromagnetic configurations presented in this work, can serve only to exclude them to be stable phases across the transition in Fe_3C .
- For the AFM-S configuration around 20 GPa, a transition from high spin state to a low spin state in the local magnetic moment of iron atoms was observed as well. In comparison to the transition observed for FM and FMM configurations, the drop of the local magnetic moment of iron atoms is larger and takes place in a smaller interval of pressures.
- During the compression the unit cell deforms in a continuous way and the material retains its orthorhombic symmetry. The compression data clearly showed a discontinuity at 30 GPa in the axial ratios (c/a and b/a). Indicating that the a axis is more compressible relative to c and b in the low pressure regime, following the relative compression trend $a < c < b$.

From this point the compression mechanism is inverted ($a > c > b$), and turns out to be quite isotropic at high pressures.

- The discontinuity in the relative axial compressibility is reflected in the angle compressibility as well. Around 30 GPa an abrupt change in the slope of the compressibility of angles between Fe and C atoms ($C_2 - Fe_{g2} - Fe_{g6}$ and $Fe_{g1} - C_2 - Fe_{g2}$) was detected at low pressures. Accordingly, at the ground state the existence of a $p - d$ hybrid band formed by the transferred $2p$ electrons of carbon atoms to the d electrons of iron atoms reflected on its density of states, it has been suggested as the main reason for the relative weakening of the Fe moment in cementite as compared to pure $bcc Fe$ [50]. Therefore the loss of magnetization induced by pressure, is related as well to the bonding interactions between Fe and C atoms.
- Supporting the aforementioned idea, it has been found that the same characteristics responsible for the difference in the magnetic moment of iron atoms at different sites (at the ground state), still holds at large pressures. That is to say, stronger interactions between Fe_g atoms and its iron environment due to shorter $Fe_g - Fe$ distances and the bonding interactions between Fe and C atoms ($d(Fe_g - C) > d(Fe_s - C)$). Therefore, is possible that one of the ingredients for the loss of magnetization, is the reduction of local magnetic moment of Fe_g atoms enhanced by pressure.
- Due to the observed magnetic phase transition in Fe_3C the $P - V$ data has to different trends before and after the transition. As a result the EOS parameters depend notably on the state of magnetization and the pressure (or volume) range over which the fit is performed. Therefore, one has to be careful, when making predictions about the physical properties of Fe_3C under high pressure conditions. The only way to overcome this difficulty, it would be to fit the data to an EOS that consider analytically the effect of the magnetization. At the moment, there is no such EOS and deeper research is desirable in this field.
- The elastic constant tensor at the ground state was determined for the FM calculation and FMM with $\mu_0 = 16$ and $\mu_0 = 20$ Bohr's magneton since these are the calculations that resemble better the magnetic state of cementite at the ground state.
In general for C_{11} , C_{22} , C_{12} , C_{23} , C_{55} and C_{66} elastic constants the agreement between the obtained results and references [13], [61] is at the most 15%. But can be bigger for the rest of the elastic constants. In particular for the FM calculation, C_{44} is negative, which violates the elastic stability conditions for the orthorhombic symmetry. The obtained ground state magnetic moment is 17 Bohr's magneton per unit cell, nevertheless FMM with $\mu_0 = 16$ and $\mu_0 = 20$ are elastically stable, this indicates that elastic stabilization can be induced by a small change of the magnetic state.
- For FMM with $\mu_0 = 16$ and $\mu_0 = 20$ the results show that C_{44} amounts about 1/15 of C_{55} , C_{66} which means that at the ground state cementite presents some degree of elastic anisotropy.
- The elastic constants tensor was determined for the high-pressure non-magnetized phase of Fe_3C (NS calculation), for pressure values in the

range 100GPa to 364GPa. The full set of single-crystal elastic constants has not been reported experimentally (not even at the ground state). These calculations allow for the first time the comparison of the high-pressure elastic properties of Fe_3C with iron and PREM values.

- According to the obtained results, under compression Fe_3C is an elastically stable structure at high pressures. Fe_3C possesses some elastic anisotropy at high pressures. For instance C_{22} presents the highest value, followed by C_{33} and C_{11} . This indicates that the crystal is less compressible in the b axis followed by the c and a axis. Corroborating the compression mechanism deduced by computing the axial compressibility for FM and FMM calculations above 30 GPa.
- At high pressures hcp iron is more anisotropic, but the degree of anisotropy increases more as a function of pressure for Fe_3C .
- Interestingly, despite the difference in the predicted single crystal elastic constants, different crystal structure, mass density and composition, the predicted evolution of Fe_3C bulk modulus differ little from that of hcp iron. By the contrary the shear modulus of Fe_3C is quite lower. By adding carbon, density decreases and one expects a decrease of the bulk modulus that would equal better PREM values. However in the form of Fe_3C , adding carbon does not have a considerable effect on the bulk modulus over that of iron hcp. But it does help to match better the shear modulus with PREM. For instance at the outer-inner core boundary the difference with respect to PREM shear modulus is 49% and 280% for Fe_3C and hcp iron respectively and 36.8% and 263% at the earth's center.
- Carbon would considerably reduce the seismic wave velocities and density of the iron-based alloys of the Earth's core in comparison to Fe alone. However we have calculated density values going from 12.66 Mg/m^3 at 329GPa, to 12.947 Mg/m^3 at 364GPa which are inside PREM's density range for the inner core, but probably too low if the presence of other light alloying elements has to be considered.

Bibliography

- [1] Javier Antonio Montoya Martinez. *Ab initio study on synthesis of new materials at high pressure*. PhD thesis, International school for advanced studies ISAS, 2007.
- [2] Jean-Paul Poirier. Light elements in the earth's outer core: a critical review. *Phys. Earth Planet. Inter.*, 85:319–337, 1994a.
- [3] Bernard J. Wood. Carbon in the core. *Earth and Planetary Science Letters*, 117:593–607, 1993.
- [4] H. K. Mao Y. Fei E. Gregoryanz M. Eremets c. S. Zha J. Li. Compression of Fe_3C to 30 gpa at room temperature. *Phys. Chem. Min.*, 29:166–169, 2002.
- [5] Q. Williams E. Knittle H. P. Scott. Stability and equation of state of Fe_3C to 73 gpa; implications for carbon in the earth's core. *Geophys. Res. Lett.*, 28:1875–1878, 2001.
- [6] Lidunka Vocadlo K. S. Knight David P. Dobson W. G. Marshall G. David Price I. G. Wood and Jhon Brodholt. J. Thermal expansion and crystal structure of cementite, Fe_3C , between 4 and 600 k determined by time-of-flight neutron powder diffraction. *Appl. Crystallog.*, 87:32, 2004.
- [7] Vocadlo L., Brodholt J., Dobson D. P., Knight K. S., Marshall W. G., Price G. D., and Wood I. G. The effect of ferromagnetism on the equation of state of Fe_3C studied by first principles calculations. *Earth and Planetary Science Letters*, 203:567–575, 2002.
- [8] Dr. Ken Rubin. http://www.soest.hawaii.edu/GG/ASK/earths_core.html. Assistant Professor Department of Geology and Geophysics University of Hawaii, Honolulu, HI 96822.
- [9] Jean-Paul Poirier. *Introduction to the physics of the earth's interior*, chapter 4. Cambridge University Press, 2000.
- [10] D. Alfé J. Brodholt L. Vocadlo and G. D. Price M. J. Gillan. First-principles modelling of earth and planetary materials at high pressures and temperatures. *Rep. Prog. Phys.*, 69:2365–2441, 2006.
- [11] Kei Hirose Katsuyuki Kawamura Nagayoshi Sata Yasuo Ohishi Motohiko Murakami. Post-perovskite phase transition in $mgsio_3$. *Science*, 304(5672):855–858, 2004.

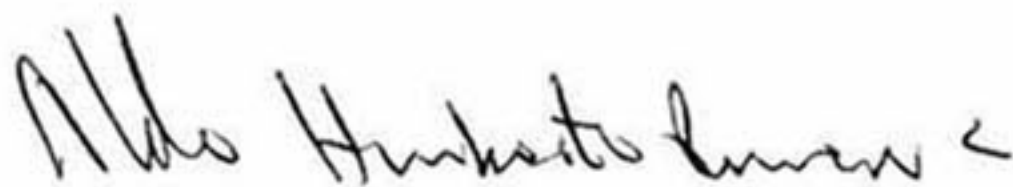
- [12] D. Dolejs I. Yu. Kantor C. A. McCammon D. J. Frost V.B. Prakapenka J. Rouquette and L. S. Dubrovinsky. Iron-carbon interactions at high temperatures and pressures. *Applied Physics Letters*, 92:121912, 2008.
- [13] C.; Srinivasan S. G.; Caro A.; Maloy S. A. Jiang. Structural, elastic and electronic properties of Fe₃C from first principles. *Journal of Applied Physics*, 103(4), 2008.
- [14] Anthony J. Falzone and Frank D. Stacey. Second order elasticity theory: An improved formulation of the Grüneisen parameter at high pressure. *Physics of The Earth and Planetary Interiors*, 4(4):284–290, 1981.
- [15] J.-M. Beuken R. Caracas F. Detraux M. Fuchs G.-M. Rignanese L. Sindic M. Verstraete G. Zerah F. Jollet M. Torrent A. Roy M. Mikami Ph. Ghosez J.-Y. Raty D.C. Allan. X. Gonze. First-principles computation of material properties : the abinit software project. *Computational Materials Science*, 25:478–492, 2002.
- [16] M. P. Teter D. C. Allan T. A. Arias J. D. Joannopoulos M. C. Payne. Iterative minimization techniques for *ab initio* total-energy calculations: molecular dynamics and conjugate gradients. *Reviews of Modern Physics*, 64(4), 1992.
- [17] P. Hohenberg and W. Kohn. Inhomogeneous electron gas. *Phys. Rev. Lett.*, 136(3B):864–871, 1964.
- [18] Capelle K. A bird's-eye view of density-functional theory. *Brazilian Journal of Physics*, 36(4A):1318–1343, 2006.
- [19] W. Kohn and L. J. Sham. Self-consistent equations including exchange and correlation effects. *Phys. Rev. Lett.*, 140(4A):1133–1138, 1965.
- [20] Martin R. M. Density functional theory for electrons in materials. Summer School on Computational Material Science, University of Illinois at Urbana-Champaign, 2001.
- [21] Efthimios Kaxiras. *Atomic and Electronic Structure of Solids*. Cambridge University Press, The Edinburgh Building, Cambridge CB2 2RU, United Kingdom, first edition edition, 2003.
- [22] Wolverton C. Ceder G. Hafner J. Toward computational materials design: The impact of density functional theory on materials research. *MRS Bulletin* 31, 31:669–668, 2006.
- [23] C. Kittel. *Introduction to Solid State Physics*. Wiley, New York, 7th ed. edition, 1996.
- [24] H. J. Monkhorst and J. D. Pack. Special points for Brillouin-zone integration. *Physical Review B*, 13:5188–5192, 1976.
- [25] P. E. Bloch. Projector augmented-wave method. *Phys. Rev. B*, 50:17953–17979, 1994.

- [26] C. J. Först and J. Schimpl P. E. Blochl. Projector augmented wave method: ab initio molecular dynamics with full wave functions. *Bull. Mater. Sci.*, 26(1):33–41, January 2003.
- [27] M. Schlüter and C. Chiang D. R. Haman. *Phys. Rev. Lett.*, 43:1494, 1979.
- [28] J. C. Slater. *Phys. Rev. B*, 51:846, 1937.
- [29] P. M. Marcus. *Int. J. Quantum. Chem.*, 1S:567, 1967.
- [30] Carsten Rostgaard. The projector augmented-wave method. arXiv:0910.1921, October 2009.
- [31] G.-M. Rignanese M. Verstraete J.-M. Beuken Y. Pouillon R. Caracas F. Jollet M. Torrent G. Zerah M. Mikami Ph. Ghosez M. Veithen J.-Y. Raty V. Olevano F. Bruneval L. Reining R. Godby G. Onida D.R. Hamann X. Gonze and D.C. Allan. Zeit. A brief introduction to the abinit software package. *Kristallogr.*, 220:558–562, 2005.
- [32] F. Jollet F. Bottin G. Zerah M. Torrent and X. Gonze. Implementation of the projector augmented-wave method in the abinit code. application to the study of iron under pressure. *Computational Materials Science*, 42:337, 2008.
- [33] A.R. Tackett G.E. Matthews N.A.W. Holzwarth. A projector augmented wave (paw) code for electronic structure calculations, part i: atompaw for generating atom-centered functions.
- [34] N.A.W. Holzwarth G.E. Matthews A.R. Tackett. A projector augmented wave (paw) code for electronic structure calculations, part ii: pwpaw for periodic solids in a plane wave basis. *Computer Physics Communications*, 135:348–376, 2001.
- [35] R. Resta A. D. Corso. Density-functional theory of macroscopic stress: Gradient-corrected calculations for crystalline se. *Phys. Rev. B*, 50(7):4327–4331, August 1994.
- [36] M. C. Payne G. P. Francis. Finite basis set corrections to total energy pseudopotential calculations. *J. Phys.: Condens. Matter*, 2:4395, 1990.
- [37] Martin Fuchs. Comparison of exchange-correlation functionals: from lda to gga and beyond. *Density-Functional Theory Calculations for Modeling Materials and Bio-Molecular Properties and Functions - A Hands-On Computer Course*, IPAM, UCLA, Los Angeles, USA, 2005.
- [38] Scuseria Perdew Staroverov. Comparison of *lda*, *gga*, and *meta - gga*. *Phys. Rev. B*, 69(075102), 2004.
- [39] Martin R. M. *Electronic Structure, Basic Theory and Practical Methods*. Cambridge University Press, 2004.
- [40] G. E. Matthews R. B. Dunning A. R. Tackett N. A. W. Holzwarth and Y. Zeng. Comparison of the projector augmented-wave, pseudopotential, and linearized augmented-plane-wave formalisms for density-functional calculations of solids. *Phys. Rev. B*, 55:2005–2017, 1997.

- [41] D. Joubert G. Kresse. From ultrasoft pseudopotentials to the projected augmented-wave method. *Phys. Rev. B*, 59:1758–1775, 1999.
- [42] J. Cho and M. Scheffler. *Ab initio* pseudopotentials study of fe, co and ni employing the spin-polarized lapw approach. *Phys. Rev. B*, 53:10685–10689, 1996.
- [43] R. E. Cohen and D. J. Singh L. Stixrude. Iron at high pressure: Linearized-augmented-plane-wave computations in the generalized-gradient approximation. *Phys. Rev. B*, 50:6442–6445, 1994.
- [44] G.A. Jeffrey E.J Fasiska. On the cementite structure. *Acta Crystallographica*, 19:463,461, 1965.
- [45] D. E. Jiang and Emily A. Carter. Carbon dissolution and diffusion in ferrite and austenite from rst principles. *Physical Review B*, 67:214103, 2003.
- [46] Hassel Ledbetter. Polycrystalline elastic constants of in situ cementite (Fe_3C). *Materials Science and Engineering A*, 527:2657–2661.
- [47] N.I. Medvedeva A.L. Ivanovskii I.R. Shein. Electronic and structural properties of cementite-type M_3X ($M = Fe, Co, Ni$; $X = C$ or B) by first principles calculations. *Physica B*, 371:126–132, 2006.
- [48] Trapeznikov V.A. Shabanova I.N. Temperature dependence of the intensity of the characteristic energy losses of $2p$ electrons of iron in cementite. *JETP Letters*, 18:576, 1973.
- [49] E.M. Cohn L.J.E. Hofer. Saturation magnetizations of iron carbides. *J. Am. Chem. Soc.*, 81:1576–1582, 1959.
- [50] Andrei V. Ruban Peter Mohn Sergii Khmelevskiy. Electronic structure analysis of the pressure induced metamagnetic transition and magnetovolume anomaly in Fe_3C -cementite. *J. Phys.: Condens. Matter*, 17:7345–7352, 2005.
- [51] S. L. Randzio. Transitiometric analysis of pressure effects on various phase transitions. *Journal of Thermal Analysis and Calorimetry*, 57:165–170, 1999.
- [52] M. Acet T. Hülser E. F. Wassermann B. Rellinghaus J. P. Itié and P. Munsch E. Duman. Large spontaneous magnetostrictive softening below the curie temperature of Fe_3C invar particles. *Journal of Applied Physics*, 96(10):5668–5672, nov 2004.
- [53] A. Tröster J. Koppensteinerl W. Schranz and R. Miletich. Finite strain landau theory of high pressure phase transformations. *J. Phys.: Condens. Matter*, 19, 2007.
- [54] Yingwei Fei Wolfgang Sturhahn Jiyong Zhao Ho kwang Mao Russell J. Hemley Jung-Fu Lin. Magnetic transition and sound velocities of Fe_3C at high pressure: implications for earth and planetary cores. *Earht and Planetary Science Letters*, 226:33–40, 2004.

- [55] S. Endo K. Miura F. Ono M. Matsushita. Evidence of new high-pressure magnetic phases in fe-pt invar alloy. *Journal of Magnetism and Magnetic Materials*, 260:371–374, 2003.
- [56] F. Baudelet J. P. itié A. Polian S. Pizzini A. Fontaine Ch. Giorgetti E. Dartyge J. P. Kappler S. Odin. Experimental evidence of pressure-induced magnetic phase transition in $Fe_{72}Pt_{28}$ invar alloy. *Journal of Applied Physics*, 83(11):7291–7293, 1998.
- [57] Jung-Fu Lin, V. V. Struzhkin, Ho kwang Mao, R. J. Hemley, P. Chow, and M. Y. Hu. Magnetic transition in compressed Fe_3C from x-ray emission spectroscopy up to 45gpa. *Phys. Rev. B*, 70:212405, 2004.
- [58] M. Acet E. F. Wassermann J. P. Itié F. Baudelet O. Mathon S. Pascarelli E. Duman. Magnetic instabilities in Fe_3C cementite particles observed with *fe k - edge x - ray* circular dichroism under pressure. *Physical Review Letters*, 94:075502, 2005.
- [59] Bin Chen Jingyun Wang Esen E. Alp Jiyong Zhao Michael Lerche Wolfgang Sturhahn Henry P. Scott Fang Huang Yang Ding Stanislav V. Si Sinogeikin Craig C. Lundstrom Jay D. Bass and Jie Li Lili Gao. Pressure induced magnetic transition and sound velocities of Fe_3C : Implications for carbon in the earth's inner core. *Geophys. Res. Lett*, 35(2008):L17306.
- [60] Eleda M. Johnson. The elastic behavior of plagioclase feldspar at high pressure. Master's thesis, Virginia Polytechnic Institute and State University, December 2007.
- [61] S. L. Jhang T. Gressmann A. Leineweber E. J. Mittemeiger Y. Wang and Z. -K. Liu M. Nikolossi. Extreme elastic anysotropy of cementite fe_3c : first principles calculations and experimental evidence. *Scripta Materialia*, 59:814–817, 2008.
- [62] M.M. Fejer B.A. Auld P. Toledano. *Phys. Rev. B*, 27(5717), 1983.
- [63] R.W. Cahn. *Nature*, 413:582, 2001.
- [64] A. K. M. A. Islam and F. N. Islam A. Hossain. Elastic properties of - and -phases of li_3n . *J. Sci. Res.*, 1(2):182–191, 2009.
- [65] H. Nolle J. F. Laszlo. *Mech. Phys. Solids*, 7:193, 1959.
- [66] Lars Stixrude and Ronald E. Cohen Gerd Steinle-Neumann. First-principles elastic constants for the hcp transition metals fe, co, and re at high pressure. *Phys. Rev. B*, 60(2):791–799, 1999.
- [67] H. J. Xiang Jinlong Yang J. G. Hou and Qingshi Zhu Z. Y. Chen. A hard metallic material: Osmium diboride. *Phys. Rev. B*, 74:012102, 2006.
- [68] W. Sturhahn J. Zhao G. Shen H.K. Mao R.J. Hemley J.F. Lin. Absolute temperature measurement in a laser-heated diamond anvil cell. *Geophys. Res. Lett*, 226:33–40, 2004.


EL JURADO DESIGNADO POR LA UNIDAD QUERÉTARO DEL CENTRO DE INVESTIGACIÓN Y DE ESTUDIOS AVANZADOS DEL INSTITUTO POLITÉCNICO NACIONAL, APROBÓ LA TESIS DE MAESTRÍA DEL LA C. ALEJANDRA VARGAS CALDERÓN TITULADA: "STRUCTURAL AND ELECTRONIC CHARACTERIZATION OF Fe_3C UNDER PRESSURE. AN AB INITIO STUDY", FIRMAN AL CALCE DE COMÚN ACUERDO LOS INTEGRANTES DE DICHO JURADO, EN LA CIUDAD DE QUERÉTARO, QRO., A LOS SIETE DIAS DEL MES DE JUNIO DE DOS MIL DIEZ



DR. ALDO HUMBERTO ROMERO CASTRO



DRA. REBECA CASTANEDO PÉREZ



DR. FRANCISCO JAVIER ESPINOZA BELTRÁN

